Chemistry, Dynamics, and Radiation of Ozone Loss: Airborne Measurements of OH, HO_2, NO_2, ClO, BrO, IO, $ClONO_2$, $BrONO_2$, ClOOCl, and H_2O

Final Summary of Research
NASA Langley Grant NNL04AA14G
January 1, 2004–December 31, 2004

Submitted to
National Aeronautics and Space Administration
from
President and Fellows of Harvard College
c/o Office for Sponsored Programs
Holyoke Center, Suite 600
1350 Massachusetts Avenue
Cambridge, Massachusetts 02138

James G. Anderson, Principal Investigator
Division of Engineering and Applied Sciences and
Department of Chemistry and Chemical Biology
Harvard University
12 Oxford Street
Cambridge, MA 02138

May 20, 2005

A. Chemistry, Dynamics, and Radiation of Ozone Loss: Airborne Measurements of OH, HO_2, NO_2, ClO, BrO, IO, $ClONO_2$, $BrONO_2$, ClOOCl, and H_2O

B. Prof. James G. Anderson, Harvard University, 12 Oxford Street, Cambridge, MA 02138. Phone: 617-495-5922; Fax: 617-495-4902; E-mail: anderson@huarp.harvard.edu; http://www.arp.harvard.edu/

C. Abstract of Research Objectives:

This grant continued the research initially funded under NAG1-01095. This research addresses, through a combination of *in situ* and remote aircraft-borne instruments, the following scientific questions:

- Which mechanisms are responsible for the continuing erosion of ozone over midlatitudes of the Northern Hemisphere?
- Will the rapid loss of ozone over the Arctic in late winter continue to worsen over the next two decades? Are these large losses dynamically coupled to midlatitudes?
- Which mechanisms dictate the rate of exchange of material between the troposphere and stratosphere? How will these processes change in response to changes in climate?
- Will regional scale pollution episodes, that are emerging as predictable seasonal events, significantly affect the middle-to-upper troposphere chemical composition. If so, how will these changes alter the chemical composition of the middle world? What changes are predicted for the overworld?
- Why has the arctic stratosphere become colder in the late winter phase in recent years? Have increases in tropical upper troposphere temperatures increased the temperature gradient such as to change the trajectories of vertically propagating waves, thus reducing the effectiveness of the meridional circulation for transport of heat, momentum and ozone from the tropics to high latitudes?

D. Summary of Research:

Results for the period 1 January 2004 to 31 December 2004 are summarized in the following six sections:

The text of this progress report consists of the detailed description of those developments.

Section 1: Resonance fluorescence instrument for the *in situ* detection of BrO in the atmosphere

It is well established that bromine compounds, which enter the atmosphere from a variety of natural and anthropogenic sources, cause stratospheric and tropospheric ozone depletion [Wofsy *et al.*, 1975; McElroy *et al.*, 1986; Anderson *et al.*, 1989; Garcia and Solomon, 1994; Wennberg *et al.*, 1994; Hausmann and Platt, 1994; Lary, *1996*; Wamsley *et al.*, 1998; World Meteorological Organization, 1995]. Despite being present at much lower atmospheric concentrations than chlorine compounds, bromine compounds are much more efficient at ozone destruction on a per atom basis. This is because a large fraction of inorganic bromine is present in chemically active forms, while most inorganic chlorine is sequestered in the relatively long-lived reservoirs, HCl and $ClONO_2$. Only a few percent of the total inorganic chlorine in the stratosphere is in the reactive form ClO, while more than half of the inorganic bromine is present as reactive BrO during daylight. At altitudes below 25 km the BrO/ClO and BrO/HO_2 cycles are among the most important ozone destruction cycles [Wennberg *et al.*, 1994; *Lary*, 1996].

The extent to which bromine and the other halogen species are responsible for the observed losses of ozone over midlatitudes of the northern hemisphere is an area of continued uncertainty. The latest WMO report, *Scientific Assessment of Ozone Depletion: 2002*, states: "The vertical, latitudinal, and seasonal characteristics of changes in midlatitude ozone are broadly consistent with the understanding that halogens are the primary cause of these changes, in line with similar conclusions from the 1998 Assessment." Other studies, however, have indicated alternative explanations to midlatitude ozone loss. Given the continued uncertainty, it is essential to examine the full complement of halogen radical families in the lower stratosphere from the tropics to midlatitudes. Accurate BrO measurements, in particular, are critical due to the high efficiency of bromine compounds at ozone destruction. Historically, most of the atmospheric field measurements have focused on chlorine compounds, but bromine is potentially more important, and it is certainly less well understood.

Efforts to test the abundance and speciation of bromine in the stratosphere have been particularly hampered by low atmospheric concentrations. Of the relatively few *in situ* measurements of BrO in the stratosphere [Brune and Anderson, 1986; Brune *et al.*, 1988; Brune *et al.*, 1989; Toohey *et al.*, 1990; Avallone *et al.*, 1995], the majority were made onboard the NASA ER-2 aircraft with the Harvard ClO/BrO instrument, a predecessor to the current Harvard Halogen instrument. The basic mode of operation was resonance fluorescence detection of Br atoms generated from chemical titration of BrO with NO. This is the analogous technique to that for ClO. Because the BrO concentrations were low, the Br fluorescence signal was weak relative to the background signal, and long averaging times were required. Typically, less than ten BrO measurements were produced for an eight-hour ER-2 flight.

This work describes an experimental effort to design and produce an instrument capable of measuring BrO *in situ* in the stratosphere with a higher signal-to-noise ratio than ever previously attained. Bromine data successfully acquired with this new instrument on the SOLVE mission to Kiruna, Sweden, are presented and discussed.

Harvard Halogen Instrument for Bromine Detection

The technique for ambient BrO detection involves chemical conversion via a rapid bimolecular reaction with NO followed by ultraviolet resonance fluorescence detection of Br atoms.

$$BrO + NO \rightarrow Br + NO_2$$
$$Br + h\nu(\text{RF lamp}) \rightarrow Br^*$$

$$Br^* \rightarrow Br + h\nu(\text{signal})$$

A schematic diagram of the Harvard Halogen flight instrument, as mounted in the super pod of the NASA aircraft, is pictured in Figure 1-1. The instrument measures BrO, ClO, ClOOCl, $ClONO_2$, and is being modified to add IO detection capability. The instrument has recently been described in detail [Wilmouth, 2002; Stimpfle *et al.*, 2004]. Only the components relative to BrO detection will be discussed here.

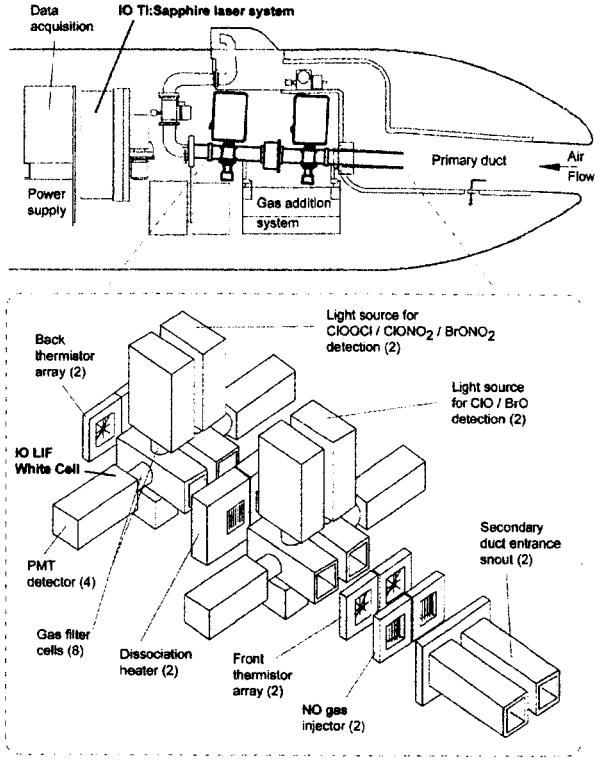

Figure 1-1. Harvard Halogen flight instrument (top left). A cross-section of the instrument in the aircraft wing pod with a perspective view of the critical elements of the detection scheme (bottom left). Photo of the instrument.

Ambient air enters the 20 cm diameter primary duct at a velocity of ~60 m/s, approximately one third that of the aircraft. A throttle valve, located at the top of the pod where the bulk of the flow exits, is used to regulate the velocity in the primary duct. The laminar core of the primary flow is extracted and decelerated to ~10–15 m/s into two 5 cm square, mirror-image, secondary ducts, where the halogen measurements are made. This nested-duct design not only aids in slowing the sample air but also in maintaining laminar flow and minimizing wall contact.

The entrance to each secondary duct is a 26 cm long fairing followed by a gate valve, which is always open during flight but typically closed during takeoff and landing. A nitric oxide injector, consisting of nine perforated teflon tubes, mixes dilute NO (1:5 NO in N_2 along with nitrogen carrier gas) uniformly into the flow. An array of seven fast-response platinum resistance thermistors mounted on wire supports monitor the ambient air temperature immediately forward of the front detection axis, where Br from the titration of BrO with NO is detected via ultraviolet resonance fluorescence. A pitot tube at the rear of the secondary duct reads ambient pressure and velocity, while a throttle valve near the secondary duct exit is used to control the flow velocity. Other relevant components of the instrument include a gas deck, where NO and air for the gas filter cell purges are housed, computer and data acquisition system, and power supplies.

The central idea for improving the bromine detection system over previous incarnations of the experiment was to decrease the overall path length from the lamp to the PMT, thereby

maximizing the flux density in a small volume. While the lamp and PMT are completely outside of the flow for chlorine measurements as well as previous bromine measurements, the improved bromine axis has the lamp and PMT penetrating the secondary duct wall in order to bring them into close proximity to one other. The UV lamp design was also changed to one that is longer with a narrower body. The new lamps have a 10 mm diameter, down from 14 mm, and have RF power coupled into the lamp in two places. The narrow body lamp tends to form a confined plasma compared to previous lamp designs.

Figure 1-2 shows a cross-section view of the RF detection axis of bromine and, for comparison, of chlorine. The lamp body and PMT extend into the flow tube for the bromine axis. Baffles and spacers are held at the end of the lamp by a retainer cap and at the end of the PMT by a rotatable hood. Preventing direct scatter between the lamp and PMT from becoming a large source of noise resulting from placing the two components close together was of particular concern. Razor blade light traps placed opposite the lamp and detector and purges of all volumes in the optical path were established in order to further optimize sensitivity.

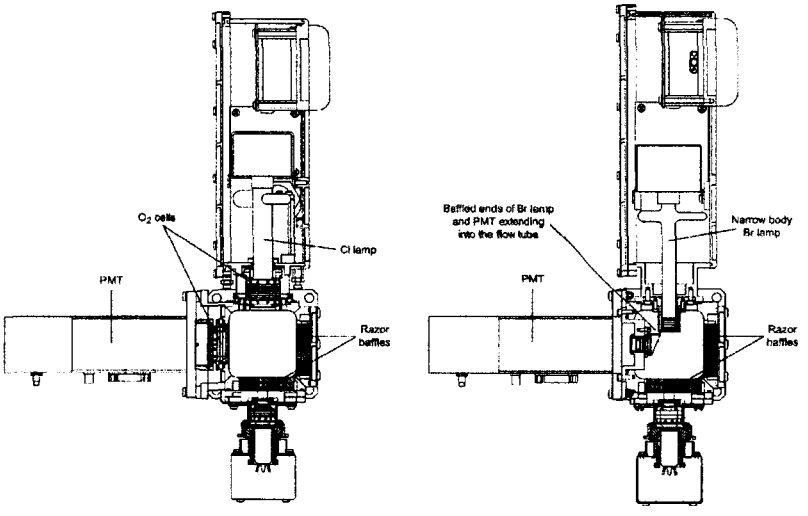

Figure 1-2. Cross-section of the complete RF detection axis of chlorine (left) and bromine (right).

Bromine Calibration

Calibration of the bromine detection system takes advantage of our well-established chlorine atom calibration. Specifically, a known, constant flow of Cl is titrated with excess Br_2 to generate a quantitative Br source.

$$Cl + Br2 \rightarrow BrCl + Br \qquad k = 1.6\times10\text{-}10 \text{ cm3 molec-1 s-1}$$

The slope of a plot of ΔBr signal versus $-\Delta Cl$ signal is a direct measure of the relative sensitivity of the Br axis to the Cl axis. The intercept of the plot is zero by definition and observation.

$$C^{Br} = \text{slope} \times C^{Cl}$$

The laboratory-determined calibration factor, C^{Br}, is the critical value necessary to relate observed bromine signal to bromine concentration.

$$SBr = CBr \times [Br]$$

Sample bromine calibration data are shown in Figure 1-3. Calibrations are run at different pressures in nitrogen and air and with different lamps, reaction distances, and flow conditions. The estimated accuracy of the BrO measurements from the Harvard Halogen flight instrument is ±20% (1σ) with a detection limit of 3 pptv in 5 minutes.

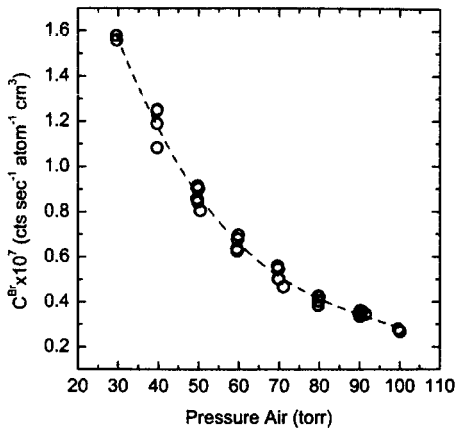

Figure 1-3. Bromine calibration data for 0226, where C^{Br} is the critical laboratory-determined calibration factor necessary to relate bromine signal to concentration: $S^{Br} = C^{Br}[Br]$.

BrO Measurements

The improvements to the bromine detection system provide the capability to detect BrO *in situ* in the atmosphere with greater sensitivity, precision, and spatial resolution than previously possible. Calibrated measurements from the SOLVE mission to Kiruna, Sweden, when BrO measurements were made during twelve ER-2 flights, are shown here.

Figure 1-4 shows halogen data from three sample flights during the SOLVE mission: 0131, 0226, and 0305. These flights occurred entirely within the Arctic vortex. In each plot, Harvard Halogen instrument measurements of ClO are shown in the upper panel and BrO in the second panel. The BrO data shown in blue are median filtered, and the red filled circles are binned averages of the raw data. Statistical data for BrO are shown for each flight in Tables 1-1 through 1-3.

Increases or decreases in the observed mixing ratios of ClO and BrO typically occur concurrently during these flights. This is particularly poignant on the 0131 flight, which involved a daytime-nighttime transition. The ER-2 took off in sunlight, traveled north within the vortex into darkness, then returned south where sunlight was again encountered. There is a clear diurnal dependence in the measurements. BrO is high in sunlit conditions and essentially zero at nighttime.

The third panel in each plot of Figure 1-4 shows calculated BrCl. Because NO_2 levels are extremely low inside the Arctic vortex, BrCl rather than $BrONO_2$ is the primary form of inorganic bromine in addition to BrO. BrCl is calculated from a steady-state expression using the ClO and BrO measurements and photolysis rate data. Steady-state values cannot be calculated at nighttime using this method, so BrCl data are necessarily absent in darkness. The lowermost panel in each plot shows mixing ratios of the inorganic bromine species and the bromine budget. Specifically, BrO is shown in blue and BrCl in black. Br_y, shown in red, is determined from the ACATS instrument, which also flew onboard the ER-2 during the SOLVE mission. The sum of BrO and BrCl is represented in green.

Of greatest interest in Figure 1-4 is that BrO + BrCl is consistently greater than total inorganic bromine, Br_y inferred from organic bromine measurements. On average, over the course of the entire SOLVE mission, the sum of the measured BrO and calculated BrCl is 3–4 ppt greater than Br_y. Any $BrONO_2$ present would increase this even further. This suggests that the historic values used for inorganic bromine in ozone trend assessments may not be valid. Specifically, including more bromine in the models would serve to increase the computed ozone depletion, a change which would bring better agreement between modeled and measured ozone loss. This result is consistent the recent work of Salawitch *et al.* [2005], which suggests that inorganic bromine at and above the tropopause is 4 to 8 ppt greater than assumed in models for past ozone trend assessment studies.

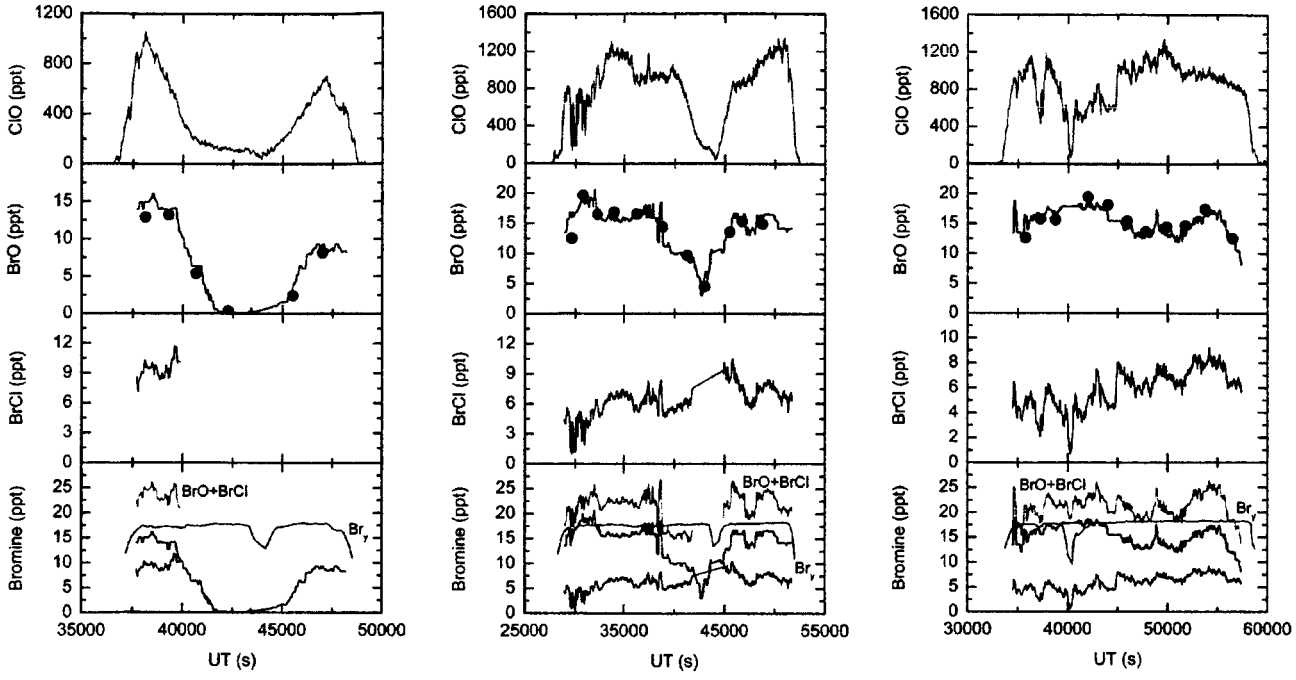

Figure 1-4. Halogen data from 3 sample flights of the ER-2 during the SOLVE mission: 0131 (left), 0226 (middle), and 0305 (right). In each plot, ClO and BrO are measured by the Harvard Halogen instrument, BrCl is calculated using the ClO and BrO measurements and photolysis rate data, and Br_y is determined from the ACATS instrument. The colors in each lowermost panel represent the same species as in the upper panels. BrO data shown in blue are median filtered and the red filled circles are binned averages of the raw data. Statistical data for BrO are shown for each flight in Tables 1-1 through1-3.

Table 1-1. BrO data from Flight 0131. Columns represent mean time of bin, mean BrO mixing ratio in bin, standard deviation of the mean, width of the bin in seconds, and number of points in each bin.

Time (s)	BrO (ppt)	σ (%)	Bin Width (s)	N
38129	12.91	15	1100	26
39284	13.2	13	1400	40
40649	5.38	35	1300	38
42259	0.34	390	1900	54
45496	2.43	69	1000	29
47001	8.16	13	2000	57

Table 1-2. BrO data from Flight 0226. Column representations same as Table 1-1.

Time (s)	BrO (ppt)	σ (%)	Bin Width (s)	N
29641	12.53	19	700	20
30743	19.71	9	1500	43
32248	16.51	9	1500	43
33998	16.95	10	2000	57
36256	16.59	9	2500	72
38758	14.43	11	2500	71
41243	9.69	15	2500	71
42993	4.50	51	1000	29
45496	13.63	18	1000	28

46738	15.40	11	1500	43
48751	15.00	9	2500	72

Table 1-3. BrO data from Flight 0305. Column representations same as Table 1-1.

Time (s)	BrO (ppt)	σ (%)	Bin Width (s)	N
35755	12.62	17	1500	43
37260	15.76	12	1500	43
38748	15.65	12	1500	42
41985	19.53	9	2000	57
43998	18.19	9	2000	58
45905	15.49	14	1800	51
47795	13.70	10	2000	57
49895	14.47	10	2200	63
51750	14.75	9	1500	43
53745	17.46	8	2500	71
56493	12.53	11	3000	86

References

Anderson, J. G., W. H. Brune, S. A. Lloyd, D. W. Toohey, S. P. Sander, W. L. Starr, M. Loewenstein, and J. R. Podolske, Kinetics of ozone destruction by chlorine oxide and bromine oxide within the Antarctic vortex: An analysis based on *in situ* ER-2 data, *J. Geophys. Res.*, 94, 11,480–520, 1989.

Avallone, L. M., D. W. Toohey, S. M. Schauffler, W. H. Pollock, L. E. Heidt, E. L. Atlas, and K. R. Chan, In *situ* measurements of BrO during AASE II, *Geophys. Res. Lett.*, 22, 831–4, 1995.

Brune, W. H. and J. G. Anderson, In *situ* observations of midlatitude stratospheric ClO and BrO, *Geophys. Res. Lett.*, 13, 1391–4, 1986.

Brune, W.H., D.W. Toohey, J.G. Anderson, W.L. Starr, J.F. Vedder, and E.F. Danielson, In *situ* northern mid-latitude observations of ClO, O_3, and BrO in the wintertime lower stratosphere, *Science*, 242, 558–62, 1988.

Brune, W.H., J.G. Anderson, and K.R. Chan, In *situ* observations of BrO over Antarctica: ER-2 aircraft results from 54°S to 72°S latitude, *J. Geophys. Res.*, 94, 16,639–47, 1989.

Garcia, R.R. and S. Solomon, A new numerical model of the middle atmosphere: 2. Ozone and related species, *J. Geophys. Res.*, 99, 12,937–51, 1994.

Hausmann, M. and U. Platt, Spectroscopic measurement of bromine oxide and ozone in the high Arctic during Polar Sunrise Experiment 1992, *J. Geophys. Res.*, 99, 25,399–413, 1994.

Lary, D.J., Gas phase atmospheric bromine photochemistry, *J. Geophys. Res.*, 101, 1505–16, 1996.

McElroy, M.B., R.J. Salawitch, S.C. Wofsy, and J.A. Logan, Reductions of Antarctic ozone due to synergistic interactions of chlorine and bromine, *Nature*, 321, 759–62, 1986.

Salawitch, R.J., D. K. Weisenstein, L. J. Kovalenko, C. E. Sioris, P. O. Wennberg, K. Chance, M. K. W. Ko, and C. A. McLinden, Sensitivity of ozone to bromine in the lower stratosphere, *Geophys. Res. Lett.*, 32, L05811, doi: 10.1029/2004GL021504, 2005.

Stimpfle, R. M., D. M. Wilmouth, R. J. Salawitch, and J. G. Anderson, First measurements of ClOOCl in the stratosphere: The coupling of ClOOCl and ClO in the Arctic polar vortex, *J. Geophys. Res.*, 109, D03301, doi: 10.1029/2003JD003811, 2004.

Toohey, D.W., J.G. Anderson, W.H. Brune, and K.R. Chan, In *situ* measurements of BrO in the Arctic stratosphere, *Geophys. Res. Lett.*, 17, 513–16, 1990.

Wamsley, P.R., J.W. Elkins, D.W. Fahey, G.S. Dutton, C.M. Volk, R.C. Myers, S.A. Montzka, J.H. Butler, A.D. Clarke, P.J. Fraser, L.P. Steele, M.P. Lucarelli, E.L. Atlas, S.M. Schauffler, D.R. Blake, F.S. Rowland, W.T. Sturges, J.M. Lee, S.A. Penkett, A. Engel, R.M. Stimpfle, K.R. Chan, D.K. Weisenstein, M.K.W. Ko, and R.J. Salawitch, Distribution of halon-1211 in the upper troposphere and lower stratosphere and the 1994 total bromine budget, *J. Geophys. Res.*, 103, 1513–26, 1998.

Wennberg, P.O., R.C. Cohen, R.M. Stimpfle, J.P. Koplow, J.G. Anderson, R.J. Salawitch, D.W. Fahey, E.L. Woodbridge, E.R. Keim, R.S. Gao, C.R. Webster, R.D. May, D.W. Toohey, L.M. Avallone, M.H. Proffitt, M.

Loewenstein, J.R. Podolske, K.R. Chan, and S.C. Wofsy, Removal of stratospheric O_3 by radicals: *In situ* measurements of OH, HO_2, NO, NO_2, ClO, and BrO, *Science*, 266, 398–404, 1994.

Wilmouth, D. M., Laboratory studies and *in situ* stratospheric observations of inorganic chlorine and bromine species critical to catalytic ozone destruction, Ph.D. thesis, Harvard Univ., Cambridge, Mass, 2002.

Wofsy, S.C., M.B. McElroy, and Y.L. Yung, The chemistry of atmospheric bromine, *Geophys. Res. Lett.*, 2, 215–18, 1975.

World Meteorological Organization (WMO), Scientific assessment of ozone depletion: 1994, *WMO Rep. 37*, Global Ozone Res. and Monit. Proj., Geneva, Switzerland, 1995.

World Meteorological Organization (WMO), Scientific assessment of ozone depletion: 2002, *WMO Rep. 47*, Global Ozone Res. and Monit. Proj., Geneva, Switzerland, 2003.

Section 2: Observations of the NO_2 Radical with the Newly Developed Laser Induced Fluorescence Instrument both Inside and Outside the Arctic Polar Vortex

Extensive *in situ* observations of NO_2, NO, ClO, $ClONO_2$, O_3, temperature and pressure during the SAGE III Ozone loss and Validation Experiment (SOLVE) are used for the first study of the $ClONO_2/NO_2$ and NO/NO_2 exchange inside the polar vortex over a three-month period and a large dynamic range of ClO (75-1400 pptv) using *in situ* data. The measurements during SOLVE show extremely low (< 5 pptv) NO_2 concentrations inside the polar vortex throughout the entire measurement period resulting from high chlorine activation and severe denitrification in the 1999/2000 arctic polar vortex. The $ClONO_2/NO_2$ and NO/NO_2 systems were studied quantitatively inside and outside the polar vortex and both NO_2 and $ClONO_2$ mixing ratios calculated with steady-state approximations agree well with observed NO_2 and $ClONO_2$ values. This shows that current understanding describes the NO/NO_2 system in the stratosphere well for extra-vortex and in-vortex air masses.

Introduction

The odd nitrogen radicals ($NO_x \equiv NO + NO_2$) play an important role in the chemistry controlling the abundance of stratospheric ozone (Crutzen, 1970; Crutzen, 1971; Johnston, 1992; Wennberg, Cohen *et al.*, 1994; Anderson, 1995; Molina, Molina *et al.*, 1996; Solomon, Portmann *et al.*, 1998; Solomon, 1999; Zondlo, Hudson *et al.*, 2000; Cohen and Murphy, 2003). Although NO_x radicals directly remove ozone through catalytic cycling of NO and NO_2, they also buffer the destruction of ozone via catalytic cycles involving the halogen and hydrogen radicals (Wennberg, Cohen *et al.*, 1994; Cohen and Murphy, 2003). Specifically, the removal of ozone through catalytic cycles involving chlorine is moderated by NO_2 through its control of the partitioning between ClO, which is active in ozone destruction, and $ClONO_2$, which is inactive. For this reason, both the partitioning of NO_x between NO and NO_2 and the $NO_2/ClONO_2$ system have been studied in detail (DelNegro, Fahey *et al.*, 1999; Stimpfle, Cohen *et al.*, 1999). Studies using *in situ* data obtained during the Photochemistry in the Arctic Region in Summer (POLARIS) mission in 1997 showed that the NO/NO_2 and $NO_2/ClONO_2$ exchange processes in the continuously sunlit polar summer stratosphere are well understood (DelNegro, Fahey *et al.*, 1999; Stimpfle, Cohen *et al.*, 1999). The SOLVE mission in 2000 allowed the first such study for a polar region in winter for air masses both outside and inside of the polar vortex—the dominant dynamical feature of the polar winter stratosphere, which sets the conditions for the formation of the ozone hole. Although the chemical and dynamical properties of the polar vortex and ozone hole have been well established, the SOLVE mission provided the first *in situ* polar vortex measurements of NO_2, $ClONO_2$ and ClOOCl, species central to ozone depletion chemistry.

The qualitative evolution of NO_2, $ClONO_2$ and ClO during the polar winter and spring is well known for stratospheric air masses: During the polar night NO_x is effectively removed, as

expected for nighttime conditions, and in the vortex polar stratospheric clouds result in activation of chlorine (formation of Cl_2, HOCl and ClOOCl) in conjunction with removal of $ClONO_2$ (and HCl). When the sun rises, conditions inside the polar vortex are therefore quite unusual. The polar sunrise restarts the production of NO_2 from NO_x reservoir species, NO_y ($NO_y = HNO_3 + ClONO_2 + HNO_4 + N_2O_5 + \ldots$), but NO_2 production can be slow due to denitrification (removal of NO_y). In contrast to air masses outside of the vortex virtually all NO_2 that is produced reacts with ClO while it persists at extremely high concentrations to form $ClONO_2$. As a result, NO_2 concentrations are expected to stay extremely low for a substantial time after the polar sunrise.

Figure 2-1 demonstrates the striking difference between the two types of air masses encountered during SOLVE: Compared to the background stratosphere the vortex air masses show extremely low NO_2 concentrations (< 10 pptv). In the early phases of SOLVE $ClONO_2$ was below the detection limit (<100 pptv), whereas by March 11 moderate $ClONO_2$ concentrations (>500 pptv) were observed in the vortex. This shows that by March 11 a substantial amount of NO_2 has been produced, but has reacted with ClO, which persists at high concentrations, to form $ClONO_2$, a reaction central to shutting down catalytic ozone destruction. Interestingly, both catalytic ozone destruction and NO_2 production are initiated by the polar sunrise and the severity of the ozone hole largely reflects the competition between these two processes (the other significant part being chlorine deactivation to HCl). The central role NO_2 thus plays in controlling halogen induced ozone loss together with the large differences between conditions in the polar vortex and the previously studied background stratosphere calls for a detailed and quantitative test of our understanding of NO_2 chemistry under the conditions of the vortex.

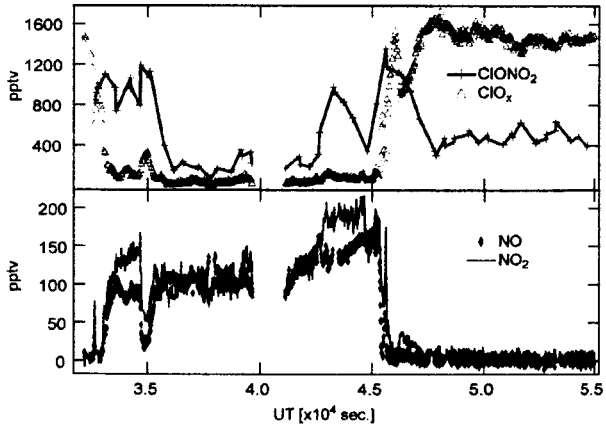

Figure 2-1. ClO_x ($ClO+2ClOOCl$) and $ClONO_2$ (a) and NO and NO_2 (b) mixing ratios are shown for the vortex edge crossing flight of 11 March 2000. The flight begins in the vortex, crosses to outside the vortex at UT = 32500 s, and back into the vortex at UT = 45000 s. Inside the vortex NO_x levels are close to 0 pptv and reflect the severe denitrification of the arctic vortex. The measurements during SOLVE represent the first *in-situ* observation of NO_2 in the arctic vortex. ClO_x mixing ratios varied from less than 100pptv outside the vortex and ~ 1500 pptv inside the vortex. On this flight some of the highest $ClONO_2$ mixing ratios ever measured on the ER-2 were observed.

Measurements

ER-2 Payload

During the SOLVE campaign (winter of 1999/2000) simultaneous *in situ* measurements were obtained aboard the NASA ER-2 aircraft deployed out of Kiruna, Sweden (68 N, 20 E). In this paper, observations of NO_2, NO, ClO, $ClONO_2$, O_3, temperature and pressure during the second phase of SOLVE, 15 February–16 March 2000, are used. The accuracies and references are listed in Table 2-1. The data are used as reported and averaged into 10 second intervals (unless reported otherwise) with the exception of BrO, for which $BrO = 0.5\ Br_y$, where Br_y is determined from the empirical Br_y-N_2O relation.(Wamsley, Elkins *et al.*, 1998).

Table 2-1. The 1-σ uncertainties of the NASA ER-2 *in situ* measurements.

Species	Accuracy	Reference
NO_2	±10%±5pptv	This work
NO	±6% ±4pptv	(Fahey *et al.* 1989)
$ClONO_2$	±20%	(Stimpfle *et al.* 1999)
ClO	±15%	(Brune *et al.* 1989a)
O_3	±5%	(Proffitt *et al.* 1989)
HO_2	±20% ± 0.02pptv	(Wennberg *et al.* 1994)
BrO	±15%	(Brune *et al.* 1989b)
Pressure	±0.25 mbar	(Chan *et al.* 1989)
Temperature	±0.3 K	(Chan *et al.* 1989)
J	±30%	

Measurement of NO_2

NO_2 was measured by a laser-induced fluorescence (LIF) technique with a instrument based on that successfully employed during the POLARIS mission.(Perkins, 2000; Perkins, Hanisco *et al.*, 2001) The NO_2 LIF technique offers direct detection of NO_2 without requiring chemical titration or processing. In addition, by making use of a spectrally narrow (0.04 cm^{-1}) feature in the NO_2 spectrum at 585 nm, the instrument achieves a highly selective measurement of NO_2 by discerning between the radical fluorescence and N_2-Raman scattering or other spectral interferences. For SOLVE the instrument was modified by substituting the Ga:As Photomultiplier Tubes (PMTs) used as detectors during POLARIS with Avalanche Photodiode Detectors (APDs). The APDs have a longer cut-off wavelength of 1000 nm compared with that of the PMT at 850 nm, but require a detailed characterization of the nonlinear response curve. Conversion of the retrieved NO_2 fluorescence signal to absolute NO_2 concentration requires a combination of laboratory and in-flight calibrations. The N_2-Raman scatter signal, which reflects the collection efficiency of the detection axis, is measured both in flight and in the laboratory. This allows the absolute NO_2 LIF sensitivity as a function of pressure and temperature, which was determined in the laboratory, to be tied directly to the sensitivity in flight via the N_2-Raman scatter signal measured during SOLVE. The sensitivity of the instrument is 5 pptv in 10 seconds with a signal-to-noise ratio of 2. During the course of the calibration possible spectral interferences from other species such as H_2O, CO_2 and O_3 were investigated. It was determined that introduction of O_3 can result in the production of NO_2 within the instrument, probably via reaction with N-containing species on exposed metal surfaces. This explains the observation of a consistent 14-15 pptv offset of the measured NO_2 mixing ratio during SOLVE, which we have subtracted in our analysis. The magnitude of the offset was determined by analyzing all data for which $[NO_2] \sim 0$ pptv. This requirement is fulfilled for air masses that have experienced darkness (defined as solar-zenith-angle >100°) at elevated ClO levels (>75 pptv). The offset, defined as the median measured NO_2 signal for these air masses, is 14.8±5 pptv. Further analysis of the data of the 20 January, 23 January, and 27 January 2000 flights showed interference NO_2 LIF signal resulting from the in-flight addition of NO_2 for calibration purposes. This interference signal was too large to allow a meaningful interpretation of the LIF signal from atmospheric NO_2 and, therefore, no NO_2 mixing ratios are reported for these flights. After 27 January 2000 NO_2 addition was only performed on one of the two detection axes, allowing the interference free observation of the LIF signal from atmospheric NO_2.

Calculations and analysis of steady-state concentrations of NO_2 and $ClONO_2$

The SOLVE mission has allowed the first analysis, based on *in-situ* measurements, of the differences in NO/NO_2 and $NO_2/ClONO_2$ exchange between background stratospheric air masses

and those that have been processed in the arctic vortex. The flight of 11 March 2000 highlights the large differences in composition between these two types of air masses (see Figure 2-1). The ER-2 crossed the vortex edge twice, starting out and terminating within it. The transition is quite sharp and can be seen in the changes of NO_2, NO, $ClO_x = ClO + 2ClOOCl$, and $ClONO_2$.

The concentrations of NO_2 and $ClONO_2$ are controlled by reactions 1–6 and reactions 7–9, respectively, which are listed in Table 2-2 (DelNegro, Fahey *et al.*, 1999; Stimpfle, Cohen *et al.*, 1999). In daylight NO_2 and $ClONO_2$ can be assumed to be in instantaneous photochemical steady-state (PSS) with production and loss being equal:

$$\frac{dNO_2}{dt} = k_{NO+O_3}[NO][O_3] + k_{NO+ClO}[NO][ClO] + k_{NO+BrO}[NO][BrO] + k_{NO+HO_2}[NO][HO_2] - J_{NO_2}[NO_2] - k_{NO_2+O}[NO_2][O] + J_{ClONO_2}[ClONO_2] - k_{NO_2+ClO}[NO_2][ClO] = 0 \quad \text{(eq. 1)}$$

$$\frac{dClONO_2}{dt} = -J_{ClONO_2}[ClONO_2] + k_{NO_2+ClO}[NO_2][ClO] = 0 \quad \text{(eq. 2)}$$

These equations are used for the first test of our understanding of NO/NO_2 and $NO_2/ClONO_2$ exchange inside the polar vortex using *in situ* observations.

Table 2-2. $NO_2 \leftrightarrow NO$ and $NO_2 \leftrightarrow ClONO_2$ Exchange Processes

		Fractional contributions	
		Extravortex	Vortex
$NO \rightarrow NO_2$			
$NO + O_3 \rightarrow NO_2 + O_2$	(1)	0.84 ± 0.07*	0.07 ± 0.01
$NO + ClO \rightarrow NO_2 + Cl$	(2)	0.13 ± 0.10*	0.92 ± 0.01
$NO + BrO \rightarrow NO_2 + Br$	(3)	0.02 ± 0.01	<0.01
$NO + HO_2 \rightarrow NO_2 + OH$	(4)	<0.01	<0.01
$NO_2 \rightarrow NO$			
$NO_2 + h\nu \rightarrow NO + O$	(5)	0.998 ± 0.0003	0.999
$NO_2 + O \rightarrow NO + O_2$	(6)	0.002 ± 0.0003	0.001
$ClONO_2 \rightarrow NO_2$			
$ClONO_2 + h\nu \rightarrow ClO + NO_2$	(7)		
$ClONO_2 + h\nu \rightarrow Cl + NO_3$	(8)		
$NO_2 \rightarrow ClONO_2$			
$NO_2 + ClO \rightarrow ClONO_2$	(9)		

*The deviations correspond to variations in ozone not an uncertainty in a measurement or rate constant.

Analysis of NO/NO_2 exchange and NO_2 photochemical steady-state

In the analyses that follow all data are restricted to solar-zenith-angle (sza) < 90° to ensure that the NO/NO_2 steady-state is valid and number densities < 2.4×10^{18} molec/cc to restrict the data to stratospheric air at cruise altitude, unless otherwise stated; the vortex is defined as [ClO] > 900 pptv and extra-vortex as [ClO] < 145 pptv to ensure exclusion of vortex edge air masses.

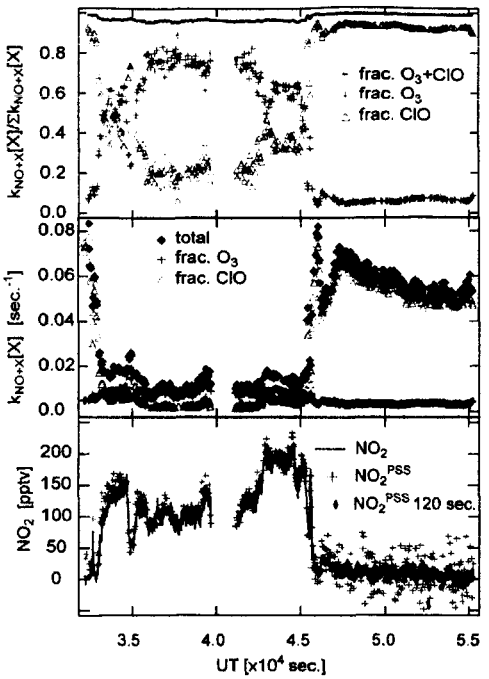

Figure 2-2. The contributions of individual first order NO → NO_2 rates calculated with rate constants from JPL-00 for the flight of 11 March 2000 are shown. The fractional contribution of NO → NO_2 conversion is shown for the flight of 11 March 2000 (a). The data are restricted to M < 2.4×10^{18} molecules/cm and solar zenith angles < 90°. The first order rates were calculated using JPL-00 rates and observed ClO, O_3, temperature, pressure, and photolysis rates from overhead ozone. Inside the vortex ClO controls this conversion, whereas outside of the vortex this reaction still contributes significantly but reaction with O_3 is most important. The first order rates for conversion of NO → NO_2 are shown (b), which demonstrates that the transition from O_3 to ClO controlled chemistry results mainly from a more than tenfold increase in the reaction rate of $k_{ClO+NO}[ClO]$ rather than from the moderate (~ 50%) decrease in the reaction rate of $k_{O3+NO}[O_3]$. The contribution of BrO and HO_2 to overall NO_2 production is always smaller than 5%. Calculated NO_2^{PSS} and observed NO_2^{obs} concentrations agree very well outside of the vortex (c). Inside the vortex the scatter in NO_2^{PSS} is large as NO is ~0 pptv, but 120-second averaged data show good agreement.

Figure 2-2a shows the fractional contributions of the NO + O_3 and NO + ClO reactions to overall NO → NO_2 conversion for 11 March 2000 using JPL 02 rates. Reaction (1), NO + O_3, contributes between 50–80% of overall NO → NO_2 conversion outside of the vortex. In contrast, the median contribution of reaction (1) inside the vortex is only 6% and the median contribution of reaction (2), NO+ClO, is 93%. The figure also shows that reactions (1) and (2) always contribute >95% of overall NO → NO_2 conversion. Thus NO/NO_2 exchange and the NO_2 photochemical steady-state concentration (NO_2^{PSS}) can be approximated with the following equations:

$$NO_2^{PSS} \approx \frac{(k_{NO+O_3}[O_3] + k_{NO+ClO}[ClO])[NO]}{J_{NO_2}} \qquad \text{(eq. 3)}$$

This equation illustrates both the competition between O_3 and ClO in the oxidation of NO to NO_2 and that NO_2^{PSS} is determined by the ratio of NO oxidation and NO_2 photolysis flux. On 11 March the large difference in the fractional contributions of O_3 and ClO to the overall conversion of NO to NO_2 between extra-vortex and vortex air masses mainly results from a ca. 16-fold increase in the absolute rate of reaction (2), NO + ClO, in the vortex (see Figure 2-2b). In contrast, the absolute NO_2 production rate of reaction (1), NO + O_3, inside the vortex is only reduced by about 60% compared to the one outside of the vortex. The large increase in the rate of reaction (2) results from very high ClO concentrations, a result of the high degree of chlorine activation. The reduction in the rate of reaction (1) results from smaller O_3 concentrations in the vortex compared with air masses outside of the vortex, which mainly is a result of catalytic ozone destruction.

The median contributions for the entire analyzed data set, consisting of the flights of 14, and 31 January, 02, 03, and 26 February, and 05, 07, 11, 12, and 16 March 2000 (only few data points with sza < 90° exist for the first three of these flights) are shown in Table 3. The contributions of reactions (3) and (4) are not significant with median contributions of < 2% and less than 5% contribution even at their maximum. For this dataset the median contribution of

reaction (1) and (2) outside the vortex are 86% and 12%, respectively, with a fairly large variability (see Table 2-2). This variability results from variations in the O_3 concentration rather than uncertainty in measurements. Inside the vortex reaction (1) only contributes 7% to overall NO → NO_2, whereas reaction (2) contributes 92%. The transition from extra-vortex to vortex is thus clearly accompanied by a dramatic change from an ozone controlled NO → NO_2 conversion to a ClO controlled one, reflecting the large difference in chemical composition of these air masses. The extent of the transition region between these two regimes is quite narrow and only few observations with intermediate contributions of reactions (1) and (2) exist.

Table 2-3 shows the absolute and fractional contributions of reaction (1) and (2) inside the vortex for the individual flights of 31 January, 02, and 26 February, and 05, 07, 11, and 12 March 2000. Whereas no clear trend is apparent for the absolute rate of reaction (2), a steady decrease in that of reaction (1) is evident, so that by 12 March a ca. 50% reduction in the fractional contribution of reaction (1) is observed compared to 31 January. This trend results from the decreasing O_3 concentrations due to catalytic processes in many of which ClO plays an important role. The observation that the absolute rate of reaction (2) is not much reduced by 12 March shows that the level of chlorine activation is not significantly reduced at this point (see next section). The fact that the vortex is fairly well isolated from the rest of the stratosphere allows such an interpretation even though it can certainly not be expected that the same actual air mass be sampled successively during these flights.

Table 2-3.

Date	$k_{NO+ClO}[ClO]$	$k_{NO+O_3}[O_3]$	$\frac{k_{NO+ClO}[ClO]}{\sum k_{NO+X}[X]}$	$\frac{k_{NO+O_3}[O_3]}{\sum k_{NO+X}[X]}$	$\left(\frac{NO}{NO_2}\right)_{calc}$	$\left(\frac{NO}{NO_2}\right)_{obs}$
31 January	0.055 s^{-1}	0.0082 s^{-1}	0.86	0.13	0.06	0.06
02 February	0.077 s^{-1}	0.0080 s^{-1}	0.90	0.09	0.09	0.09
26 February	0.062 s^{-1}	0.0058 s^{-1}	0.91	0.08	0.10	0.10
05 March	0.055 s^{-1}	0.0050 s^{-1}	0.90	0.08	0.09	0.09
07 March	0.067 s^{-1}	0.0051 s^{-1}	0.93	0.07	0.12	0.12
11 March	0.055 s^{-1}	0.0036 s^{-1}	0.93	0.06	0.14	0.14
12 March	0.051 s^{-1}	0.0041 s^{-1}	0.92	0.07	0.16	0.16

Beyond this qualitative analysis of NO/NO_2 exchange a comparison of calculated NO_2^{PSS} with measured NO_2, $NO_2^{obs.}$, allows a quantitative test of our understanding of the reactions controlling NO_2 concentrations. Figure 2-2c shows a comparison of NO_2^{PSS} with $NO_2^{obs.}$ for the flight of March 11 2000. The agreement is excellent outside the vortex; median NO_2^{PSS} =1.05 $NO_2^{obs.}$, which agrees well with the analysis by DelNegro *et al.* for the POLARIS mission. Inside the vortex median NO_2^{PSS} = 1.17% $NO_2^{obs.}$. The good agreement within the vortex is more readily observable for NO_2^{PSS} calculated with 120-second averaged data (see Figure 2-2c).

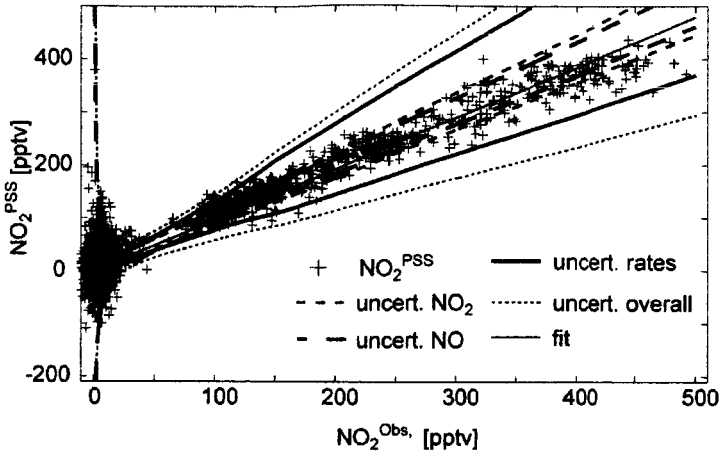

Figure 2-3. A comparison of the calculated NO_2^{PSS} (using JPL-02 rates and observed NO, ClO, O_3, temperature, pressure, and photolysis rates from overhead ozone) and measured NO_2 mixing ratios for the second part of SOLVE is shown. The green dashed lines (- -) show the uncertainty of the NO_2 measurement in relation to the observed NO_2. At low NO_2 mixing ratios the scatter in NO_2^{PSS} is very large as NO ~0 pptv and accordingly the uncertainty in NO_2^{PSS} is dominated by the uncertainty from NO (blue double dashed line - –). At high NO_2 mixing ratios the uncertainty in NO_2^{PSS} is dominated by the uncertainty from the rate constants (solid red line). The data are restricted to $M < 2.4 \times 10^{18}$ molecules/cm and solar zenith angles < 90°.

Figure 2-3 shows a graph of calculated NO_2^{PSS} versus $NO_2^{obs.}$ for the flights of 14, and 31 January, 02, and 26 February, and 05, 07, 11, 12, and 16 March 2000 (only few data points with sza < 90° exist for the first three of these flights). Two regimes can be distinguished: The first is the extra vortex data with NO_2 mixing ratios larger than 50 pptv, which are exclusively from the flights on 14 January, 11 and 16 March 2000. The majority of the data, which have NO_2 mixing ratios less than 50 pptv, represent the first reported *in situ* NO_2 mixing ratios from within the arctic vortex. The relative scatter in the calculated NO_2^{PSS} is large for these data points as [NO] is very small. Also shown in Figure 2-3 are the uncertainty in NO_2^{PSS} from the observed NO, the first order rates, and the overall uncertainty. [The uncertainties were calculated using fits of simple functional forms to the measured parameters.] At low NO_2 mixing ratios the overall uncertainty of NO_2^{PSS} is dominated by the uncertainty from NO, which is large as [NO] is very small. At NO_2 mixing ratios above 50 pptv the overall uncertainty is determined by the uncertainty in the pseudo first-order rates, $\Sigma k_{NO+X}[X]$. The figure shows that at all NO_2 mixing ratios few NO_2^{PSS} data points are outside of the overall uncertainty despite the large increase in the scatter of NO_2^{PSS} with decreasing NO_2 (and also NO). At high values of observed [NO_2] the calculated NO_2^{PSS} shows a slight negative deviation and a fit to a line forced through the origin has a slope of 0.96, well within the experimental uncertainty. Outside of the vortex NO_2^{PSS} is in excellent agreement with NO_2^{obs}; the median fractional error E in NO_2^{PSS}, $E = (NO_2^{PSS} - NO_2^{obs.})/NO_2^{obs.}$, is –0.5 ± 12% (standard deviation). For data inside the vortex agreement are also good and the median fractional error, E, is +26 ± 1600%. The large standard deviation reflects the large uncertainty in the observed NO concentrations.No correlation of the fractional error in NO_2^{PSS}, $E = (NO_2^{PSS} - NO_2^{obs})/ NO_2^{obs}$, was found with temperature or NO_2 photolysis rate within the uncertainty of these measurements. Therefore, an analysis of E as a function of $k_{ClO+NO}[ClO]/\Sigma k_{X+NO}[X]$, the fraction of NO → NO_2 conversion by reaction (2), can indicate possible systematic errors associated with k_{ClO+NO} or k_{O3+NO}. Figure 2-4 shows E as a function of $k_{ClO+NO}[ClO]/\Sigma k_{X+NO}[X]$ for the flights of 14, and 31 January, 02, and 26 February, and 05, 07, 11, 12, and 16 March 2000. The 60-second data are restricted to $M < 2.4 \times 10^{18}$ and to extra vortex measurements (ClO < 145 pptv) as the scatter in the vortex NO_2^{PSS} data is very large. E is determined by $k_{O3+NO}[O_3]$ if the abscissa equals 0 and by $k_{ClO+NO}[ClO]$ if it equals 1. The fit of E to a line indeed shows a slope that indicates an underestimate (–3%) of NO_2^{PSS} from reaction (1) and a slightly larger overestimate (+25%) from reaction (2). However, these deviations are within the uncertainties resulting from the NO_x ($NO_x = NO + NO_2$) measurements as well as the

uncertainty associated with the pseudo first-order rate constants. Overall, the first order rates agree with the observations within the uncertainty of the NO/NO_2 ratio, which is ca. 20% for the data shown in Figure 2-4.

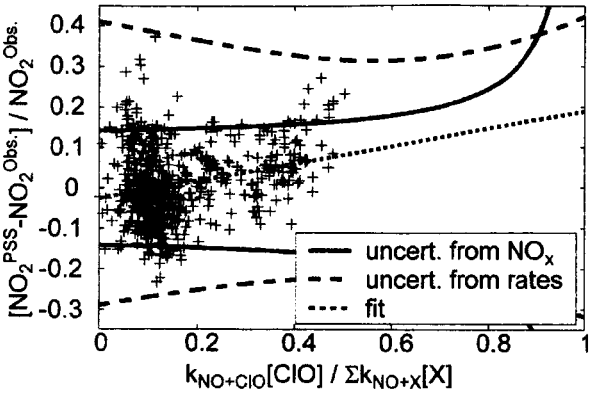

Figure 2-4. The fractional error in NO_2^{PSS}, $E = (NO_2^{PSS} - NO_2^{obs})/NO_2^{obs}$, is shown as function of the fractional contribution of reaction (1) to overall NO_2 production $k_{ClO+NO}[ClO]/\Sigma k_{X+NO}[X]$. E is a function of for the flights of 14, and 31 January, 02, and 26 February, and 05, 07, 11, 12, and 16 March 2000. The 60-second data are restricted to $M < 2.4 \times 10^{18}$ and to extra vortex measurements ($ClO < 145$ pptv) as the scatter in the vortex NO_2^{PSS} data is very large. The deviations of fit of E to a line are within the uncertainties resulting from the NO_x ($NO_x = NO + NO_2$) measurements as well as the uncertainty associated with the pseudo first-order rate constants.

Analysis of $ClONO_2$ photochemical steady-state

The concentration of $ClONO_2$ is controlled by reactions (7–9) listed in Table 2-3, and the $ClONO_2$ instantaneous steady-state can be expressed from equation 2:

$$ClONO_2^{PSS} = \frac{k_{NO_2+ClO}[ClO][NO_2]}{J_{ClONO_2}} \qquad \text{(eq. 5)}$$

Figure 2-5 shows a comparison of $ClONO_2^{PSS}$ calculated using JPL-00 rates, and 120-second averaged measured temperature, pressure, ClO, NO_2, and photolysis rates with observed $ClONO_2$ for the flight of 11 March 2000. The agreement between median calculated and median observed $ClONO_2$ is very good ($ClONO_2^{PSS} = 1.16 \pm 0.39 \times ClONO_2$) both outside ($ClONO_2^{PSS} = 1.15 \pm 0.32 \times ClONO_2$) and inside ($ClONO_2^{PSS} = 1.20 \pm 0.28 \times ClONO_2$) the vortex. These values are within the combined uncertainties of NO_2 and ClO. As in the analysis of NO_2^{PSS} the data are restricted to number densities $< 2.4 \times 10^{18}$ molec/cc to restrict the data to stratospheric air at cruise altitude and sza < 90° as an estimate of the validity of the $ClONO_2$ steady-state. However, the $ClONO_2/NO_2$ photochemical steady-state is typically achieved more slowly than the NO/NO_2 one. For the more rigorous analysis of the agreement between $ClONO_2^{PSS}$ and observed $ClONO_2$ that follows only data, for which this steady-state approximation is expected to be valid are used. The fulfillment of this requirement was established by comparing $ClONO_2$ concentrations calculated using a time-dependent, zero-dimensional photochemical model with $ClONO_2^{PSS}$. The time-dependent model used here only included reactions 7-9 as well as ClO dimer formation and dissociation. Figure 2-6a shows the results of this calculation for the flights of February 26, March 5, March 7, March 11, March 12, and March 16, 2000, and number densities $< 2.4 \times 10^{18}$ molec/cc. At sza > 85° the photolysis rate becomes too slow for the instantaneous PSS to be a good approximation of the $NO/ClONO_2$ system. In contrast, the instantaneous PSS approximation is expected to be quite accurate near local noon (at small solar-zenith angles). During the flight of 11 March 2000 deviations at smaller solar-zenith angles (65–75°) were observed in outside vortex air masses. These air masses had very low ClO concentrations resulting in a NO_2 + ClO rate, that was to slow to allow the instantaneous PSS to be valid.

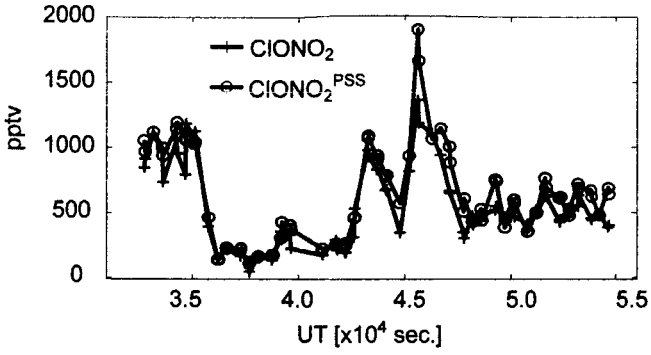

Figure 2-5. A comparison of observed $ClONO_2$ and $ClONO_2^{PSS}$ calculated using JPL-02 rates, and 120-second averaged measured temperature, pressure, ClO, NO_2, and photolysis rates from overhead ozone with observed $ClONO_2$ for the flight of 11 March 2000 is shown. The data are restricted to $M < 2.4 \times 10^{18}$ molecules/cm and solar zenith angles < 90°. The agreement between median calculated and median observed $ClONO_2$ is very good ($ClONO_2^{PSS}$=1.16±0.39 × $ClONO_2$) both outside ($ClONO_2^{PSS}$ =1.15±0.32 × $ClONO_2$) and inside ($ClONO_2^{PSS}$ =1.20±0.28 × $ClONO_2$) the vortex.

For the analysis in Figure 2-6b only data points for which agreement of steady-state and time dependent model was within 5%, and $M < 2.4 \times 10^{18}$ were chosen. The scatter in the 60-second $ClONO_2^{PSS}$ is large, resulting from the very low NO_2 concentrations, which determine the overall uncertainty in $ClONO_2^{PSS}$; however, averaged $ClONO_2^{PSS}$, shown as the circles, agrees well with observed $ClONO_2$. The slope of a line-fit of this averaged $ClONO_2^{PSS}$ *versus* averaged $ClONO_2$ through the origin gives a slope of 1.05 and the median (not averaged) fractional error, $(ClONO_2^{PSS} - ClONO_2)/ClONO_2$, is 17%. Outside of the vortex the median (not averaged) fractional error, $(ClONO_2^{PSS} - ClONO_2)/ClONO_2$, is 33 ± 29% (standard deviation) and inside the vortex it is +4 ± 117%. This agreement is remarkably good, especially considering the extremely low NO_2 concentrations and the fact that the PSS is not required to be valid to better than ± 5%.

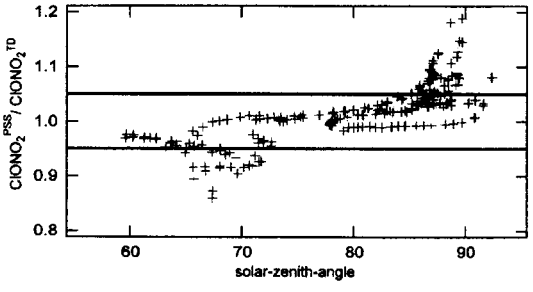

Figure 2-6a. A comparison between $ClONO_2$ concentrations calculated using a time-dependent, zero-dimensional photochemical model with $ClONO_2^{PSS}$ for the flights of February 26, March 5, March 7, March 11, March 12, and March 16, 2000, and number densities < 2.4×10^{18} molec/cc. At sza > 85° the photolysis rate becomes too slow for the instantaneous PSS to be a good approximation of the $NO/ClONO_2$ system.

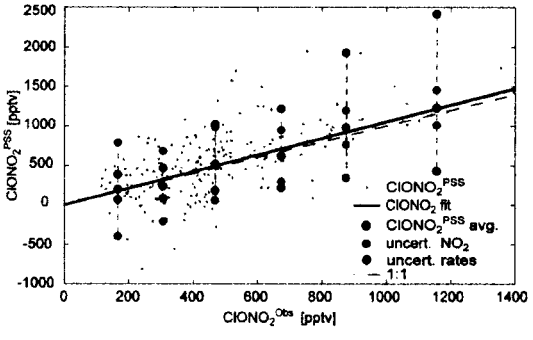

Figure 2-6b. A comparison between $ClONO_2^{PSS}$ and observed $ClONO_2$ for data points for which agreement of steady-state and time dependent model was within 5%, and $M < 2.4 \times 10^{18}$. The scatter in the 60-second $ClONO_2^{PSS}$ is large, resulting from the very low NO_2 concentrations, which determine the overall uncertainty in $ClONO_2^{PSS}$; however, averaged $ClONO_2^{PSS}$, shown as the circles, agrees well with observed $ClONO_2$. The slope of a line-fit of this averaged $ClONO_2^{PSS}$ *versus* averaged $ClONO_2$ through the origin gives a slope of 1.05 and the median (not averaged) fractional error, $(ClONO_2^{PSS} - ClONO_2)/ClONO_2$, is 17%. Outside of the vortex the median (not averaged) fractional error, $(ClONO_2^{PSS} - ClONO_2)/ClONO_2$, is 33 ± 29% (standard deviation) and inside the vortex it is +4 ± 117%. This agreement is remarkably good, especially considering the extremely low NO_2 concentrations and the fact that the PSS is not required to be valid to better than ± 5%.

Implications

SOLVE allowed the first *in situ* measurements of NO_2 and $ClONO_2$ in a severely denitrified and processed arctic vortex, and the analysis of $NO/NO_2/ClONO_2/ClO$ exchange

using photochemical steady-state models over a wide range of ClO concentrations. This analysis shows that calculated and observed NO_2 are in excellent agreement for the entire data set, which demonstrates that in the stratosphere the NO/NO_2 system is well described for extra-vortex and in-vortex air masses by equations 1–6 in Table 2-2. The measurements show that NO_2 concentrations inside the vortex remain low throughout the entire deployment as a result of a high degree of chlorine activation and denitrification.

Comparison of calculated and observed $ClONO_2$ mixing ratios is of particular importance with respect to the chlorine budget as it allows a validation of the $ClONO_2$ contribution to the budget. The comparison shows excellent agreement for the entire data set, well within both the uncertainties of the $ClONO_2$ measurement and the uncertainties arising from the rate constants.

The combined analyses show that the $NO/NO_2/ClONO_2/ClO$ dataset is consistent with model calculations and confirms our understanding of the gas phase chemistry governing this system. Despite the good agreement between calculated and observed NO_2 and $ClONO_2$ concentrations, the large uncertainties in the calculated NO_2 and $ClONO_2$ demonstrate the value of the *in-situ* observations. Especially for models using $ClONO_2$ the uncertainty of calculated $ClONO_2$ if only NO and no NO_2 observations are available is very large and thus would result in large uncertainties for the chlorine budget without measurements of $ClONO_2$ and NO_2.

References

Anderson, J. G. (1995). *Progress and Problems in Atmospheric Chemistry*. J. R. Barker. Singapore, World Scientific. **3**.

Brune, W.H., J.G. Anderson, and K.R. Chan, In situ observations of ClO over Antarctica: ER-2 Aircraft results from 54°S to 72°S latitude. *J. Geophys. Res.*, 1989. **94**: p. 16,649–63.

Brune, W.H., J.G. Anderson, and K.R. Chan, In situ observations of BrO over Antarctica: ER-2 Aircraft results from 54°S to 72°S latitude. *J. Geophys. Res.*, 1989. **94**: p. 16,639–47.

Chan, K.R., et al., Temperature and horizontal wind measurements on the ER-2 aircraft during the 1987 airborne Antarctic ozone epxeriment. *J. Geophys. Res.*, 1989. **94**: p. 11,573–87

Cohen, R. C. and J. G. Murphy (2003). "Photochemistry of NO2 in Earth's Stratosphere: Constraints from Observations." *Chem. Rev.* **103**: 4985–98.

Crutzen, P. J. (1970). *Q. J. R. Meteorol. Soc.* **96**: 320.

Crutzen, P. J. (1971). *J. Geophys. Res.* **76**: 7311.

DelNegro, L., D. W. Fahey, *et al.* (1999). "Comparison of modeled and observed values of NO2 and JNO2 during the Photochemistry of Ozone Loss in the Arctic region in Summer (POLARIS) mission." *J. Geophys. Res.* **104**(D21): 26,687–705.

Fahey, D.W., et al., *In situ measurements of total reactive nitrogen, total water, and aerosol in a polar stratospheric cloud in the Antarctic.* J. Geophys. Res., 1989. **94**: p. 11,299–315.

Johnston, H. S. (1992). *Ann. Rev. Phys. Chem.* **43**: 1.

Molina, M. J., L. T. Molina, *et al.* (1996). *Ann. Rev. Phys. Chem.* **47**: 327.

Perkins, K. K. (2000). In Situ Observations of Nitrogen Dioxide using Laser-Induced Fluorescence Detection: Examining the NO_2-HNO_3 System in the Lower Stratosphere. *Earth and Planetary Sciences*. Cambridge, Harvard University: 145.

Perkins, K. K., T. F. Hanisco, *et al.* (2001). "The NO_x-HNO_3 system in the lower stratosphere: Insights from *in situ* measurements and implications of the J(HNO_3)-[OH] relationship." *J. Phys. Chem. A* **105**: 1521–34.

Proffitt, M.H., *et al., In situ* ozone measurements within the 1987 Antarctic ozone hole from a high-altitude ER-2 aircraft. *J. Geophys. Res.*, 1989. **94**: p. 16,547–55.

Solomon, S. (1999). *Rev. Geophys.* **37**: 275.

Solomon, S., R. W. Portmann, et al. (1998). *Geophys. Res. Lett.* **25**: 1871.

Stimpfle, R. M., R. C. Cohen, et al. (1999). "The coupling of ClONO2, ClO, and NO2 in the lower stratosphere from in situ observations using the NASA ER-2 aircraft." *J. Geophys. Res.* **104**(D21): 26,705–14.

Wamsley, P. R., J. W. Elkins, et al. (1998). "Distribution of Halon-1211 in the upper troposphere and lower stratosphere and the 1994 total bromine budget." *J. Geophys. Res.* **103**(D1): 1513–26.

Wennberg, P.O., et al., Aircraft-borne laser-induced fluorescence instrument for the in situ detection of hydroxyl and hydroxyperoxyl radicals. *Rev. Sci. Instrum.*, 1994. **65**: p. 1858–76.

Wennberg, P. O., R. C. Cohen, et al. (1994). "Removal of Stratospheric O_3 by radicals—In Situ measurements of OH, HO_2, NO, NO_2, ClO and BrO." *Science* **266**(5184): 398-404.
Zondlo, M. A., P. K. Hudson, *et al.* (2000). *Ann. Rev. Phys. Chem.* **51**(473).

Section 3: Deployment of and Laboratory Absolute Calibration of *in situ* Water Vapor and Total Water Instruments on the NASA WB-57 Aircraft in the CRYSTAL-FACE, and AVE Missions

We describe the performance and in-flight validation of an instrument mounted in a pallet on the NASA WB-57 research aircraft that measures the sum of gas phase and solid phase water, or total water, in cirrus clouds. Using a heated isokinetic inlet and Lyman-α photofragment fluorescence technique for detection, measurements of total water have been made over three orders of magnitude. During CRYSTAL FACE, the instrument operated at duct temperatures sufficiently warm to completely evaporate particles up to 150-μm diameter. Laboratory calibrations, in-flight diagnostics, intercomparison with water vapor measured by absorption in flight, and intercomparisons in clear air with the Harvard water vapor instrument validate the detection sensitivity of the instrument and illustrate the minimal hysteresis from instrument surface contamination. The Harvard total water and water vapor instruments together provide measurements of the ice water content of thin cirrus clouds in the tropopause region with a 9% uncertainty and thicker cirrus clouds in the upper troposphere with an uncertainty of 17%.

Introduction

In Weinstock *et al.* [2005a], we describe the motivation, design criteria, and laboratory calibrations for the Harvard total water instrument. We describe here the in-flight validation of this instrument that combines an isokinetic inlet, a heated duct, and a photofragment fluorescence detection axis for the quantitative measurement of the total water content of a cloud. The flights we use for validation took place on the NASA WB-57 research aircraft during test flights from Houston TX in May, 2001, the Clouds and Water Vapor in the Climate System mission (CWVCS) based out of San Jose, Costa Rica in the summer of 2001, and the Cirrus Regional Study of Tropical Anvils and Cirrus Layers-Florida Area Cirrus Experiment, (CRYSTAL FACE), from Key West, Florida, in July 2002. When combined with simultaneous water vapor measurements, instrument accuracy and response time can be evaluated in clear air, and ice water content can be determined when clouds are sampled.

The Harvard cloud ice water content (IWC) measurements were part of the WB-57 payload during CRYSTAL FACE to help satisfy one of its primary goals of developing the capability of modeling the radiative properties of thin cirrus using space-based millimeter wave measurements of the ice water paths within the cloud. Testing this capability first requires accurate *in situ* measurements of the microphysical properties of thin cirrus, including IWC, with simultaneous or nearly simultaneous measurements of the radiative properties of the sampled cloud. Calculations of the radiative effects of tropical thin cirrus [e.g. Stackhouse and Stephens, 1991] illustrate potential radiative heating effect of high altitude thin cirrus and its strong dependence on ice water content. For example, they calculate that for a $0.0002 g/m^3$ ice water content ($6.7e^{12}$ mol/cc), a 3-km thick cloud provides about 1.5 W/m^2 of infrared heating, and this heating scales directly with ice water content. In fact, McFarquhar *et al.*, [2000] report cloud radiative forcing calculations using microphysical and lidar data during the Central Equatorial Pacific Experiment averaging 1.58 W/m^2. Measurements of the potentially small ice water content of thin cirrus need to be accurate and precise enough to adequately constrain models calculating the radiative properties of these clouds because this additional heat source could measurably impact the slow ascent rates in the upper tropical troposphere.

Instrument performance and evaluation

Engineering flights for the total water instrument took place in May 2001 from the NASA Johnson Space Flight Center at Ellington Field, Houston, TX. All subsystems of the instrument performed successfully providing the opportunity to evaluate how well the instrument measures water vapor in cloud free air and total water in a cloud. In either case, the minimum success criteria are that the total water mixing ratio at the detection axis equals ambient total water and that the detection sensitivity to water vapor in flight is the same as that established by laboratory calibrations. Furthermore, it is essential that these criteria be met independently in both clear air and clouds. We will address the validation of the calibration by first intercomparing with the Harvard water vapor instrument, and then by using in-flight absorption measurements, and finally with the NASA JPL tunable diode laser multipass IR (JPL) hygrometer [May, 1998], the other water vapor instrument on the WB-57.

In 2005a we enumerated the potential sources of systematic error and their expected magnitudes. In this report we use examples of flight data to illustrate how successful we were in meeting our previous estimates. The issues we specifically address are:

1. Instrument hysteresis or wall effects that show up as unwanted or undesirable time constants in the total water measurement during rapid mixing ratios changes.
2. Validation of the detection sensitivity established by laboratory calibrations.
3. Complete evaporation of cirrus ice particles.

Instrument validation bears not only on the measurement accuracy of the water vapor and total water instruments, but also by extension on the issue of accurate water vapor measurements in general as addressed in the SPARC assessment of upper tropospheric and stratospheric water vapor [Kley *et al.*, 2000].

Hysteresis issues and intercomparisons of Harvard total water with Harvard water vapor: Clear air

An independent measurement of water vapor is needed along with the total water measurement to determine the ice water content of the sampled cloud. The Harvard water vapor instrument has served that purpose and has also proved invaluable in the validation of the total water measurements in clear air, a necessary step before evaluating its measurement in clouds. While the detection axes for the two instruments are virtually identical, the instruments operate in very different flow regimes. Flow rates in the total water vapor instrument are typically about 5-6 m/sec in a 5.08-cm rectangular cross section duct, providing a mass flow less than one tenth of that in the water vapor instrument. Accordingly, outgassing from instrument walls and hysteresis effects that have not been an issue in the water vapor instrument become a significant concern for the total water instrument.

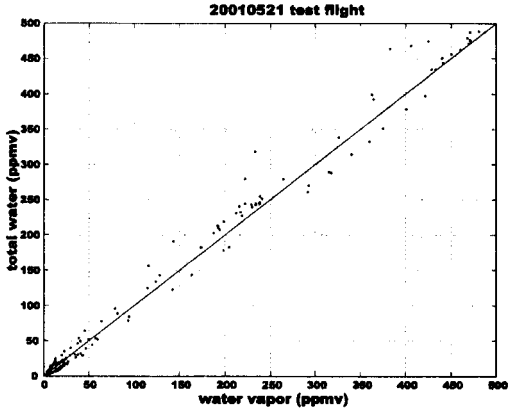

Figure 3-1. Plot of total water vs. water for the test flight out of Houston on May 21, 2001, illustrating general overall agreement of the two instruments for measuring water in clear air. The 1:1 line is added to illustrate agreement.

To explore this hysteresis issue, we show in Figure 3-1 water vapor measurements from the first test flight, on May 21, 2001, where total water is plotted against water vapor. Though agreement between the two instruments is typically better than 10%, this can be somewhat

misleading. While the scatter in the data would appear to be acceptably small, a closer look at the data is required. We show in Figure 3-2a water vapor as measured by the two instruments plotted vs. time. In Figures 3-2b and 3-2c are plots of ambient temperature and pressure respectively. Regardless of the absolute sensitivities of the two instruments, there are three labeled regions that display evidence of hysteresis, in which walls and surfaces of the total water instrument either act as sources or sinks for water vapor. The most obvious feature occurs at the beginning of the flight, where total water measures high, presumably as the walls outgas during ascent. Furthermore, the aircraft ascended through fairly thick cirrus, as indicated both visually and by the total water measurement. If a small fraction of cloud water sticks to instrument surfaces, especially upstream of the heater, or prior to the heater being turned on, this water could later outgas when ambient water and pressure decrease. The second distinct feature, evident when total water measures lower than water vapor, occurs during measurements of the lowest water vapor mixing ratios, and the discrepancy appears to anti-correlate with ambient temperature, although there appears to be a lag time as well. We hypothesize that this represents water vapor sticking to the insufficiently heated inlet walls when its temperature is below ambient as the aircraft enters warmer air. The third region to focus on is in the middle of the flight where the total water instrument measurement lags the water vapor instrument measurement both as water increases and again as it decreases. The hysteresis here appears fairly benign and we emphasize can only be properly analyzed when directly compared to the water vapor instrument measurement.

The behavior exhibited here is insidious and prevalent in *in situ* instruments that measure molecules that adhere to surfaces, not only water vapor. Furthermore, by comparing the "agreement" illustrated in Figure 3-1 with the "disagreement" illustrated in Figure 3-2 using the exact same data, we make the point that scatter plots can obfuscate rather than illustrate the actual agreement or disagreement in data sets. It is also necessary to stress that making accurate water vapor measurements in clear air is a necessary but not sufficient condition for validating the accuracy of the total water measurement in clouds. The degree to which the instrument exhibits hysteresis directly impacts its accuracy. To further illustrate this point we focus on a section of the 20020716 flight during CRYSTAL FACE, where the WB-57 traverses the same thick cirrus cloud three times, with measurements of total water reaching more than 2500 ppmv in the cloud, and with background water vapor about 30 to 35 ppmv.

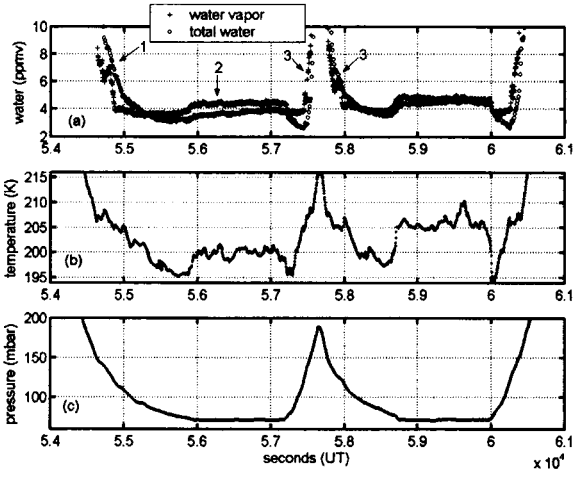

Figure 3-2. Panel (a) shows under close inspection the small systematic differences between the water vapor and total water instruments during the May 21, 2001 flight as described in the text. The numbered arrows indicate the different regions of hysteresis described in the text. Panels (b) and (c) show plots of temperature and pressure vs. time during the flight.

In Figure 3-3a we show water, total water, and the ice water content derived from the Cloud, Aerosol, and Particle Spectrometer (CAPS) [Baumgardner *et al.*, 2002] as the WB-57 traverses the cloud, and in Figure 3-3b we focus in on the water values at the edges and outside

of the clouds. Using the CAPS data to delineate the cloud edges, we indicate with arrows times after cloud traversals where water vapor measured by the total water instrument is clearly high. This extreme case illustrates the limited but observable impact of the walls even in this region where the ice water content of the cloud is up to 100 times the background water vapor.

On the other hand, if we focus on the beginning of the flights, during ascent, we see the clear effect of hysteresis that we initially attributed to ascent through thick cirrus clouds. However, a fortuitous test for the vacuum integrity of the inlet early in the Costa Rica mission resulted in a significant improvement in hysteresis and provided a representative protocol for drying out the instrument duct between flights. We illustrate this in Figure 3-4, where we compare flights on 20010807 and 20010809. The significant improvement on the 20010809 flight is attributed to the instrument pump-out between flights. The protocol, which consisted of pumping the instrument down to about 30 mbar while maintaining a slow flow of dry air or nitrogen for about an hour, was followed during the remainder of the Costa Rica mission as well as throughout the CRYSTAL mission with comparable success. This laboratory protocol minimizes, but does not totally remove hysteresis during ascent.

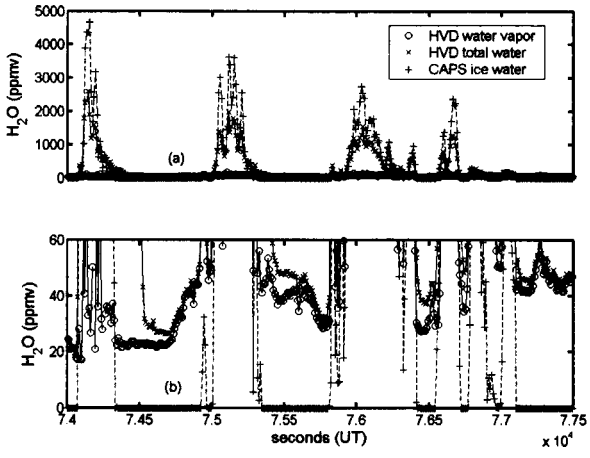

Figure 3-3. Plots of water vapor and total water made during the July 16th flight over Florida vs. time. The vertical scaling in (b) facilitates focusing on the regions of hysteresis denoted by the arrows. The CAPS ice water content measurement can be used to mark cloud edges.

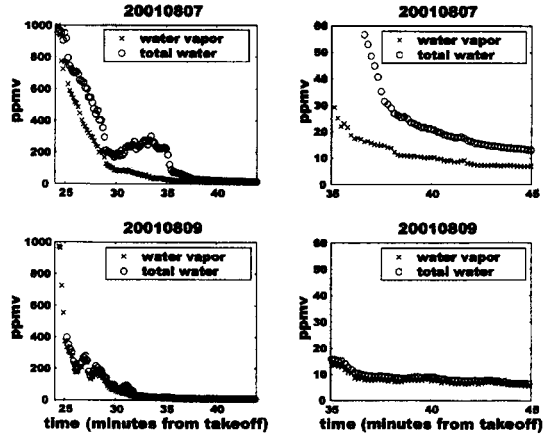

Figure 3-4. Measurements of water vapor and total water during ascent for two flights from San Jose, Costa Rica. The right-hand panels allow an intercomparison of the relative degree of hysteresis for the two flights, showing the marked improvement for the August 9th flight.

During the first test flight series in May 2001 as well as the science mission in August 2001 in San Jose, Costa Rica, the pump rpm was systematically varied from 1500 to 3000 rpm, providing flow from approximately 10% below to 25% above the isokinetic velocity in order to evaluate instrument sensitivity to flow velocity, especially in clear air. For the CRYSTAL FACE mission, with the goal of having isokinetic flow, the rpm of the pump was actively controlled, using an algorithm that calculated required mass flow from the aircraft navigational system pressure, temperature, and true air speed, and the total water instrument duct temperature, pressure, and flow velocity.

One issue that we do not address in these flights is the inlet efficiency as determined by how successful we are in maintaining isokinetic flow. That will be addressed in an upcoming paper that describes intercomparisons of

ice water content measurements made during the Midlatitude Cirrus Experiment (MidCix) that took place in May 2004.

Validation of the detection sensitivity established by laboratory calibrations: In-flight absorption measurements

Absolute accuracy to 5% is a critical performance criterion for water vapor measurements. This accuracy has been quoted for the Harvard water vapor instruments that have flown on the WB-57 and on the NASA ER-2 research aircraft. Realistically, this quoted uncertainty might have to be increased for any given data set when optical degradation from salts dissolved in cloud ice cause the instrument sensitivity to change from flight to flight. While this can be somewhat accounted for by laboratory calibrations carried out in the field, less than ideal conditions along with time constraints limit the utility of this approach and alternative approaches to tracking the relative sensitivity of the water vapor instrument in flight are being explored. Measurement of water vapor at the detection axis by in-flight absorption specifically tests or validates the absolute calibration of the detection axis at the temperature and pressure in the duct. While it is often difficult to find clear air water vapor features with number densities high enough to employ radial absorption in the water vapor instrument, clouds provide the perfect opportunity for making dual absorption/fluorescence measurements in the total water instrument. This approach, is identical to that used for in-flight validation of the Harvard water vapor instrument during the STRAT and POLARIS campaigns [Hintsa *et al.*, 1999], and accounts for any changes in lamp intensity [Kley *et al.*, 1979, Weinstock *et al.*, 1994] by simultaneously utilizing two absorption path lengths. In Figure 3-5 we highlight two typical examples of in-flight absorption measurements made during the CRYSTAL FACE campaign. Both examples show that water vapor measured by absorption is about 7% higher than that measured by fluorescence, using the laboratory calibration data.

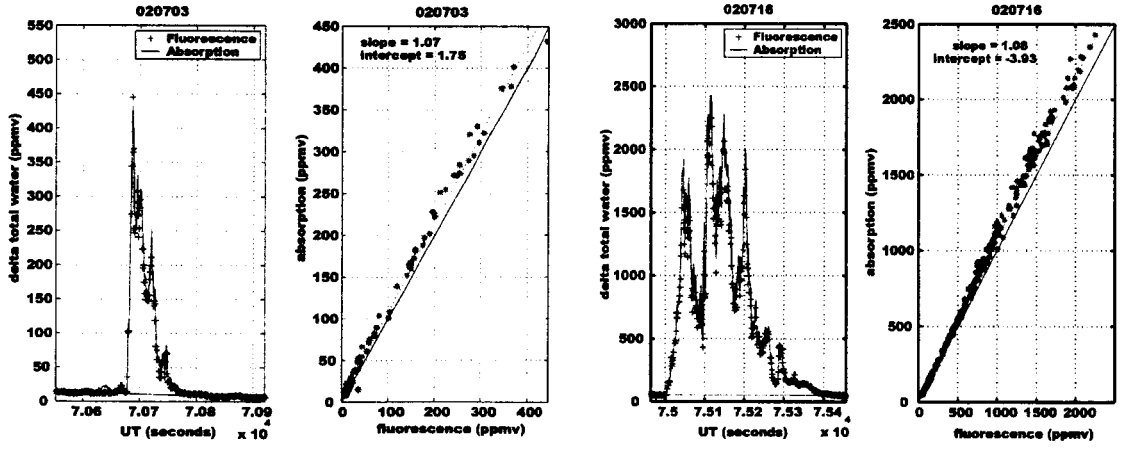

Figure 3-5. Sample in-flight intercomparisons during the July 3 and 16, 2002 flights. The left-hand panels shows the detailed agreement between total water measured by absorption and fluorescence. The right-hand panels plot water vapor measured by absorption vs. fluorescence for the same data points plotted in the left-hand panels, as well as a linear least squares fits to the data (dotted line). Also plotted are the slope=1 lines for reference

In Figure 3-6 we look at several in-flight absorption/fluorescence intercomparisons from five flights during the CRYSTAL FACE mission. These data show variability in the agreement for a given flight can ranges from 5 to 10%. This variability is not consistent with transient changes in sensitivity during the flight, but rather points to uncertainties in the realization of the in-flight absorption measurement. Furthermore, in-flight changes in instrument sensitivity are not consistent with intercomparisons with the Harvard and JPL water vapor instruments.

An apparent change in instrument sensitivity took place between the flights of July 16 and July 23. Because the field calibrations, albeit limited in number, do not exhibit this change, we attribute this to artifacts in the absorption measurement. We confirm the validity of this decision by plotting total water vs. JPL water vapor for the July 16, 23 and 26 flights (not shown). No detectable change in slope was evident in the clear-air measurements. Additionally, if you focus on the first in-flight intercomparison on July 3, results using the laboratory calibration would have to be 7% low to provide agreement between the fluorescence and absorption determinations of water. Historically however, the calibration sensitivity increases during a mission, consistent with optical degradation of the front window of the photodiode that monitors the lamp intensity. Therefore, we attribute the observed 7% difference to systematic errors in the in-flight absorption measurement.

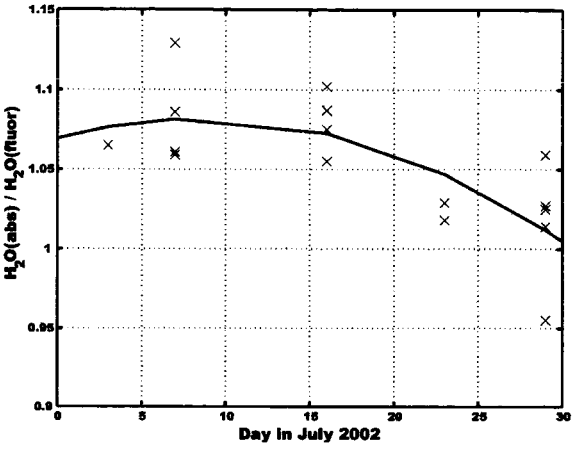

Figure 3-6. Plot of a polynomial fit to the results of all the total water in-flight absorption vs. fluorescence intercomparisons. Each point represents the slope of a least squares fit to the intercomparison data, as shown in Figure 3-5. Because of the numerous cloud encounters during CRYSTAL FACE, we were able to carry out up to 5 intercomparisons per flight.

For reference we include in Figure 3-7 an example of a similar intercomparison for the water vapor instrument. As stated earlier, there were very few opportunities for in-flight intercomparisons for the water vapor instrument, with this example providing the most stable background on either side of the absorption feature. This intercomparison is consistent with the total water intercomparisons and does not support a change from pre-flight calibrations.

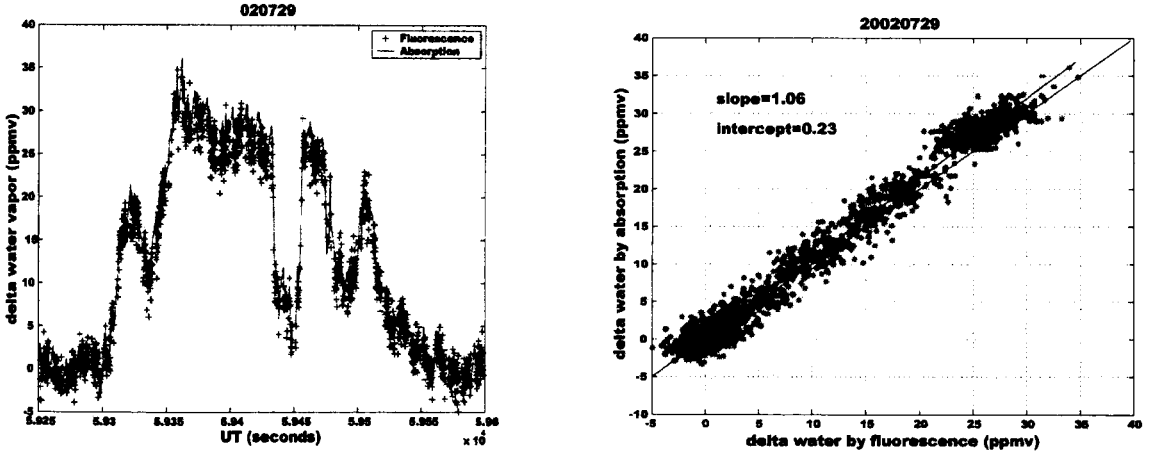

Figure 3-7. As in Figure 3-5 but for water vapor during the 20020729 flight. As with any absorption measurement, a decrease in signal is measured relative to a reference signal. For the analysis here, the water vapor mixing ratio at each edge of the absorption feature is set to zero, and it is the change in water vapor from that zero that is plotted.

Intercomparison with the JPL hygrometer

Finally, as further evidence of validation in clear air we turn to a flight during CRYSTAL FACE and present in Figures 3-8 and 3-9 simultaneous measurements from both Harvard water instruments as well as the JPL hygrometer. This particular example provides a stringent test of

the total water instrument, illustrating not only the agreement with the water vapor measurements, but also the absence of meaningful hysteresis.

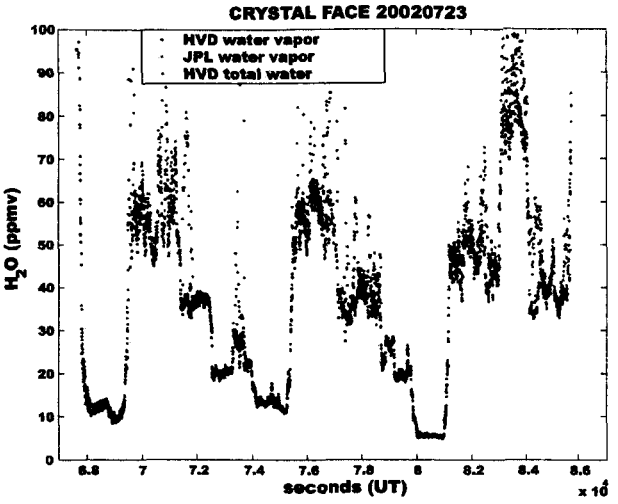

Figure 3-8. Comparison of water vapor instruments for the July 23, 2002 flight during CRYSTAL FACE showing agreement for the three instruments in clear air and the presence of clouds during positive excursions by total water.

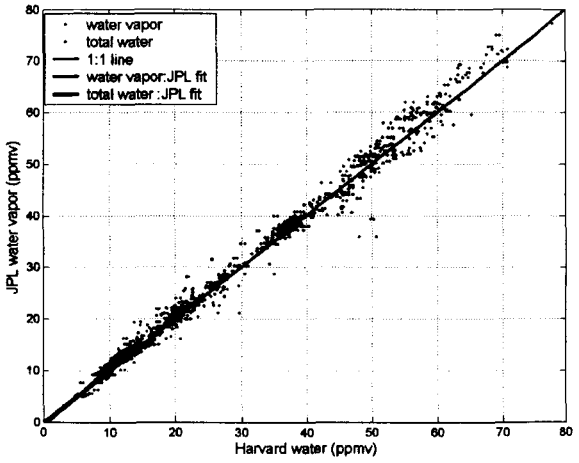

Figure 3-9. Plot of the July 23, 2002, clear air data to illustrate the linear relationship between water vapor as measured by the Harvard instruments and the JPL instrument. The blue and red lines are least squares fit to the water data less than 15 ppmv. The plot also shows agreement at low water vapor values minimizing the possibility that measurements from any of the instruments might suffer from an artificial offset in dry stratospheric air.

Particle evaporation

The instrument was designed to evaporate particles up to about 150μ in diameter. During CRYSTAL FACE, concerns were raised that the aircraft sampled particles up to almost one mm in diameter, much larger than our heater would evaporate during the transit time from the heater to the detection axis. Fortunately, the instrument detection axis fortuitously affords us an opportunity to evaluate evaporation efficiency. Both the water vapor and total water lamps emit 309 nm radiation that is detected by the fluorescence photomultiplier tube (PMT) as a result of surface, molecular, and particle scatter. Accordingly, when the WB-57 passes through a cloud, the PMTs in both the water vapor and total water instruments will show a signal that is related to ice particles that are not completely evaporated. If the particles solely undergo evaporation before reaching a detection axis, then that signal can be expressed as $S = KFd\tau$, where K is a proportionality constant, F is the photon flux from the lamp within the bandpass of the optical filter, d is the particle density, and τ is the residence time of the particle within the lamp beam. To first order, the sensitivity to particle scattering is the same for the total water and water vapor instruments allowing us to assume the same KF for both instruments. The residence time for each instrument is inversely proportional to the duct velocity, which is 5–6 m/s for the total

water instrument and about 80 m/s for the water vapor instrument. Therefore, scattering in the total water instrument should be at least ten times that in the water vapor instrument for the same particle density at the detection axis. We compare in Figure 3-10 the scattering in the water vapor and total water instruments from cloud events during the 20020729 flight. In the total water axis, where evaporation should be complete, the particle scattering signal is approximately 0.2 to 3% of that in the water vapor axis suggesting that the mole fraction of unevaporated ice particles is negligible.

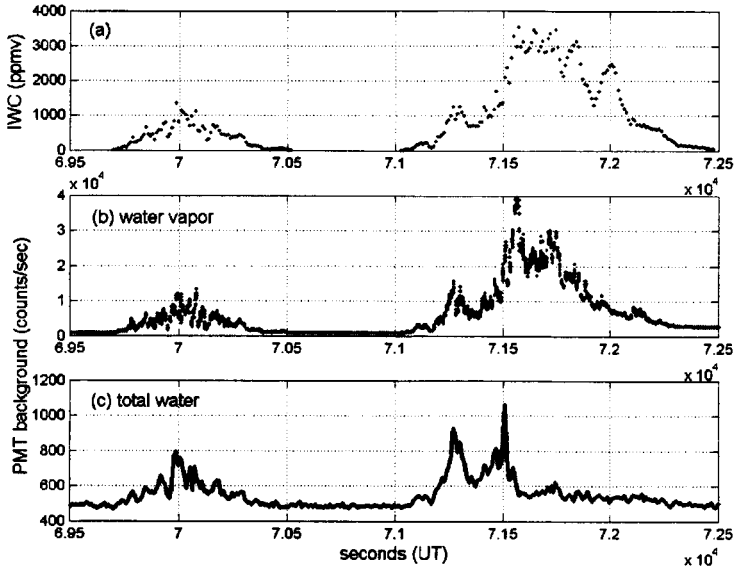

Figure 3-10. Comparison of background scatter in the water vapor and total water detection axes caused by cirrus ice particles. For water vapor, the large signal is expected because the 15-20 K ram heating and the roughly 20-millisecond residence time in the duct cause only minor particle evaporation. In the total water axis, where evaporation should be complete, the particle scattering signal is approximately 0.2 to 3% of that in the water vapor axis.

However, we must take into account the fact that particles undergo melting along with evaporation. The scattering signal from partially melted spherical particles would be less than that from pure ice particles and could explain the smaller scattering signals that are observed. The assumption that the rate of uptake of latent heat during melting of a spherical ice particle balances the rate of transfer of that heat through the surface water layer is represented by equation 16-76 of Pruppacher and Klett (1997)

$$4\pi\rho_i L_m a_i^2 \frac{\mathrm{d}a_i}{\mathrm{d}t} = \frac{4\pi a_d a_i k_w [T_0 - T_a(a_i)]}{a_d - a_i} \qquad (1)$$

where ρ_i is the density of ice, a_i is the radius of the spherical ice core of a droplet of radius a_d, L_m is the molar latent heat of melting for ice, k_w is the thermal conductivity of water, T_0 is 273 K, and T_a is the temperature of the ice core. Equation 16-77 of Pruppacher and Klett then expresses the melting time of an ice sphere

$$t_m = \frac{L_m \rho_i}{k_w a_d} \int_a^0 \frac{r(a_d - a_i)\mathrm{d}r}{T_0 - T_a(a_i)} \qquad (2)$$

From these equations we calculate that the melting time for 100–500 micron particles in the duct is on the order of a few tenths of a second. These equations somewhat underestimate the rate of melting (Rasmussen *et al.*, 1984) but are adequate for our purposes and suggest that ice particles in the total water duct undergo simultaneous evaporation and melting. During the transit time in the duct, it is likely that partially melted particles collide with the walls at the two right-angle turns. As a result of the collision, the liquid component sticks to the wall, where it evaporates, and the frozen component bounces off. It is likely that further melting continues after the last

wall collision so that the remaining ice particles have an ice core but are liquid at the surface when they reach the detection axis.

To check the implications of this assumption, we have measured the scattering signal from a stream of 70 μ droplets falling through the detection axis where they encounter a photon flux consistent with that used in flight. We compare the resulting scattering signal, equal to about 25 counts/(second-particle), with the scattering signal observed for a specific case during the 20020729 flight when ice water derived from particle measurements is significantly higher than measured by our instrument. While we find that the assumption of spherical droplets requires too high a percentage of the ice water to remain unevaporated, the droplet scattering signal measured in the laboratory suggests that the particles remaining are in fact liquid on the surface, but most likely are not spherical and remain more efficient scatterers than liquid drops. Because of the ambiguity regarding the phase of the particles remaining at the detection axis, and accordingly our inability to quantitatively relate the measured particle scattering signal to the fraction of ice water that remains unevaporated, the total water measured during CRYSTAL FACE flights for which there is a sizeable scattering signal must be viewed as a lower limit. We will describe changes to the instrument to remedy this problem later in the manuscript.

Instrument accuracy

We projected that this instrument pair could provide cloud ice water measurements with an uncertainty ranging from 10–17%, depending on particle size distributions. We now use the hysteresis observed after cloud transits on July 16, 2002, and illustrated in Figure 3-3b to estimate that at most 2% of the total water in clouds sticks to duct walls in the form of liquid droplets and then evaporates after the cloud transit. We treat this as a random error.

Typically, the precision in the measurement of water vapor and total water is about 0.5 ppmv, which limits our ability to locate the edge of clouds, especially of thin cirrus. There are also instances when the total water instrument exhibits a small amount of hysteresis. This can be especially important when water vapor is low and ambient air temperature is low and decreasing along the flight track. We hypothesize that under these conditions the inlet takes up a little water, thereby measuring low. The key concern here is not in the water vapor measurement per say, but how an inaccurate clear air measurement will degrade the accuracy of the total water measurement in a thin cirrus cloud. This manifested itself in Costa Rica, with total water measuring lower than water vapor under circumstances that coincided with a drop in ambient temperature.

We explore this further with examples from two flights during the CRYSTAL FACE mission. In Figures 3-11a and 3-11e we plot simultaneous measurements of water vapor from the two Harvard instruments and the JPL instrument. Figures 3-11b and 3-11f provide ambient temperature; Figures 3-11c and 3-11g illustrate the fractional difference between pairs of instruments. In Figures 3-11d and 3-11h the roots pump rpm is plotted. The relative drop in total water signal in both flights, corresponding to about 0.5 ppmv or 10% of the observed water vapor, coincides in each case with the change in pump rpm. The resulting slowdown in velocity apparently leads to some surface water adsorption, most likely on the cold inlet. What these plots reveal is that because of the design requirements of a total water instrument, both mechanically and operationally where isokinetic flow is needed, the risk of incurring systematic errors from surface effects must be carefully explored. While the errors shown here are small and only occur when ambient water vapor is low, this is the regime where the ice water content of thin cirrus must be measured with critical care. A 10% error in the water vapor measurement will propagate into an error in ice water content proportional to the ratio of water vapor to total water. Analysis of the full data set suggests that in the tropopause region where thin cirrus clouds are sampled the

surface only acts to adsorb and not desorb. Accordingly, without having the water vapor instrument as a check on the total water instrument, this 10% error could cause the ice water measurement in this region to be low by 10g(wv / tw)%.

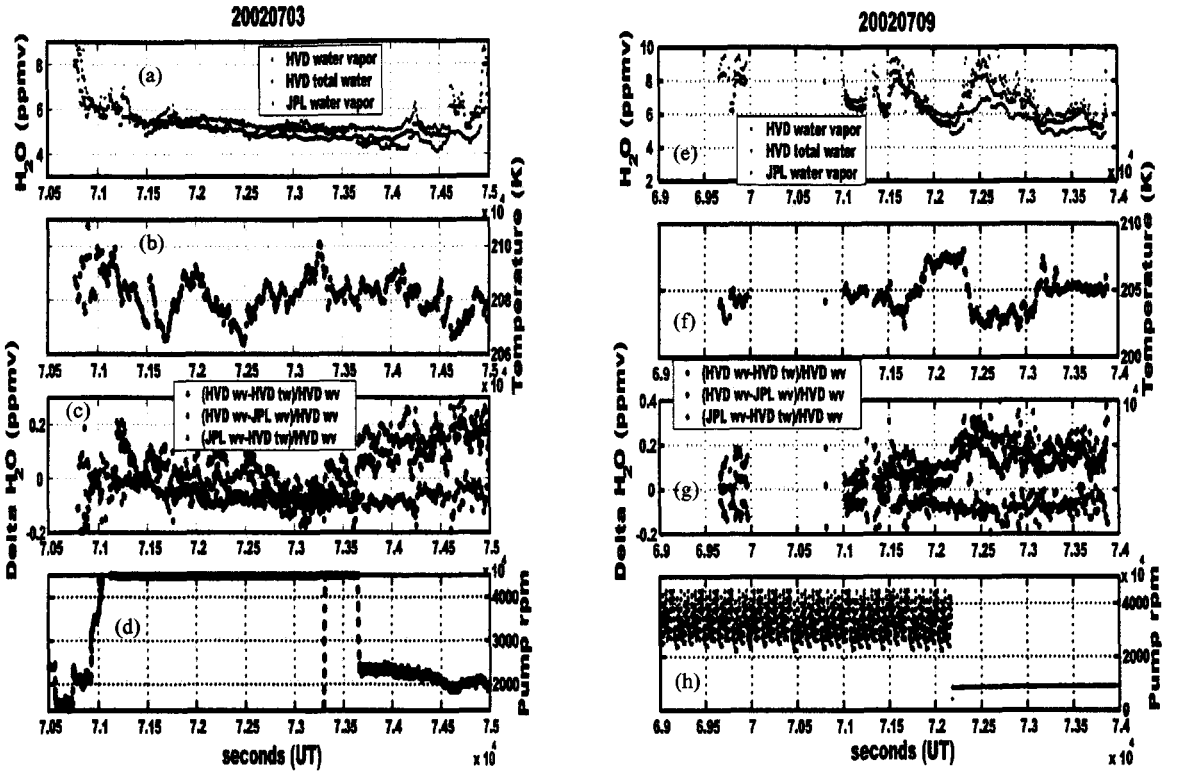

Figure 3-11. Intercomparison of total water measurements in cloud-free air with the Harvard and JPL water vapor instruments for flights on July 3, and July 9, 2002. The bottom panels plot pump rpm, showing the transition from high to low speed on the 3rd, and from high speed to off on the 9th. In each case the total water instrument measures low starting from the time that the duct velocity slows down.

In summary, a comparison of the data from the two flights shows that there is a slight dependence on pump speed/flow velocity. This manifests itself in the relatively unusual relationship between pump speed and signal, with water increasing as pump speed increases. This is unusual because there is typically a concern that outgassing of water vapor from surfaces systematically increases measured water vapor, so that when comparing water vapor measurements the lower water value is typically thought to be correct. This interpretation would imply that the instrument has a systematic error causing it to measure more accurately at slower flow speeds, behavior that is inconsistent with our broad experience base in measuring water vapor. The intercomparison with the JPL hygrometer provides evidence consistent with our interpretation of the total water instrument measuring low when a cold surface, such as the inlet, acts as a sink for water vapor.

The next source of error results from incomplete particle evaporation. Based on simple calculations for evaporation of droplets, we have established that particles with diameters up to 150 μm are completely evaporated. It is reasonable to be concerned that fractions of larger particles remain unevaporated, with that fraction proportional to the initial particle diameter. Parameterizations of effective ice particle density as a function of particle diameter [Heymsfeld *et al.*, 2004], and comparisons with total water measurements from the CAPS instrument,

suggest the possibility that Harvard ice water measurements are low when large particles are present. As discussed earlier, scattering data at the detection axis generally scales with measured total water and is consistent with incomplete evaporation. One would expect that this scattering signal would scale with the difference between Harvard and CAPS ice water content. However, there are examples during cloud events where there is significant scattering and the two total water measurements agree very well, and other cases where there is significant disagreement but only a small scattering signal. Furthermore, ice water content derived from an instrument that measures particle scattering necessitates an assumed effective ice density, and is therefore subject to a dependence on particle size. Nevertheless, the presence of a scattering signal does suggest that, at least for ice water content above about 500 ppmv, incomplete evaporation provides a source of uncertainty that is virtually impossible to quantify. We will not include this in the quoted error bars for the instrument and will address needed instrument updates later in the manuscript.

None of the in-flight validation data presented here can change the estimates of how well the instrument maintains the ambient particle concentration as air enters the instrument duct. So, as in 2005a, we estimate a 15% uncertainty for particles larger than 20μm, leading to a total uncertainty of 17% in the ice water content of thick cirrus. For thin cirrus or contrail encounters, we reduce this to 5%, thus leading to a total uncertainty of 9%.

Instrument improvements

We have provided detailed evidence for the quoted accuracy and precision of the total water vapor instrument. Additionally, we have illustrated how agreement between the total water and water vapor instruments in spite of their operational differences further support that accuracy for the water vapor instrument. Based on the information provided here, there are two specific areas that can be improved. First, measurement of ambient pressure and velocity at the inlet will significantly reduce their uncertainty that is currently based on the uncertainty in model calculations of the flow around the aircraft. Secondly, to help resolve the question of low water vapor measurements in the lower stratosphere, we plan to modify the aluminum inlet by adding sufficient heat to the front section to eliminate water adhering to the wall. and replacing the non-durable FluoroPel coating with a permanent Teflon coating. We plan to similarly coat the instrument ducting as well. Concerns regarding temperatures insufficient to totally evaporate large particles has been resolved since the CRYSTAL FACE mission by combining additional heat with a high conductance stainless steel screen with 50 μm diameter holes positioned between the two heater sections to break up large ice particles.

Conclusions

We have demonstrated the performance of a total water instrument that when combined with simultaneous water vapor measurements from the Harvard photofragment fluorescence hygrometer provides ice water mixing ratios with an accuracy of 9% in thin cirrus and 17% in thicker cirrus when particle diameters are 20 μm or larger. Examples of total water measurements in cirrus clouds ranging from subvisible cirrus in the tropics to dense cirrus in the subtropics are given. Additionally, the same series of calibrations and in-flight intercomparisons that validate the accuracy of the total water measurement in clear air help confirm the 5% accuracy of the water vapor instrument. To elaborate, the three main sources of error in the water vapor instrument arise from uncertainties in the laboratory calibration, uncertainties in the validity of the laboratory calibration in flight, and contamination of the ambient air sampled at the instrument detection axis. The overall agreement between the clear air water vapor measurements by the total water and water vapor instruments illustrates the lack of instrument contamination for the total water instrument after the exhibited hysteresis during ascent. It also

serves to further confirm the in-flight validity of the laboratory calibration for the instrument pair. The accuracy of both instruments, as for any in situ water instrument, depends on the quality of the laboratory calibration. By using the combination of added water as calculated by equation (5) and absorption at Lyman-α we minimize the potential systematic errors that might be present when solely relying on either of the two methods for determining the calibration coefficients. The 2000 SPARC water vapor assessment, and Figure 3-1 therein, illustrate that in-flight intercomparison data should not be the sole means of evaluating instrument accuracy. We show here that with the utilization of instrumental techniques that are amenable to laboratory calibration methods and successful in-flight intercomparisons, 5% instrument accuracy can in fact be validated.

Water vapor measurements by the Harvard total water instrument typically exhibit the same accuracy as the Harvard water vapor in clear air. As described previously, exceptions to this are caused by hysteresis occur during aircraft climbout when the instrument walls provide a source of water vapor and at times in the lower stratosphere when the inlet walls act as a sink of water vapor. Increased uncertainty for in-cloud measurements are derived from uncertainties in maintaining the ice particle concentration of the air sample as it transitions from ambient conditions to the instrument. While we have designed the inlet to limit the perturbation to that density, further validation of these measurements is desirable. We are in the process of making upgrades in the water vapor instrument in order to continue to improve these measurements. These will similarly improve the accuracy of the total water instrument by reducing uncertainties in the detection axis sensitivity. We also plan to make the aforementioned improvements to the total water instrument that will improve the accuracy of in-cloud measurements. Nevertheless, even if these modifications are successful, it is difficult to validate the particle efficiency of the total water inlet. For that, we look to the history of water vapor intercomparisons as a guide to what might be necessary to promote confidence in the total water measurements. With integration onto the WB-57 of the CVI cloud ice water content instrument, and the expectation that the other total water instruments will mature, opportunities for a careful intercomparison of ice water measurements will occur. The MidCiX campaign in the spring of 2004 has provided the first opportunity for such an intercomparison of IWC measurements.

References

Baumgardner, D., H. Jonsson, W. Dawson, D. O'Connor and R. Newton, The cloud, aerosol and precipitation spectrometer (CAPS): A new instrument for cloud investigations, *Atmos. Res., 59-60*, 251-264, 2002.

Heymsfeld, A. J., A. Bansemer, C. Schmitt, C. Twohy, and M. R. Poellot, Effective ice particle densities derived from aircraft data, *J. Atmos. Sci*, **61**, 982–1003, 2004.

Hintsa, E. J., E. M. Weinstock, J. G. Anderson, and R. D. May, On the accuracy of in situ water vapor measurements in the troposphere and lower stratosphere with the Harvard Lyman-α hygrometer, *J. Geophys. Res., 104*, 8183-8189,1999.

Kley, D., E. J. Stone, W. R. Henderson, J. W. Drummond, W. J. Harrop, A. L. Schmeltekopf, T. L. Thompson and R. H. Winkler, In situ measurements of the mixing ratio of water vapor in the stratosphere, *J. Atmos. Sci., 36*, 2513-2524, 1979.

Kley, D., J. M. Russell III, C. Phillips (Eds.) SPARC Assessment of Upper Tropospheric and Stratospheric Water Vapour, rep. 113, World Clim. Res. Programme (WCRP), Geneva, Switzerland, December 2000.

May, R. D., Open-path, near-infrared tunable diode laser spectrometer for atmospheric measurements of H_2O, *J. Geophys. Res. 103,* 19161-19172, 1998.

McFarquhar et al., Thin and subvisible tropopause tropical cirrus: observations and radiative impacts, *J. Atmos. Sci.*, 57, 1841-1853, 2000.

Pruppacher H. R. and J. D. Klett (1978), Microphysics of Clouds and Precipitation, Second Edition, Kluwer Academic Publishers, Norwell, MA.

Rader, D. J. and V. A. Marple, A study of the effects of anisokinetic sampling, *Aer. Sci. Tech*, **9**, 283-299, 1988.

Rasmussen, R. M., V. Levizzani and H. Pruppacher, A wind tunnel and theoretical study of the melting behaviour of atmospheric ice particles II: A theoretical study for frozen drops of radius < 500 μm, J. Atmos. Sci., 41, 374-380, 1984.

Stackhouse, P. W. Jr., and G. L. Stephens, A Theoretical and observational study of the radiative properties of cirrus: results from FIRE 1986, *J. Atmos. Sci.*, 48, 2044-2059, 1991.

Stocker, T.F., G.K.C. Clarke, H. Le Treut, R. S. Lindzen, V. P. Meleshko, R. K. Mugara, T. N. Palmer, R. T. Pierrehumbert, P. J. Sellers, K. E. Trenberth, and J. Willebrand, 2001: Physical Climate Processes and feedbacks, In: Climate Change 2001: The Scientific Basis. Contribution of Working Group I to the Third Assessment Report of the Intergovernment Panel on Climate Change [Houghton, J. T., Y. Ding, D. J. Griggs, M. Noguer, P. J. van der Linden, X. Dai, K. Maskell, and C. A. Johnson (eds)]. Cambridge University Press, Cambridge, United Kingdom and New York, NY, USA, 881pp.

Twohy, C. H., A. J. Schanot, and W. A. Cooper, *J. Atmos. Oceanic Technol.*, 14, 197-202, 1997.

Weinstock E. M., J. J. Schwab, J. B. Nee, M. J. Schwab, and J. G. Anderson, A cryogenically cooled photofragment fluorescence instrument for measuring stratospheric water vapor, Rev. Sci. Instrum., 61, 1413-1432, 1990.

Weinstock, E. M., *et al.*, "New fast response photofragment fluorescence hygrometer for use on the NASA ER-2 and the Perseus remotely piloted aircraft," *Rev. Sci. Instrum.* **65**, 3544–54, 1994.

Weinstock E. M., J. B. Smith, D. Sayres, J. R. Spackman, J. V. Pittman, N. Allen, J. Demusz, M. Greenberg, M. Rivero, L. Solomon, and J. G. Anderson, Measurements of the total water content of cirrus clouds: Instrument details and calibration, *J. Atmos. Oceanic Technol.*, submitted.

Section 4: Development of the HO_xotope instrument for the *in situ* detection of HDO, $H_2{}^{18}O$, and H_2O by Photodissociation-Laser Induced Fluorescence.

The HO_x isotope instrument (HO_xotope) was developed over the last several years to construct a fully independent measurement of water isotopes that could, in tandem with the ICOS water isotope instrument, provide validation of instrument precision, accuracy, and sampling time constants. At the same time, the development of two independent water isotope instruments enables the longer term objective of detecting both the gas phase only and the combined vapor and condensed phases (total water isotopes).

The development over the last couple of years involved several projects: (1) the laboratory exploration of the photolysis of H_2O using the newly developed excimer lamp photolysis source. (2) The development of the OD and OH spectroscopy used to detect the OH and OD fragments. (3) The calibration techniques that enable accurate addition of water and water isotopes without the fractionation associated with traditional techniques. (4) Sampling techniques that minimize wall uptake of water. (5) Calibration and diagnostics of the new instrument. (6) Mechanical, software, optical, and electrical engineering development for the cold, unpressurized WB-57 pallet. Some of the more scientifically significant developments are discussed below.

The HO_xotope instrument combines a new water photolysis system with our pre-existing instrument for laser induced fluorescence detection of OH. Water is photolyzed with an excimer lamp at 172 nm, producing ground state OH and OD radicals. The radicals are detected with rotational state selective laser induced fluorescence at 287 nm.

The fluorescence experiment has two noteworthy characteristics. The first is its high sensitivity: At stratospheric mixing ratios of H_2O (4 ppm at 50 mbar), the relative abundance of H_2O and HDO can be measured with a S/N > 12 in a 10 s acquisition cycle. The second is a fast time response: The fluorescence is collected a 1 cm^3 region in the center of a well defined flow. This minimizes the detection of isotopes from the boundary layer of the duct where wall exchange, uptake, and desorption occur. This also enables the use of a small sampling volume (<500 cm^3), since long path lengths are not required. The Harvard HOx isotope instrument provides a benchmark measurement that is uncontaminated by wall effects, a feature that is critically important in evaluating measurements of a polar molecule such as water vapor.

The Fluorescence Detection of H_2O and HDO in the lower stratosphere

Step 1: Photodissociation of $H_2O + h\nu \rightarrow H + OH$ and $HDO + h\nu \rightarrow H + OD$ $h\nu = 172$ nm

- High power Xe excimer lamp
  - 8 W @ 172 nm
  - 30 kHz pulses
  - 5 μs width

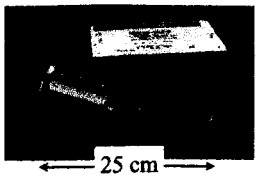

- Microdischarges evolve to fill entire lamp envelope.

The lamp emission has good overlap with the H_2O absorption band that peaks at 165 nm. The photolysis efficiency is limited by oxygen absorption below 170 nm.

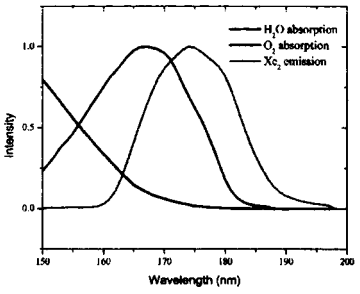

Step 2: Laser induced fluorescence detection of OH and OD at 287 nm

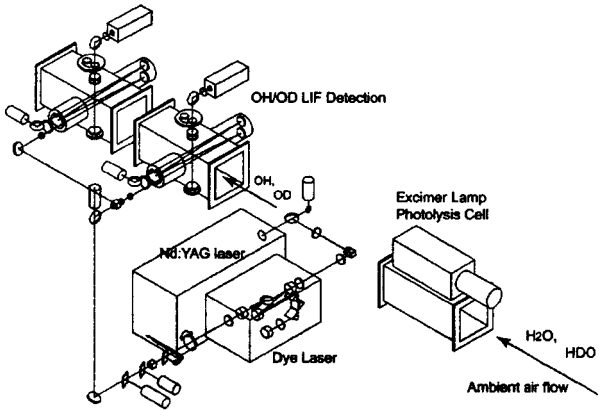

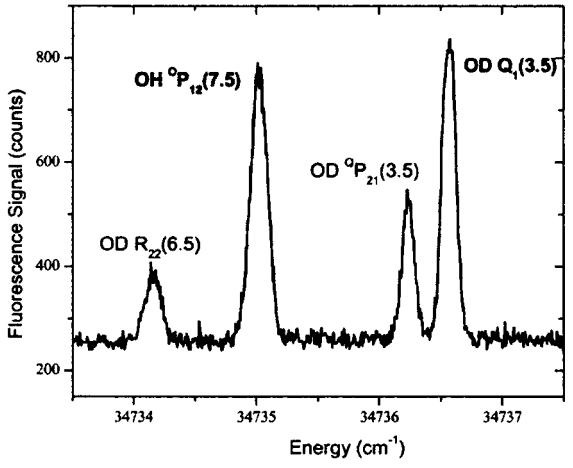

Figure 4-1. The OH and OD fragments are detected by laser induced fluorescence at 287 nm (34735 cm^{-1}) with a laser system that has flown on the NASA ER-2 since 1992. The flow is maintained at 15–30 mbar by an 8 l/s mechanical pump. The ducting system (not shown) is coated with Teflon or similar fluoropolymer to minimize water uptake. The flow is straightened to minimize wall reactions of the radicals. OH and OD are detected alternately by tuning to a weak OH line or a strong OD line.

Calibration

The absolute calibration of the water isotopes defines the intrinsic accuracy of the water isotope instruments in the absence of systematic errors. For example, this calibration includes pressure and temperature dependent factors, but does not include sampling time constants. The calibration of the isotope instruments uses the well-established water vapor addition system used by the Harvard Lyman-α instruments and a new technique developed for fast flow isotope detection. The water vapor addition system provides a known amount of water vapor using the known vapor pressure of water at a given temperature. This calibration method has been used in the laboratory intercomparison between the Harvard Lyman–α instruments and the JPL water hygrometer operated by Bob Herman.

The liquid water injection system provides a new mechanism for adding a known amount of water into a flow system without the fractionation of water isotopes that occurs during evaporation. Samples of standard mean ocean water are added directly into the flow system as water droplets, each 200 picoliters in volume. The droplets evaporate *in situ*, ensuring that the isotopic character of the sample is maintained in the calibration flow system. The water injection technique itself is calibrated by measuring the volume and weight of a known number of drops

(e.g. 10^6 drops = 0.200 ml = 0.200 mg → 200 pl/drop). The method is thus independent of vapor pressure relationship with temperature. By using both methods, the Harvard water isotope instruments are tied to the same absolute standard mean ocean water isotopic abundance provided by NIST and the water vapor pressure relationships used by *in situ* water vapor instruments.

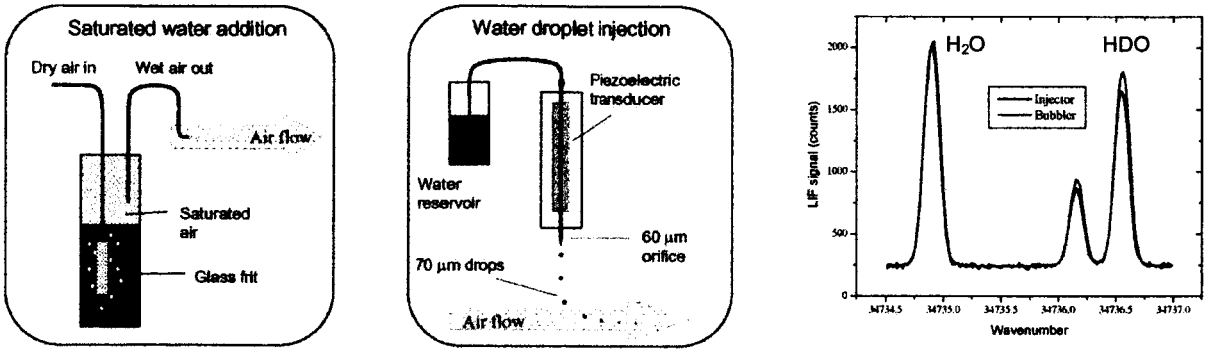

Figure 4-2. The two absolute water addition systems are shown above. The saturated water addition system uses the vapor pressure relation with temperature to determine the absolute partial pressure of water vapor added into the flow. The water droplet injector uses a piezoelectric actuated capillary to inject a known amount of liquid water into the flow. The addition of liquid water avoids the fractionation that results from evaporative sources. The observed spectrum shown on the right illustrates the advantage of direct water injection. The abundance of HDO is 7% greater with liquid injection due to the absence of isotope fractionation.

Sampling

The primary consideration in sampling water *in situ* is the uptake and subsequent release of water from the walls of the instrument. This consideration is even more significant when the exchange includes the isotopes that change on a time scale very different than the abundance of water alone. As a result, the magnitude of this wall exchange limits both the time response and the accuracy of these water isotope instruments.

The sampling time constants of the ICOS and HOx isotopes instruments are minimized through careful design that minimizes dead volumes in the flow, liberal use of hydrophobic coatings, and fast well-developed flows. These time constants, which factor into the overall accuracy and time response are then determined empirically. For example, the time constant of the HOx isotope instrument is shown in Figure 4-3. After the addition of 100 ppm of H_2O into the system, the concentration at some time t after the turnoff is given by

$$[H_2O]_{measured} = 100 \text{ ppm } [(0.98\exp(-t/\tau_1) + 0.015\exp(-t/\tau_2) + 0.005\exp(-t/\tau_3)]$$

where τ corresponds to various time constants including flush time, adsorption onto walls, and absorption into o-rings. With this time response, the instrument measures a residual 1% (+1 ppmv) after 10 s and 0.3% (+0.3 ppmv) after 60 s.

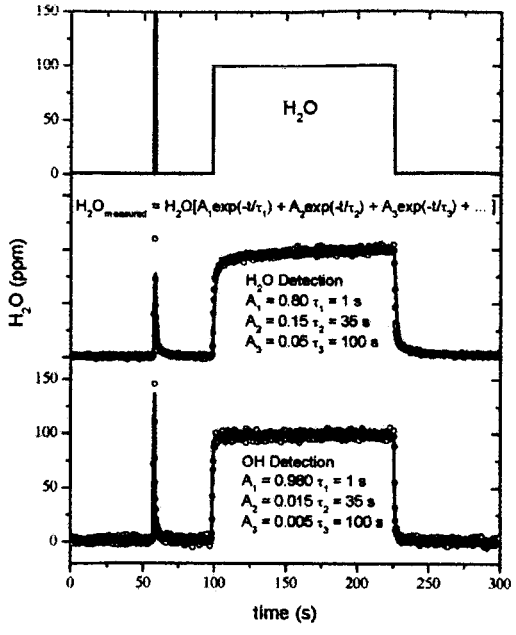

Figure 4-3. The time response of (a) molecular H_2O detection and (b) OH fragment detection are measured simultaneously. A known amount of H_2O is injected into the instrument (top). The 4 Hz signal of H_2O detected with a Lyman– α hygrometer is shown in the middle panel. The 4 Hz LIF signal of the OH fragment produced from photolysis of H_2O at 172 nm is shown in the lower panel.
The solid lines are generated from a multi-exponential fit:

$A_1\exp(-t/\tau_1) + A_2\exp(-t/\tau_2) + A_3\exp(-t/\tau_3) + \ldots$

$A_1 = 0.98$ $\tau_1 = 1$ s (flush time)
$A_2 = 0.015$ $\tau_2 = 35$ s (wall effects)
$A_3 = 0.005$ $\tau_3 = 100$ s (wall effects)

In this model τ_1 corresponds to the pumping time constant, or the flush time of the system. τ_2 and τ_3 correspond to the adsorptive and absorptive uptake of the system.
The larger time constant for the molecular detection of H_2O results from wall interactions that are absent in the OH fragment detection.

The effect of these measured time constants on the accuracy of an *in situ* water isotope measurement can be evaluated with a simple model. Consider an aircraft profile that flies from a recently convected airmass with boundary layer like isotopic character into a dry cloud free region with a stratospheric isotopic character. The water might change from 100 ppm to 15 ppm, but HDO will change from 14 ppb to 0.75 ppb. The relative change in HDO is roughly 3 times greater than the change in H_2O, resulting in a 3× greater sensitivity to sampling time constants or desorption from walls. This example is shown graphically in Figure 4-4, for a hypothetical flight profile.

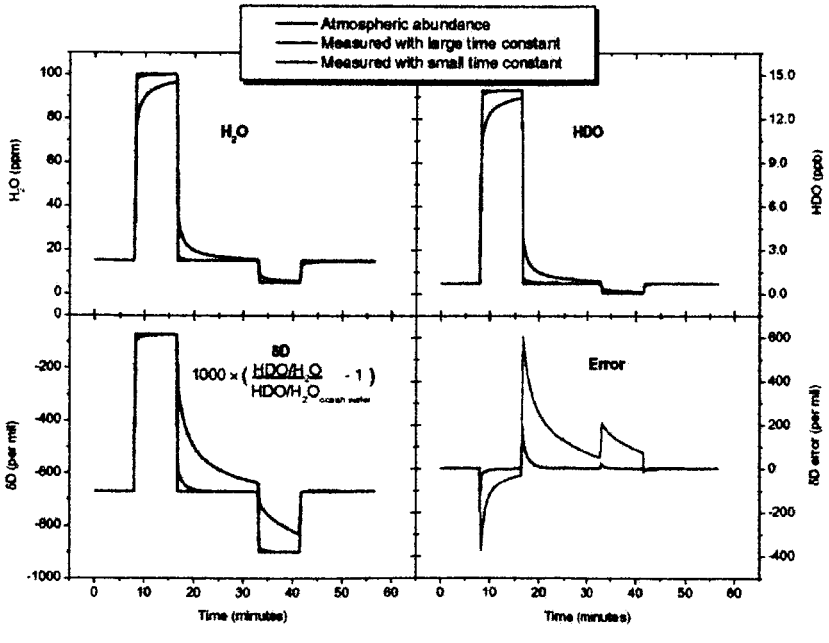

Figure 4-4. The effect of sampling time constants are shown for a hypothetical flight profile. The aircraft passes through dry and wet regions representative of the well mixed stratosphere or upper troposphere, a recently convected airmass, and a highly desiccated advected airmass. The two sampling time constants from Figure 4-3 are applied to the hypothetical water isotopic abundance. The depletion of HDO is represented by dD, where $\delta D = 0$ per mil is equal to standard mean ocean water and $\delta D = -1000$ per mil indicates the complete removal of HDO.

In this example the accuracy of the hypothetical measurement with the longer time constant is unacceptable. The error in the isotope ratio is as large as 400 per mil (40%) for

several minutes after leaving the wet airmass. This is a particularly significant error because the transition regions between wet and dry regions mimic the convective outflow regions that are likely to contain some of the most important scientific data for water isotope instruments. The data with the fast time constant provides acceptable errors in the isotope ratio, even in the sharp transitions. Given this measured time constant, an evaluation of the CRYSTAL-FACE data set indicates that the sampling time constant of the HOx isotopes instrument would contribute less than 0.3% (3 per mil) rms error. The analysis of the instrument sampling time constant in the laboratory provides the added benefit of clearly identifying data that might be suspect due to sampling time constants shown in Figure 4-4.

***In situ* Instrument Performance**

The HO_xotope instrument was flown on NASA's WB-57 aircraft in Houston, Texas during Dececember 2004/January 2005. The payload consisted of the two new water isotope instruments, HO_xotope (measuring H_2O and HDO) and ICOS (H_2O, HDO, and $H_2{}^{18}O$), each equipped with rear facing inlets that sampled gas phase water. Also on the payload were two well established instruments measuring water vapor and total water (vapor + condensate) using the Lyman-α photofragment fluorescence technique. During the test flights the WB-57 cruised at altitudes from the mid-troposphere to the overworld stratosphere (~9 to 19 km altitude) and sampled several abrupt changes in water vapor mixing ratio in both clear and cloudy air. Measurements were then evaluated for consistency, precision, accuracy, and sampling time constants.

The engineering test flight series were quite successful from both an engineering and science perspective. Several key engineering tasks were addressed after the first test flight exposed issues with several subsystems, including the laser diode and vacuum pump. Other new subsystems performed well throughout the flight series, including the inlet and sampling system, the photolysis system and the data acquisition and control systems. Due to the priority of engineering tasks, the instrument was not calibrated prior to the field deployment. Post flight calibrations identified several diagnostics that were not adequately measured during the test flights, including the flow velocity in the sampling system, the transmission of the photolysis cell windows, and the LIF detection efficiency. Each of these inadequately measured diagnostics contributes an error of 10 – 30% to the overall detection sensitivity of the HO_xotope instrument that cannot be recovered by post flight calibration. Each of these issues has since been addressed with engineering changes and operational changes. However, the data presented below are adjusted by a single multiplicative factor to account for the difference in sensitivity of the instrument during the flight and during post flight calibrations.

The comparison of the HO_xotope measurements of H_2O to that measured by the Lyman-α water vapor instrument provides a useful validation of the new isotope instrument. The Lyman-α instrument is an excellent validation instrument, having demonstrated absolute accuracy of 5% in numerous flight campaigns and having in flight calibrations to ensure this accuracy on a flight-to-flight basis. The comparison for the flight of January 11, 2005 is shown in Figure 4-5. Though not shown, the comparison with the Harvard total water instrument provides an additional cross check on water vapor in clear air and quantifies water in the condensed phase, so that inlet performance can be evaluated. In Figure 4-5 the H_2O vapor measured by the Hoxotope instrument is multiplied by an arbitrary scaling factor (~1.3). Thus, we cannot evaluate the absolute accuracy of the HO_xotope measurements for these data. The relative accuracy, however, is very good, except during the ascent and shows excellent consistency between the two measurements.

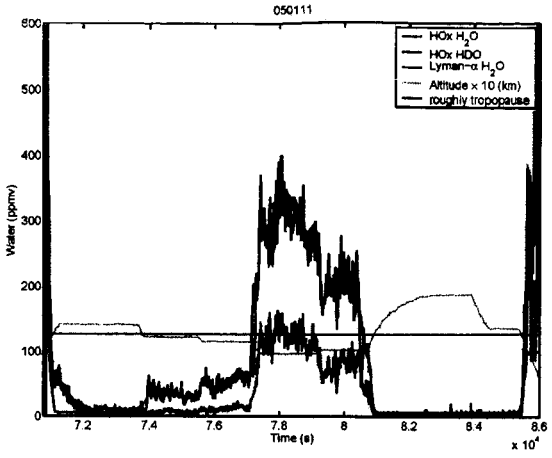

Figure 4-5. Observations of the H_2O and HDO measured by the Hoxotope instrument are compared to the H_2O observed by the Harvard Lyman-α hygrometer. The Hoxotope data is scaled by a constant. The data were obtained between Houston, TX, and Pensacola, FL on January 11, 2005. The altitude of the WB-57 and the approximate altitude of the tropopause are shown for reference.

The ascent portion of the flight shows a large overabundance of H_2O and HDO in the HO_xotope measurement. The total water instrument (not shown) does not indicate the presence of any clouds, thus it is not due to the sampling of condensed water through the HO_xotope inlet. The offset is large enough that it is unlikely to come from within the instrument. The integrated difference in water between the HO_xotope and Lyman-α instruments is equivalent to 6 cm^3 of pure H_2O, or 1000 monolayers coverage on the instrument inlet. The most likely source of water is the inlet of the Harvard total water instrument that sits in front of the HO_xotope inlet on the fuselage of the WB-57. The large surface area of the total water inlet could shed water during ascent and not be a significant source or sink of water during the flight. Future flights will require a repositioning of the HO_xotope inlet to the starboard side of the aircraft or of the instrument pallet to a position forward of the total water inlet.

After the ascent, the discrepancy quickly disappears and does not reappear again. The absence of discrepancies after ascent confirms the absence of large unexplained instrument artifacts and underscores the absence of water uptake and release in the HO_xotope system. Though not shown, the total water instrument indicates numerous cloud encounters that do not appear in the HO_xotope data. A one hour long stratospheric leg of this flight is shown in Figure 4-6. The data obtained in this flight leg demonstrates both the fast time response of HO_xotope and the high sensitivity to HDO in the lower stratosphere. The fast time response and the absence of water uptake and release in the instrument are evident at edges of the figure. At these points during the flight, altitude changes lead to abrupt changes in water vapor (between 250 and 10 ppm in less than 10 minutes). The measurement of HDO shows a precision of 0.3 ppbv in a 4 s average in this flight leg. Post flight changes to the instrument should improve the sensitivity by a factor of 3.

The measurement of the isotope ratio is the primary scientific objective during these test flights. The ratio of HO_xotope HDO and Lyman-α H_2O is shown in Figure 4-7 for the flight of January 11, 2005. The use of Lyman-α H_2O instead of the HO_xotope value reduces the scatter in the plot. The contaminated data obtained during the ascent is highlighted in red. The isotopically heavy contamination shifts all of the measured values towards less depleted values. The data represent the entire flight, at numerous level flight legs between Houston and Pensacola, rather than a profile at one location. The local tropopause was not measured continuously during the flight, but temperature profiles indicate the tropopause was at roughly 11–12 km during ascent and descent above Houston, and during tropopause crossings at the far eastern part of the flight.

The isotope ratio shown in Figure 4-7 is derived from the HO_xotope measurement of HDO that was scaled to match the Lyman-α data. Although this scaling diminishes the independence of the HDO/H_2O ratio in an absolute sense, the relative value of HDO to H_2O is completely independent. In other words, the shape of the profile is largely unchanged is a different scaling factor is used to scale the HO_xotope data to match the Lyman-α data. The absolute uncertainty is equal to the scaling factor (~30% or 300 per mil), but the relative accuracy is much better, ~10% or 100 per mil.

Postflight improvements have focused on improving the accuracy and precision of the measurement. These improvements include enhancing the reliability of the flight diagnostics that determine the instrument sensitivity during flight that were largely responsible for the need for a scaling factor in the data shown above. The implementation of new photolysis cell windows and detection axis filters will improve the sensitivity of the instrument, possibly by as much as a factor of 3. Laboratory calibrations that account for these changes are ongoing.

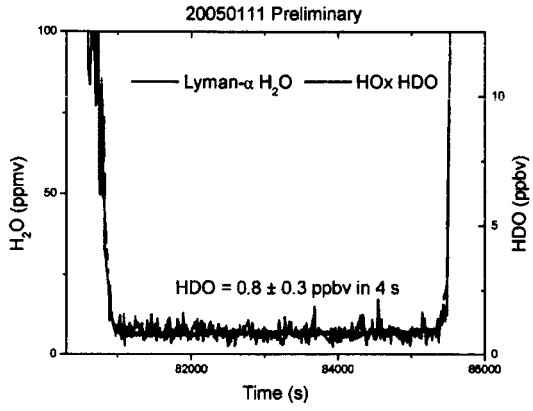

Figure 4-6. Observations of HDO by the Hoxotope instrument are compared to the H_2O measured by Harvard Lyman-α instrument. The WB-57 in this case ascends rapidly from a 10 km flight leg in the upper troposphere with [H_2O] > 250 ppmv to a 19 km leg in the lower stratosphere with [H_2O] < 10 ppmv. This portion of the flight is approximately 1 hour in duration.

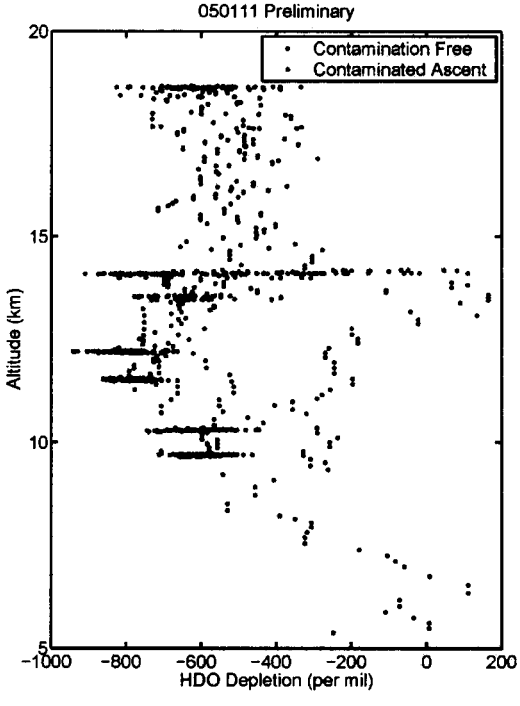

Figure 4-7. The Isotope ratio in units of HDO depletion (per mil) = 1000 × (HDO/H_2O − 1) determined from the ratio of Hoxotope HDO and Lyman-α H_2O is shown *versus* altitude. The contaminated ascent data is highlighted in red. The contamination due to isotopically heavy boundary layer water shifts the measured isotope ratio to less depleted values. The tropopause is roughly 11-12 km.

Section 5: Development and Deployment of the Integrated Cavity Output Spectroscopy (ICOS) Technique for the *in situ* Detection of HDO and H_2O.

The year 2004 brought to a close a three-year project developing a new spectroscopic technique for *in situ* detection of rare atmospheric gases, funded by NASA's Instrument Incubator Program. This development effort was motivated by the scientific goal of measuring the isotopic composition of water vapor (the ratio HDO/H2O) in the near-tropopause region, where the mixing ratio of HDO is less than a part per billion. Because conventional spectroscopic techniques do not provide sufficient sensitivity to measure small changes in the isotopic ratio in this region, there is a need for new, more sensitive measurement techniques. The Harvard IIP work focused on the technique of Integrated Cavity Output Spectroscopy (ICOS). During the first two years of the IIP project, a bench instrument was constructed and the ICOS technique refined until its sensitivity reached the target for HDO science. In 2004, the laboratory bench instrument was converted into a fully autonomous flight instrument, integrated onto NASA's WB-57 aircraft, and flown in a series of test flights. These test flights demonstrated that laboratory ICOS performance could be reproduced in flight, with sensitivity levels exceeding those of most comparable spectroscopic instruments by more than an order of magnitude. The flights represented the first use of ICOS for *in situ* aircraft-borne atmospheric measurements. We review here the principles of ICOS, describe the instrument construction and attendant issues, and show data from the 2004/2005 test flights.

Integrated Cavity Output Spectrocopy (ICOS)

ICOS is an optical-cavity based absorption spectroscopy technique (Engeln *et al.* 1998; Paul *et al.,* 2001). As in the conventional absorption spectroscopy techniques used in many aircraft instruments, light from a narrowband, tunable, continuous-wave laser is injected into a cell containing a gas sample and tuned across a spectral feature of the molecule of interest (Figure 5-1).

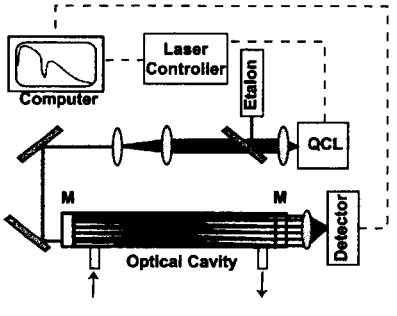

Figure 5-1. ICOS schematic. Light from a mid-infrared cw quantum cascade laser is coupled into an optical cavity; output light is captured by an HgCdTe detector.

Light exiting the sample cell is captured on a detector; the resulting spectral signature gives the concentration of the absorbing molecules. For measuring scarce molecules, conventional spectroscopic instruments typically use multipass cells that enhance absorption by increasing the optical pathlength through the gas sample. The upper limit for pathlength in these systems is on the order of 100 meters, i.e., approximately a hundred passes in a one-meter cell. ICOS overcomes this limitation by the use of a high-finesse optical cavity composed of highly-reflective mirrors rather than a multipass Herriot or White cell. With cavity mirrors of R = 99.98% (200 ppm losses), photons entering the cell are trapped for nearly 5000 passes on average, producing an effective optical pathlength of nearly 4 km. For this reason the ICOS technique offered the promise of a 40 x improvement in sensitivity over conventional techniques. By winter 2003 our laboratory efforts had realized this promise, producing mid-IR spectra with noise comparable to that of conventional techniques but 40 x deep absorption features (Figure 5-2). This performance allows the scientifically useful measurement of HDO/H2O ratios in the dry stratosphere.

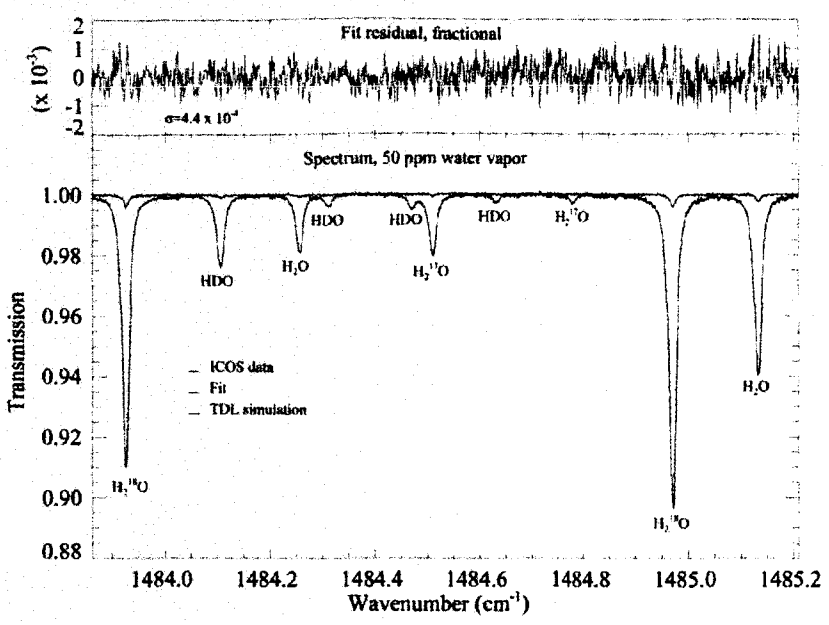

Figure 5-2. Laboratory ICOS spectrum of the target region for detection of HDO and H2O, in blue, with the fit to the data overlaid in red. For comparison a synthetic representation of the signal from a conventional absorption instrument is shown in black. The increased absorption and corresponding sensitivity of the ICOS technique is readily apparent.

Design of the flight system

During 2004, the laboratory ICOS system was converted to a flight instrument for use on the WB-57, the Harvard ICOS Isotope Instrument. The conversion presented numerous challenges:

- *Optical cell and foreoptics*
  - The cell must be mechanically stable enough to maintain alignment even in hostile flight conditions
  - Cell flush rate must be less than 3 seconds to not compromise spatial resolution of data
- *Gas handling system*
  - All inlet plumbing must be free of hysteresis: no trapped volumes, minimal surface adsorption
- *Thermal enclosure*
  - Temperature around optical system must be maintained to within several degrees.
  - Gradients across optical cell must be less than half a degree, because several of the absorption lines in the target spectrum are highly temperature-sensitive.
- *Calibration and fitting*
  - During flight, periodic calibration cycles must provide water-free baseline data to provide a power curve for fitting data.
  - Because flying a reliable water vapor standard is extremely difficult, calibration cycles require a calibration proxy.
  - Laser frequency and tuning characteristics must remain stable enough for reliable fits.
- *Electronics*
  - Operation of all systems must be fully autonomous and reliable.

— Electrical noise must not compromise sensitivity.

Much of the work effort during 2004 was devoted to meeting these challenges. Some aspects of this work are described below.

Optical cell

Design of the optical cell required multiple considerations. The optical cell must provide a stable and noise-minimal optical alignment. It must also provide flow characteristics that minimize contamination. For robustness in flight, the optical cell was designed with no moveable parts or adjustment. Mirror position is determined only by the machining of the surfaces on which the mirrors rest, and all adjustments to optical alignment are provided by moveable mirrors in the foreoptics. This approach has not previously been attempted in laboratory cavity-based spectroscopy, where vibrations are readily controlled and external pressure changes are insignificant. We have found however that it works extremely well and provides a simple, reliable means of aligning the optical system in a flight system.

Because maximizing the free aperture of the mirror is vitally important to minimizing the "noise" of spurious cavity resonances, the cell is sealed with a radial o-ring around the mirror diameter rather than a standard face-seal on the mirror surface. This configuration allows us to make use of the full surface area of the mirror to spread out the beam pattern and minimize interferences between successive beam passes.

Optical cell design must minimize two potential avenues for contamination within the optical cell: 1) desorption of adsorbed water molecules from walls and surfaces, and 2) trapping of air and water from previous periods of the flight in stagnant air pockets in the cell. Surface adsorption was addressed by coating all surfaces exposed to measured gas with a Fluoropel, a hydrophobic fluoropolymer. Prevention of stagnant airspace required a larger design effort. Gas is injected into both ends of the cell, near the mirrors, through four offset inlet ports at each end (Figure 5-3). The offset ports provide a swirling flow that scours out the volume in front of each mirror and prevents development of a pocket of stagnant air (Figure 5-4).

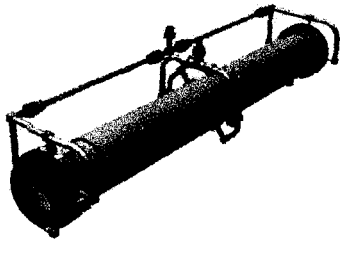

Figure 5-3. Optical cell and gas handling plumbing for the Harvard ICOS instrument. Gas is injected from four ports around either mirror and exits from ports at cell center. Multiple exit ports are needed for symmetrical flow.

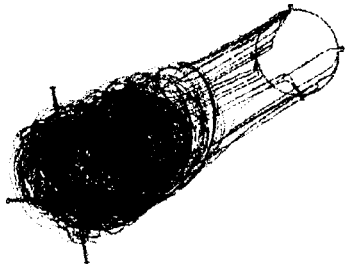

Figure 5-4. Fluid-dynamics simulation of flow in one half of the ICOS optical cell. Color along each fluid parcel trajectory denotes time since injection. The offset injection ports produce a swirling flow that scours out the airspace in front of each mirror.

Gas handling system:

The same contamination considerations for the optical cell apply to the tubing used to carry air to the optical cell: surface adsorption and dead volumes must be minimized. In the ICOS instrument, all gas-handling tubing is orbitally-welded, electropolished 1/2" diameter

stainless steel tubing coated with Fluoropel. All connections on the input gas handling system are made with pharmaceutical-grade fittings (Swagelok VCO-B) that eliminate dead volumes.

Thermal regulation

Temperature stability within the instrument was accomplished by enclosing the entire optical and calibration gas systems within an insulated and heated box, with 750 W of heat provided by thermofoil heaters mounted on the inner metal surface. Input air is thermally regulated by 75W of thermofoil heaters on the input tubing before the entrance into the thermal enclosure. This system was tested in the laboratory and proven to be adequate for heating input gas from the coldest ambient temperatures experienced (190 K) to the regulated enclosure temperature (298 K). Temperature within the optical cell is monitored by two high-precision thermistors (0.1 K, 1 MOhm to prevent self-heating) mounted at cell center, at the waist of the beam pattern where they do not interfere with optical transmission. Temperature is also monitored along the cell via five matched high-precision thermistors mounted to the cell surface. Because tests in the laboratory show that the gas temperature gradient within the cell is a well-defined function of the temperature gradient along the cell surface, this allows monitoring and evaluation of any thermal inhomogeneities in the gas sample.

Calibration and fitting

During periodic calibration cycles during the flight, the cell is flushed with ultradry air to allow measurement of a water-free baseline power curve for the laser. For this purpose we use research-grade nitrogen gas (Matheson) with water vapor mixing ratio guaranteed below 0.2 ppm, i.e., less than 5% of the minimum water vapor measured during flight. This residual water does not mean that the measurement is subject to 5% error: if the laser tuning characteristics remain stable, any residual baseline water can be corrected in the final data reduction by simple addition to the derived mixing ratio. Laser tuning characteristics are monitored continuously during the flight by splitting a small fraction of the laser power into a Ge etalon, which provides a measurement of laser frequency.

Calibration cycles also include several minutes of measurement of an in-flight calibration standard that serves as a proxy for water vapor. We have identified methyl fluoride (CH3F) as the best proxy, as it provides a series of strong and well-separated absorption lines over the instrument's target spectral region. As a non-polar molecule, CH_3F presents no danger of adsorption onto wall surfaces and contamination of subsequent measurements.

Test flights

The first test flights of the ICOS Isotope Instrument were made on the WB-57 out of Ellington Field in Houston, TX, on a campaign from Nov. 2004–Jan. 2005. The goal of these flights was to obtain an understanding of instrument performance, to demonstrate that laboratory sensitivity is maintained in flight, and to validate the instrument measurements. The need for validation mandated that the aircraft payload contain numerous instruments providing simultaneous measurements for comparison. For this reason the instrument payload included four independent measurement of H_2O and two of HDO. The total payload of the test flight series is described in Table 5-1 and shown in Figure 5-5.

Table 5-1.

Instrument	Gases	Phase	Integration time
ICOS	H_2O, HDO, $H_2{}^{18}O$, $H_2{}^{17}O$, CH_4	gas phase	3 s
Hoxotope	H_2O, HDO	gas phase	12 s
Lyman-α Water Vapor	H_2O	gas phase	3 s
Lyman-α Total Water	H_2O	combined gas phase + condensate	3 s

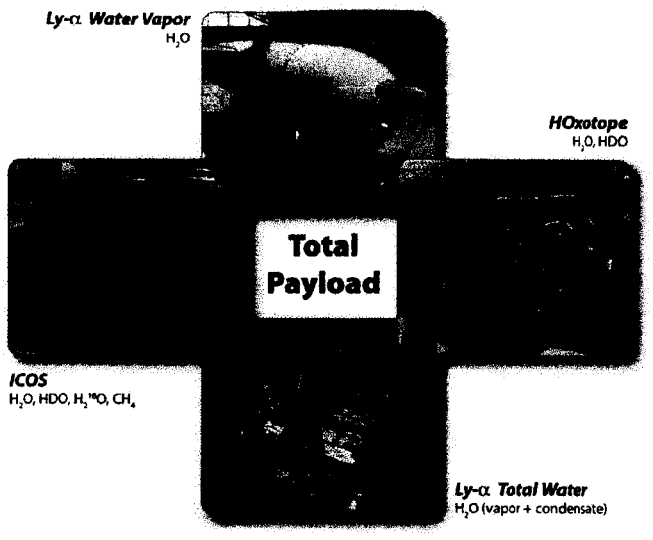

Figure 5-5. The total payload for the Harvard isotope test flights of November 2004–January 2005.

The two Lyman-α instruments are long-established, well-characterized and well-calibrated instruments that have participated in numerous NASA science missions. The HO_xotope instrument is based on an established instrument (Harvard HOx) that is now modified for measurement of H_2O and HDO. Clouds and cirrus can be identified by comparing the Lyman-α total water and water vapor instruments; this allows evaluation of any contamination of new instruments by evaporation of cloud ice particles. All instruments have a rapid data rate, allowing validation of their intrinsic response time, a critical concern when measuring the rapid fluctuations in water vapor concentrations expected in the near-tropopause region.

In order to test the instruments most fully, flight plans were designed to probe the instruments' dynamic range, response time, sensitivity, and robustness to contamination. The WB-57 flew flight legs at a variety of altitudes from mid-troposphere to stratosphere, with water vapor mixing ratios varying from many hundred ppm to less than 5 ppm. During some sections of the flights, pilots were instructed to maintain level altitude in cloud-free air to provide relatively constant mixing ratios and the clearest possible comparison of the different instruments' retrievals; this allows identification of any systematic errors. At other times, pilots made transects through cloud tops and near-tropopause cirrus wherever possible to test the instruments' imperviousness to evaporation of cloud particles. Sharp cloud boundaries also provided a test of the instruments' intrinsic response times. Ascents and descents provided a test of the instruments' performance under conditions of differing external pressure.

Results

All subsystems of the ICOS instrument performed well during the test flight series. The electronics proved relatively trouble-free, with no additional sources of noise during flight. Temperature and pressure were well controlled. Temperatures in the optical system were regulated to a few degrees K during the entirety of the flight, and temperature gradients along the optical cell were less than the identified 0.5K limit. Pressure within the cell was regulated to less than 0.3 torr for the bulk of the flight. Cell pressure was allowed to vary at the highest flight altitudes (i.e., lowest ambient pressure, < 60 torr) but even in this case data proved relatively easy to fit and measurement accuracy was not compromised. This stability produced instrument sensitivity at near-laboratory values, giving measurement precision for HDO of 60 ppt even in the dry stratosphere, sufficient for addressing all identified science issues involving HDO/H_2O in the near-tropopause region.

Hysteresis and contamination due to variations in atmospheric water were also shown to be minimal during the test flights. Figure 5-6 shows water vapor measurements from all four instruments during the flight of Jan. 11, 2005; all four instruments track the same atmospheric features, with no identifiable lags. Figure 5-7 narrows in one portion of the flight, in which the airplane flew a level flight leg at 9 km through heavy cirrus and then ascended into the dry stratosphere. Water vapor concentrations change abruptly from several hundred ppm (with total water > 500 ppm) to stratospheric values of 5 ppm. The ICOS measurement shows no detectable contamination or lag during this transition. These results demonstrate that the instrument is capable of making uncontaminated measurements even during quite wide swings in ambient atmospheric water concentrations.

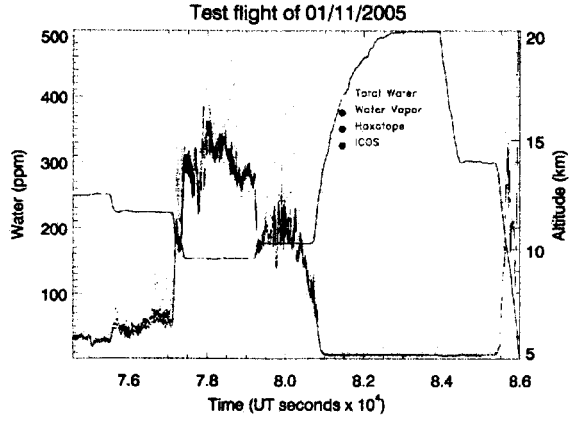

Figure 5-6. Water vapor measurements by four independent instruments during the test flight of Jan. 11, 2005. The total water instrument is shown in light blue; this trace exceeds the others during crossings through clouds or cirrus. All instruments reproduce the same features over a large dynamic range. Note that ICOS precision for measurement of water vapor already exceeds that of the Ly-a instruments.

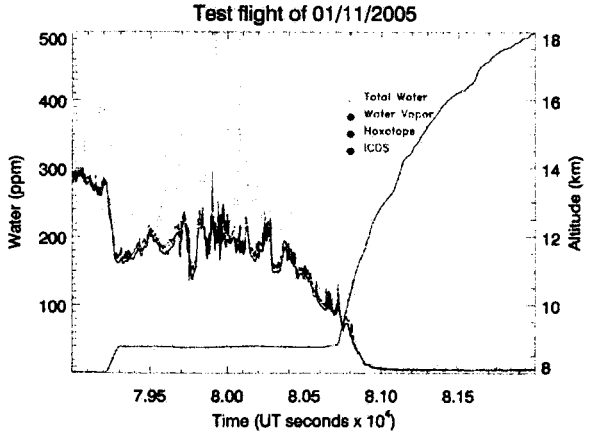

Figure 5-7. A subsection of the Jan. 11 flight, in which the aircraft climbs abruptly from 9 km, within the troposphere, into the dry overworld stratosphere. Neither of the isotope instruments shows residual contamination from the recent transect through cirrus containing over 500 ppm total water.

Identified improvements

Several instrument subsystems could not be fully completed to design specification by the time of the flight series. Work on these is ongoing during Spring 2005, and all are expected to be complete by the next flights of the instrument. As expected, the lack of these subsystems compromised data quality somewhat in certain parts of the test flights, and completing them will further improve ICOS data quality.

Inlet and outlet valves

The ICOS instrument design calls for a gas system that can be fully sealed during the pre-flight hands-off period, so that it experiences no contact with wet Houston air. The outlet valve was not installed during the test flight series, so that the instrument could not be sealed from ambient air while on the ground. This resulted in some residual contamination that persisted

throughout most of the flight and caused systematic measurement error in certain flight segments, as described further below.

Dewar pressure regulation

The ICOS laser wavelength is a direct function of laser temperature, and therefore a direct function of the gas pressure in the liquid nitrogen Dewar that holds the laser. At the time of the test flight series we had not yet completed our new, ultrastable pressure regulation system, and the instrument flew with an older system that remained somewhat sensitive to ambient pressure. The laser wavelength therefore shifted slightly at the highest flight altitudes, meaning that residual contamination from ground exposure became apparent in one flight segment. This is apparent in the ICOS profile of isotopic contamination from the Jan. 11 flight, where the 18 km flight leg shows erroneously enriched isotopic compositions (Figure 5-8). During the remainder of the flight, isotopic profiles appear reasonable and in good agreement with the (slightly noisier) HO_xotope profile. The offset between the instruments is not a concern; these are preliminary data and neither of the instruments had been fully calibrated at this time. Without laboratory calibration, HO_xotope measurements are uncertain by 30% (300 per mil). Note that the scatter in the data below the tropopause is not measurement noise, but simply reflects varying water concentrations even on a level flight leg. When data are plotted against water vapor instead of altitude, the resulting relationship is extremely compact (Figure 5-9). This result differs from previous measurements and interpretations of tropospheric water isotopic composition (Webster *et al.*, 2001).

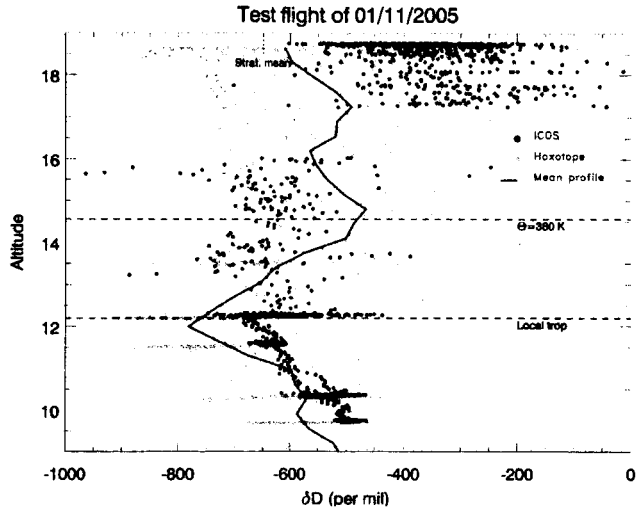

Figure 5-8. Profiles of isotopic composition obtained during the Jan. 11 flight, with HO_xotope data in green and ICOS data in black. These are preliminary data only. The anomalously enriched stratospheric measurements by ICOS at the highest stratospheric altitudes result from the combination of residual contamination in the optical cell and altitude-dependent changes in the laser tuning curve. An approximate average profile is shown in red. This profile is consistent with expectations for the midlatitudes air: isotopic composition decreases steadily from surface to tropopause; is relatively constant in the overworld stratosphere and is consistent with known mean stratospheric values (-650 per mil); and in the middleworld, a region of frequent mixing, varies along a mixing line between tropospheric and overworld stratospheric values.

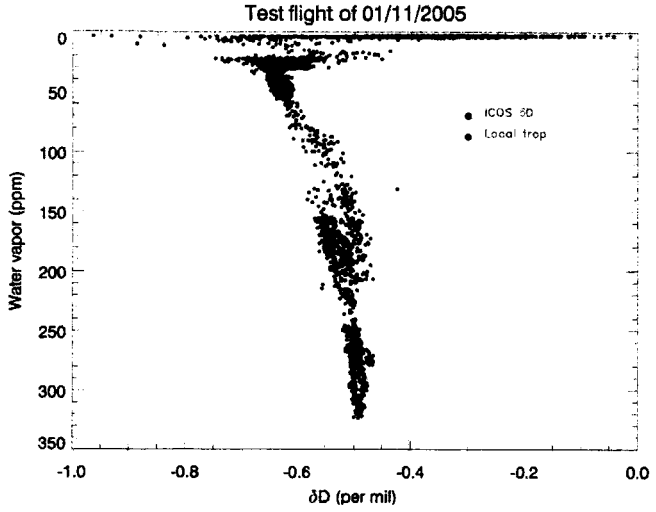

Figure 5-9. ICOS profile of isotopic composition plotted against water vapor. The two follow a very compact relationship in the troposphere. Near-tropopause data, by contrast, shown in red, shows real atmospheric variation from convective processes. The slight offset of one part of the profile is an artifact of these preliminary fits, caused by the use of a different in-flight calibration power curve during this flight segment.

Spectroscopic calibration

As mentioned above, the ICOS spectroscopic parameters had not been independently calibrated in the laboratory at the time of the test flights. Data retrievals shown above are based on HITRAN parameters alone. This calibration is ongoing.

Foreoptics purge

The thermal enclosure is designed to be purged with dry nitrogen before flight and continuously dried during flight, so that the foreoptics do not hold wet Houston air that can impact the measurement. Although the ICOS instrument is 5000 times more sensitive to water vapor within the sample cell than to water vapor outside it, the extreme moisture content of surface air can still produce a noticeable effect in ICOS spectra if wet air is carried to high altitudes. At the time of test flights, the purge and desiccation system had not been implemented; this led to some systematic error in the early portions of the test flights.

Conclusions

During 2004, we proved the effectiveness of the ICOS technique and made the first demonstration of its usefulness for *in situ* gas measurement from an aircraft. We completed, integrated, and test-flew a new instrument that can serve as a valuable addition to NASA research payloads for years to come. We provided new measurements of HDO and H2O that show interesting and previously unobserved physical phenomena. The instrument promises to provide a valuable science contribution to NASA research missions, especially with regard to planned missions to the tropics, where ICOS HDO measurements can be used to explore questions of troposphere-stratosphere exchange and the origin of stratospheric water vapor.

References

Engeln, R., G. Berden, R. Peeters and G. Meijer, "Cavity enhanced absorption and cavity enhanced magnetic rotation spectroscopy," *Rev. Sci. Instr.* **69**, 3763–9, 1998.

Paul, J. B., L. Lapson and J. G. Anderson, "Ultrasensitive absorption spectroscopy with a high-finesse optical cavity and off-axis alignment," *Applied Optics* **40** (27): 4904–10 SEP 20 2001

Webster, C. R., and A. J. Heymsfield, "Water isotope ratios D/H, O-18/O-16, O-17/O-16 in and out of clouds map dehydration pathways," *Science* **302** (5651): 1742–5 DEC 5 2003.

Section 6: Measurement Within the Arctic Vortex and Interpretation of those Measurements of the Dimer ClOOCl Observed Simultaneously with ClO.

Abstract. The first measurements of ClOOCl in the stratosphere have been acquired from a NASA ER-2 aircraft, deployed from Kiruna, Sweden (68° N, 21° E), during the joint SOLVE/THESEO-2000 mission of the winter of 1999/2000. ClOOCl is detected by thermal dissociation into two ClO fragments that are measured by the well-known technique of chemical conversion, vacuum ultraviolet resonance fluroescence. Ambient ClO is detected simultaneously. Observations of the ratio $[ClOOCl]/[ClO]^2$ (estimated uncertainty of ±25%, 1σ) are used with a time-dependent photochemical model, to test the model representation of the ratios of kinetic parameters J/k^{Prod} and k^{Loss}/k^{Prod} for day and nighttime observations, respectively. Here, k^{Prod} and k^{Loss} are the rate constants for ClOOCl production and loss, respectively, and J is the photolysis rate of ClOOCl. The observations are in good agreement with J based upon the 2002 JPL recommended cross sections for ClOOCl [Sander *et al.*, 2002], if the true value of k^{Prod} is given by either the 2000 JPL recommendation [Sander *et al.*, 2000] or the work of Trolier *et al.* [1990]. The larger values of k^{Prod} given by *Bloss et al.* [2001] and the 2002 JPL recommendation are consistent with the observations only if J is increased by a significant amount. This is accomplished if J is calculated with the larger ClOOCl cross sections measured by Burkholder *et al.* [1990]. The J values for ClOOCl based on the Huder and DeMore [1995] cross sections are too small, by factors of ~1.6 to 2.5 for all values of k^{Prod}, based on the observations. Nighttime results suggest that, for 190<T<200 K, the values for K^{Eq} (the equilibrium constant, equal to the ratio of k^{Prod}/k^{Loss}) of *Cox and Hayman* [1988] and Avallone and Toohey [2001] are in best agreement with the observations.

Introduction

The existence of the weakly bound dimer of chlorine monoxide, ClOOCl, is fundamental to the most destructive chlorine-catalyzed ozone loss mechanism in the polar stratosphere [Molina and Molina, 1987; Anderson *et al.*, 1991; Solomon, 1999; World Meteorological Organization, 2002, and references therein]. Yet, ClOOCl has never before been observed in the stratosphere by *in situ* or remote means. Thus a large body of work aimed at elucidating our understanding of chlorine-catalyzed ozone loss has relied upon its assumed existence in the winter polar vortices in the Arctic and Antarctic. In the absence of measurements, the density of ClOOCl in the stratosphere has been estimated based on laboratory measurements of the fundamental photochemical processes thought to control ClOOCl production and loss. Clearly, a measurement of the dimer constitutes a critical check of the photochemistry of ClOOCl and thus free radical forms of chlorine, ClO_x (≈ ClO + ClOOCl × 2) in the stratosphere.

The basis for our interest in ClOOCl, and more broadly the ratio of ClO_x over Cl_y ($Cl_y \approx ClO_x$ + HCl + $ClONO_2$ + HOCl), concerns the continuing need to critically appraise our understanding of the halogen-catalyzed ozone loss cycles. In particular, the dimer mechanism allows rapid ozone destruction through the photolysis of ClOOCl to atomic chlorine [Molina and Molina, 1987] and becomes extremely efficient at high ClO concentrations typical of polar regions in late winter and early spring,

$$\begin{aligned} &ClO + ClO + M \xrightarrow{k^{Prod}} ClOOCl + M \\ &ClOOCl \xrightarrow{J} Cl + ClOO^* \\ &ClOO^* \longrightarrow Cl + O_2 \\ &\underline{\left(Cl + O_3 \rightarrow ClO + O_2\right) \times 2} \\ &\text{net: } 2\,O_3 \rightarrow 3\,O_2 \end{aligned} \qquad (1)$$

The rate-determining step of this catalytic cycle is the photolysis reaction, thus the ozone loss rate via the dimer cycle is

$$\left(\frac{d[O_3]}{dt}\right)_{ClOOCl} = -2 \times J_{ClOOCl}\, \Phi_{Cl}\, [ClOOCl] \qquad (2)$$

where Φ_{Cl} is the quantum yield into the chlorine atom-producing channel [Molina *et al.*, 1990; Moore *et al.*, 1999].

A more thorough understanding of the rate-limiting reactions of all catalytic cycles that control ozone loss and the processes that control radical concentrations is required to increase confidence in our ability to forecast future UV exposure at Earth's surface. The urgency is identified by (a) the observed, seasonally-dependent erosion of the total ozone column at mid-latitudes in recent decades [Logan *et al.*, 1999], (b) the dramatic year-to-year variation in late winter column ozone at high northerly latitudes [Newman *et al.*, 1997] that is tied to the extreme temperature sensitivity [Chipperfield and Jones, 1999; Salawitch, 1998] of chlorine [Molina and Molina, 1987] and bromine [McElroy *et al.*, 1986] catalyzed ozone loss, and (c) the realization that ozone loss is likely linked to trends in the abundance of water vapor in the lower stratosphere and the associated lower temperatures resulting from enhanced radiative cooling [Kirk-Davidoff *et al.*, 1999].

Our present forecasting ability is sobered by the recent recognition that photochemical models tend to underestimate the observed rate of chemical ozone depletion in the Arctic stratosphere [Becker *et al.*, 2000; Rex *et al.*, 2003]. Accurate forecasts of future levels of Arctic ozone are further complicated by the suggestion that the build-up of greenhouse gases might result in changes in wintertime stratospheric circulation patterns that lead to lower temperatures and enhance ozone depletion [Shindell *et al.*, 1998].

Here we present the first measurements of ClOOCl in the stratosphere. These data, when combined with simultaneous measurements of ClO, allow the most direct observation-based examination of polar halogen photochemistry to date. These measurements were carried out as part of the joint Sage III Ozone Loss and Validation Experiment (SOLVE) and the Third European Stratospheric Experiment on Ozone (THESEO) 2000 campaign staged out of Kiruna, Sweden (68°N, 21°E) from Nov 1999 to Mar 2000 [Newman *et al.*, 2002].

ClOOCl Photochemistry and Modeling

Two of the three known reactions directly involved with production and loss of ClOOCl are part of the catalytic cycle (1) shown above. The single known production mechanism for ClOOCl is the self-reaction of ClO radicals [Sander *et al.*, 1989; Trolier *et al.*, 1990; Nickolaisen *et al.*, 1994; Bloss *et al.*, 2001],

$$ClO + ClO + M \xrightarrow{k^{Prod}} ClOOCl + M \qquad (3)$$

where k^{Prod} is the reaction rate constant and M represents the oxygen/nitrogen mixture of the bulk atmosphere. The peroxide structure of the ClO dimer has been shown to be the dominant product formed under stratospherically relevant conditions, and its detailed molecular structure and energy have been determined [McGrath *et al.*, 1988; Birk *et al.*, 1989; McGrath *et al.*, 1990].

ClOOCl is lost by at least two known mechanisms, photolysis and thermal dissociation. Photolysis predominates over thermal dissociation of ClOOCl during the day at typical temperatures of the wintertime Arctic lower stratosphere polar vortex,

$$ClOOCl \xrightarrow{J} Cl + ClOO \quad (\text{yield} \geq 0.9) \qquad (4a)$$

$$\xrightarrow{J} ClO + ClO \quad (\text{yield} \leq 0.1) \qquad (4b)$$

where J (s^{-1}) is the photolysis rate. J values are calculated using a radiative transfer model described below coupled with laboratory measurements of absorption cross sections [Molina and Molina, 1987; Cox and Hayman, 1988; Permien *et al.*, 1988; Burkholder *et al.*, 1990; DeMore and Tschuikow-Roux, 1990; Huder and DeMore, 1995].

Due to experimental difficulty, there are considerable uncertainties in the value of the ClOOCl absorption cross section (σClOOCl) for the region longward of 310 nm. The cross sections reported by Huder and Demore [1995] for this spectral region, shown in Figure 6-1, are considerably smaller than other measurements. Also shown are cross sections reported by Burkholder *et al.* [1990], which are larger than other measurements, particularly for wavelengths (λ) > 310 nm. The JPL 2002 recommendation (JPL02) [Sander *et al.*, 2002] (which has remained unchanged since the 1994 evaluation) lies between these two laboratory determinations. The measurement of σClOOCl reported by DeMore and Tschuikow-Roux [1990] (not shown) lies close to the JPL02 recommendation for $\lambda < 360$ nm, and falls between JPL02 and Huder and DeMore [1995] for $360 < \lambda < 400$ nm. For $\lambda > 360$ nm, the JPL02 recommendation is a log-linear extrapolation of data obtained at shorter wavelengths, which is "considered to be more reliable than the experimental measurements because of the very small dimer cross sections in this region" [Sander *et al.*, 2002].

The cross sections reported by Burkholder *et al.* [1990] extend to 410 nm. We have carried out our own log-linear extrapolation of these data to 450 nm, shown by the dotted line in Figure 6-1, for calculations of the photolysis rate of ClOOCl based on Burkholder *et al.* [1990] discussed below. This extrapolation is somewhat uncertain due to the noise in the data. We have chosen, we believe, a reasonable extrapolation that represents the overall slope of the data between 300 and 410 nm and that also has a slope similar to the JPL 2002 extrapolation at these wavelengths.

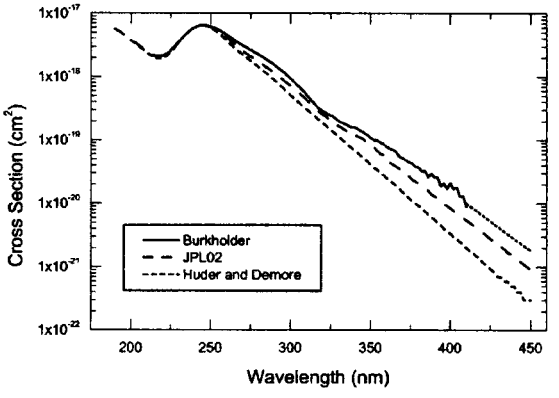

Figure 6-1. ClOOCl absorption cross section (cm^2) versus wavelength (nm) from *Burkholder et al.* [1990], JPL02 [*Sander et al.*, 2002], and *Huder and DeMore* [1995]. The dotted line at $\lambda > 410$ nm for *Burkholder et al.* [1990] is an extrapolation, calculated according to $\log[\sigma(cm^2)] = -0.0185 \times \lambda\,(nm) - 12.415$.

It is important to stress two points regarding the cross sections of Huder and DeMore [1995]: their experiment was designed to minimize contributions of possible spectral impurities from species such as Cl_2O, Cl_2, and O_3 that may have affected other experiments; their values for σ_{ClOOCl} reported longward of 310 nm are based on a log-linear extrapolation of measurements at shorter wavelengths. Consequently, the Huder and DeMore [1995] values of σ_{ClOOCl} longward of 310 nm might appear low when, in fact, it may be the direct measurements obtained by other experiments at longer wavelengths that are biased high due to impurities. Alternatively, the Huder and DeMore [1995] long wavelength extrapolation could be in error due to modest errors in the slope of the cross section shortward of 310 nm.

There could also be a low-lying electronic state that leads to dissociation of ClOOCl that is only active longward of 310 nm and is correctly accounted for in the Burkholder *et al.* [1990] experiment. A coupled-cluster calculation using a double zeta quality basis set has indicated the presence of a triplet state of ClOOCl near 350 to 370 nm [J. S. Francisco, private communication, 2003].

There is considerable uncertainty in σ_{ClOOCl} based on the laboratory studies, "particularly for longer wavelengths" as is stated by the JPL Data Evaluation Panel [Sander *et al.*, 2002]. Finally, we note that the determination of the quantum yield into channels 4a and 4b [Molina *et al.*, 1990; Moore *et al.*, 1999] is crucially important to the efficiency of the dimer-based catalytic cycle (1), since (4b) constitutes a null cycle. To date, direct measurements of this quantum yield for wavelengths longward of 308 nm are lacking.

In the analysis shown below, we include model results using J values derived from cross sections of ClOOCl from four sources: Huder and DeMore [1995] (J^{Huder}); the JPL02 recommendation [Sander *et al.*, 2002] (J^{JPL02}); Burkholder *et al.* [1990], extrapolated to 450 nm as shown in Figure 6-1 ($J^{Burkholder}$); and a speculative J value based upon an assumption of additional photolysis in the near IR tail of the absorption curve (J^{NearIR}). Calculations of these four J values of ClOOCl at 50 mbar, for a surface albedo of 0.24 and a local temperature of 195 K, are shown in Figure 6-2a. J^{Huder} is about 40 to 50% lower than J^{JPL02}, whereas $J^{Burkholder}$ is about 40 to 50% higher than J^{JPL02} (Figure 6-2b). J^{NearIR} becomes much larger than J^{JPL02} for SZA > ~88° (see below). Finally, the contribution to $J^{Burkholder}$ of the log-linear extrapolation of σ_{ClOOCl} is quantified in Figure 6-2c; the increase in J varies from about 5% (SZA < 80°) to about 20% (91° < SZA < 93°).

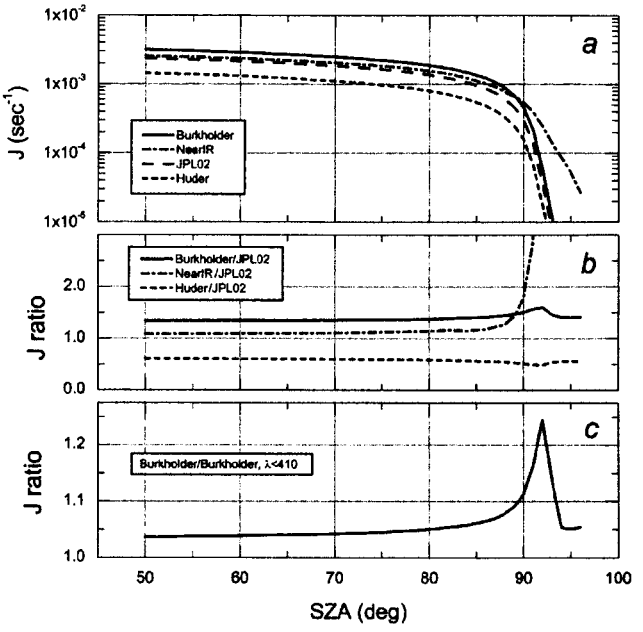

Figure 6-2. (a) The J value (sec^{-1}) for ClOOCl photolysis versus SZA (deg) for four cases used here: $J^{Burkholder}$, J^{NearIR}, J^{JPL02}, and J^{Huder}. (b) The ratios of $J^{Burkholder}$, J^{NearIR}, and J^{Huder} with respect to J^{JPL02}. (c) The ratio of $J^{Burkholder}$ (cross section extrapolated to 450 nm) with respect to the J value based upon the non-extrapolated *Burkholder et al.* [1990] cross section. All J values were calculated for 50 mbar, local temperature of 195 K, surface albedo of 0.24, cloud-free conditions, using profiles for temperature and ozone appropriate for the Arctic vortex during early March 2000.

The speculative J^{NearIR} arose from an analysis of observations of ClO in the Arctic vortex by MLS (Microwave Limb Sounder) that, at times, suggested ClOOCl photolysis might occur rapidly out to solar zenith angles as high as 92° [J. Waters, M. Santee, and M. Rex, private communication, 2003]. Based solely on energetics, ClOOCl could dissociate in the near IR, although no state has been identified, or even suggested [e.g., Burkholder *et al.*, 1990]. However, the scientific importance of near IR photolysis of ClOOCl (e.g., $\lambda > 800$ nm) is that, were it to occur at an appreciable rate, chemical loss of ozone for air that received solar illumination at zenith angles between about 85 and 92° would be increased significantly relative to standard models [Burkholder *et al.*, 1990; Rex *et al.*, 2003]. This sensitivity arises because, at twilight, the atmosphere is optically thin in the near IR (in the absence of volcanically enhanced aerosol loading), whereas Rayleigh scattering leads to significant increases in optical depth at shorter wavelengths [Wennberg *et al.*, 1999]. Hence the J^{ClOOCl} would remain large in twilight if there happened to be a contribution to photolysis from the near IR, Figure 6-2a. J^{NearIR} is calculated assuming the JPL02 cross section plus an additional state with an integrated cross section × actinic flux of 2×10^{-4} s^{-1} centered at 800 nm. This value

was determined from the previously mentioned MLS observations of ClO, which we now believe may have been biased high due to experimental noise.

The second ClOOCl loss process is by thermal dissociation, which proceeds at a rate that is a very sensitive function of temperature,

$$ClOOCl + M \xrightarrow{k^{Loss}} ClO + ClO + M \qquad (5)$$

where k^{Loss} is the reaction rate constant. For the ClOOCl observations considered here, associated with ambient temperatures in the $190 < T < 200$ K range, photolysis is approximately a factor of 10 or more larger than thermal dissociation, for SZAs equal to or less than 93 and 92°, respectively. Laboratory measurements of k^{Loss} have been carried out directly [Nickolaisen *et al.*, 1994] and k^{Loss} can be inferred from measurements of the equilibrium constant for dimer formation, K^{Eq} [Cox and Hayman, 1988], and k^{Prod}. A value of K^{Eq} has also been inferred from nighttime observations of ClO in the Arctic vortex [Avallone and Toohey, 2001].

We analyze the observations of ClOOCl and ClO with the aid of a time-dependent, 24-hour, photochemical model [Salawitch *et al.*, 1993]. Kinetic parameters used in the model are from JPL 2002 [Sander *et al.*, 2002] except as otherwise specified. The J value is calculated from the ClOOCl absorption cross sections, using a radiative transfer model [Salawitch *et al.*, 1994] constrained by maps of ozone reconstructed using measurements from the Polar Ozone Aerosol Measurement (POAM) III satellite instrument [Randall *et al.*, 2002]. Within the model, the concentrations of ClO, ClOOCl, BrO, BrCl, OClO, and O are found at 15-minute time steps by solving the appropriate set of differential equations (e.g., equations (5) and (6) of Salawitch *et al.* [1993]) subject to the conditions that production and loss of each species balance over a 24-hour period (i.e., diurnal steady state). For comparison to ER-2 observations, the model results are then linearly interpolated (versus local time) to the solar zenith angle of the data. The sum of ClO + ClOOCl × 2 (ClO_x) and the sum of Br + BrO + BrCl (BrO_x) are specified for each model run. Values of BrO_x are specified using a relation versus potential temperature based on DOAS (Differential Optical Absorption Spectroscopy) measurements of BrO in the Arctic vortex during March 2000 [K. Pfeilsticker, private communication, 2003] (model results shown here are insensitive to rather substantial variations in BrO_x). Model values for ClO_x are specified from ER-2 observations along the flight track. Using this approach, the model tests the variation of the partitioning of ClO and ClOOCl with solar illumination, temperature, and other parameters.

The model is also constrained using observed values of latitude, temperature, pressure, albedo, ozone column [e.g., McElroy, 1995], and the mixing ratio of O_3 along the flight track [e.g., *Richard et al.*, 2001]. While this approach might occasionally lead to erroneous results due to details of individual air-mass trajectories, we note the flow is primarily zonal and wind speeds are too slow to, on average, appreciably affect the results. For example, if this analysis is confined to data for which zonal and meridional wind speeds are limited to the range –10 to +10 m s^{-1}, as measured by the MMS instrument [Scott *et al.*, 1990], our conclusions remain unchanged. We have conducted extensive comparisons of model results for ClO_x and BrO_x based on this simple approach to results using a full photochemical model simulation (e.g., Salawitch *et al.*, [1994]). We find essentially no difference in the results (differences less than ~2%) when the vortex is activated, because of the near-zero levels of NO_x and the low levels of HO_x [Hanisco *et al.*, 2002] that are characteristic of the activated Arctic vortex.

The Instrument

The instrument used to detect ClO and ClOOCl was newly fabricated for the POLARIS mission, which was staged out of Fairbanks, Alaska in 1997 [Newman *et al.*, 1999]. During POLARIS the first *in situ* measurements of $ClONO_2$ were acquired [Stimpfle *et al.*, 1999]. The

design of the instrument is based upon a predecessor first deployed on the ER-2 [Brune *et al.*, 1989] during the AAOE mission, staged out of Punta Arenas, Chile in 1987 [Tuck *et al.*, 1987].

The detection of ambient ClO relies on a two-step process. ClO is first titrated with NO to form Cl atoms,

$$ClO + NO \rightarrow Cl + NO_2 \qquad (6)$$

and the Cl atom concentration is then measured quantitatively using ultraviolet (UV) resonance fluorescence at 118.9 nm [Anderson *et al.*, 1980; Brune *et al.*, 1989]. The current configuration of the instrument includes a thermal dissociation capability, whereupon weakly bound, halogen-containing molecules are cleaved into molecular fragments,

$$ClONO_2 \xrightarrow{\Delta H=113\ kJ/mol} ClO + NO_2 \qquad (7)$$

$$ClOOCl \xrightarrow{\Delta H=71\ kJ/mol} ClO + ClO \qquad (8)$$

The ClO produced by thermal dissociation of $ClONO_2$ and/or ClOOCl is then detected as above. The differing bond strengths of $ClONO_2$ and ClOOCl provide a critical diagnostic for the identification of the dissociated species as manifest by the observed temperature required for complete dissociation. Overall, the current instrument is considerably more complex than its predecessor since, in addition to the changes with the halogen detection system, an NO_2 detection subsystem was included as an integral part of the flight instrument [Perkins, 2000; Perkins *et al.*, 2001].

A schematic diagram of the flight instrument [Bonne, 1998], as it was situated in the left wing pod of the ER-2, is shown in Figure 6-3. Ambient air is sampled through the 20 cm diameter primary duct opening at the forward end of the pod as the ER-2 flies at ~200 m/s. A throttling valve near the exit of the primary duct, located at the top of the pod, is fixed to yield a flow velocity approximately one third of the aircraft velocity, ~60 m/s, in the primary duct. The laminar core of the primary flow is extracted into two parallel, mirror image, secondary ducts in which the ClO, ClOOCl, or $ClONO_2$ measurements are made. Each secondary duct, square cross section of 5.08 × 5.08 cm, is comprised of the following ten components, each identified in turn, along the direction of flow. (1) The entrance to each secondary duct is fitted with a fairing designed to minimize boundary layer growth such that the core of the secondary duct flow is assumed to be laminar. (2) A gate valve located immediately behind the fairing is opened in flight at P < 400 mbar on ascent and closed at P > 500 mbar on descent. (3) Nitric oxide (NO) gas diluted in N_2 (1:5) is mixed with a flow of N_2 carrier gas [200 sccm (standard $cm^3\ min^{-1}$)] and injected through an array of nine, perforated Teflon tubes. (4) A temperature sensing array consisting of seven thermistor beads suspended on wire supports measures the air temperature forward of the first detection axis to measure boundary layer growth. (5) A detection axis, located forward of the dissociation heater, is used to detect Cl atoms from ClO by UV resonance fluorescence. (6) The dissociation heater assembly consists of a grid of 28 resistively

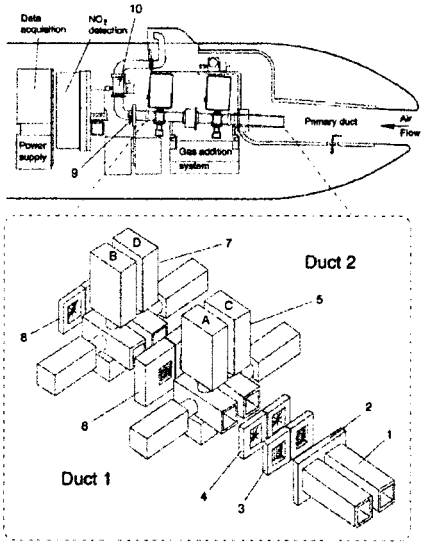

Figure 6-3. A cross-section of the instrument in the ER-2 wing pod and a perspective view of the components making up the secondary ducts in which the ClO, ClOOCl, and $ClONO_2$ measurements are made. See text for details.

heated silicon strips capable of introducing a step-jump in temperature to the flow while minimizing any wall interaction. Each silicon strip spans the cross section of the duct and is 0.041 cm thick and 0.84 cm wide, i.e., the dimension parallel to the flow. Each heater is designed for independently programmable operation up to 2.4 kW. (7) A second detection axis is located aft of the heater to detect Cl atoms from $ClONO_2$ and ClOOCl. (8) A second thermistor array measures air temperature downstream of the heater and aft detection axis. (9) A pitot tube, mounted in the center of the duct, is used for flow velocity and ambient pressure measurements. And finally, (10) a throttle valve is used to control flow velocity in the secondary duct at ~10 m/s; the throttle valve is closed whenever the gate valve is closed.

The twin secondary duct design was chosen to maximize measurement flexibility and diagnostic capability within the constraints dictated by available volume, allowable total weight, power consumption and thermal management. Other critical instrument components include the computer control and data acquisition system, the gas addition system, the dissociation heater controller and power supplies.

For SOLVE/THESEO-2000 the usual mode of instrument operation was such that in Duct 1, Axis A was used to measure ambient ClO and Axis B was used to measure ClOOCl and/or $ClONO_2$. In Duct 2, Axis C was used primarily with a prototype BrO detection axis and Axis D was used in a diagnostic mode to observe the temperature dependence of the ClOOCl and/or $ClONO_2$ thermal dissociation signals. The fluorescence signals at the detection axes forward of the heaters, axes A and C, are modulated primarily by the addition of NO. The fluorescence signals at the detection axes aft of the dissociation heaters, axes B and D, are modulated by the simultaneous operation of NO addition and the dissociation heater temperatures.

The NO addition cycle has a period of 35 sec and operates in synchronization with heater control algorithms that are of longer duration. Illustrations of the NO addition cycle are shown in Figures 6-4 and 6-5, with the observed fluorescence signals from axes A and B of duct 1, from the flight of 0202 (Feb 2, 2000. All flights discussed here took place in the year 2000). Figures 6-4 and 6-5 show data for which the dissociation heater is on (T = 363 K) and off (T = 218 K), respectively. The algorithm consists of four separate NO flows, stepping from high to low values, over an interval of 25 sec, followed by 10 sec of zero NO addition to record the null signal. The NO flow rates, 7.9, 3.9, 0.60, and 0.18 sccm, are chosen to accommodate the conversion of ambient ClO to Cl (or BrO to Br) atoms at the forward axes, for which the two smaller NO flows are optimized, and the conversion of ClO from dissociated ClOOCl and/or $ClONO_2$ at the aft axes, for which the two larger NO flows are optimized. Typically, the NO flow rates given above result in NO mixing ratios in the secondary duct of approximately 52, 26, 3.9 and 1.2 ppmv (parts per million by volume). In general, the aft axes require larger concentrations of NO because (a) the effective reaction time is shorter due to the faster velocity in the heated region compared to the cooler region, (b) thermal dissociation must take place prior to the conversion of fragment ClO to Cl, and (c) the higher temperature slows reaction (6) by approximately a factor of two. In addition, the aft axes are less prone to excessive Cl atom removal in the presence of excess NO, as discussed in more detail below, since the Cl atom removal mechanism slows considerably with increasing temperature. As evident in Figures 6-4 and 6-5, the relatively large NO flows optimized for the aft axes readily overtitrate the ambient ClO signal at the forward axis. This consequence proves beneficial as it provides the means to all but eliminate the contribution of ambient ClO to the observed signal at the aft axes for NO flows tailored to the detection of ClOOCl and $ClONO_2$ (Figure 6-5b).

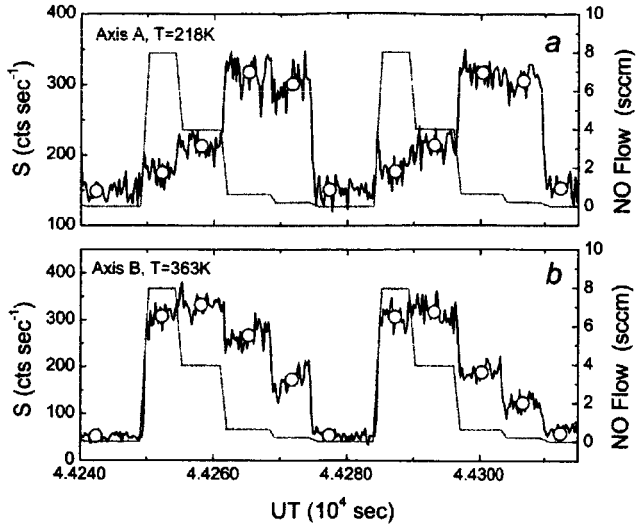

Figure 6-4. The NO addition algorithm and the observed fluorescence signals (cts sec^{-1}) versus time (sec) for axes A and B. Data are from the 0202 (Feb 2, 2000) flight. (a) Signal from axis A due to ambient ClO. (b) Signal from axis B when the air temperature is heated to 363 K. The signal at the higher NO flows is due to ClOOCl. The signal at the lower two NO flows is due to a mixture of ClOOCl and ambient ClO. Open circle symbols represent count rate averages calculated for each NO flow.

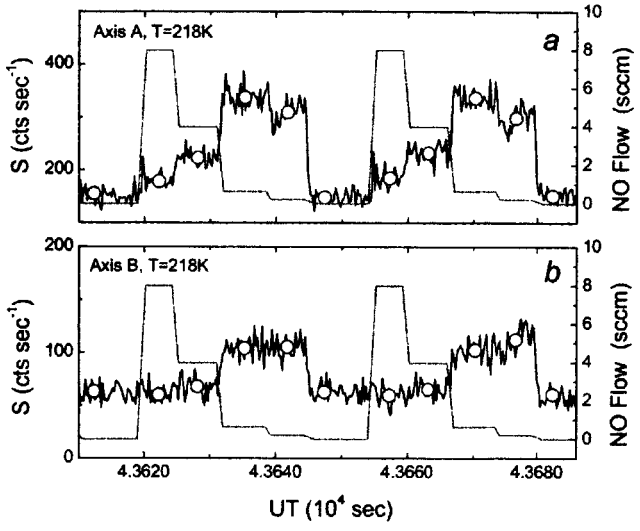

Figure 6-5. As in Figure 6-4, but for a flight segment where the dissociation heater is off. The signal at the highest two NO levels is largely unchanged relative to the background signal, indicating the complete removal of Cl atoms originating from amibent ClO.

The kinetics of the conversion of ClO to Cl by reaction with NO had been thought to be adequately described by the reaction sequence defined by (6) and the following reactions:

$$Cl + NO + M \rightarrow ClNO + M \qquad (9)$$

$$Cl + O_3 \rightarrow ClO + O_2 \qquad (10)$$

Fractional yields for ClO to Cl conversion, that are required for data analysis, are calculated with a model based upon flight conditions of T, P, flow velocity, [O_3] and [NO]. Since (9) is a Cl loss process, excessively high concentrations of NO will irreversibly remove Cl atoms to form ClNO. Thus NO addition in flight is varied to continually check that the yield is optimized. The presence of O_3 decreases the peak fractional conversion as it cycles Cl back into ClO. Other possible reactions of minor importance, such as the reaction of Cl with CH_4, have been neglected. The typical fractional yield for ClO to Cl conversion is ~0.8, assuming the above mechanism for the SOLVE observations.

However, an examination of the instrumental flight data from SOLVE has shown that Cl atoms are lost in excess NO more rapidly than the reaction sequence of (6), (9), and (10) can allow, especially as T decreases. Thus the presence of another non-negligible Cl removal process

is indicated that will necessarily lower the calculated yield of Cl atoms. A plausible mechanism is the reaction of ClOO with NO through the following reaction sequence [*Wilmouth*, 2002]:

$$Cl + O_2 + M \rightarrow ClOO + M \quad (11)$$

$$ClOO + M \rightarrow Cl + O_2 + M \quad (12)$$

$$ClOO + NO \rightarrow ClNO + O_2 \quad (13)$$

The relative importance of this mechanism is expected to be extremely T-dependent due to the thermal instability of ClOO. Laboratory measurements of the rate constant for ClOO production [*Nicholas and Norrish*, 1968; Nicovich *et al.*, 1991; Baer *et al.*, 1991] and the equilibrium constant for ClOO formation [Nicovich *et al.*, 1991; Baer *et al.*, 1991; Mauldin *et al.*, 1992; Avallone, 1993] have been reported and evaluated [Sander *et al.*, 2002]. There is one published, relative measurement of the rate constant of (13) at room temperature [Wongdontri-Stupor *et al.*, 1978]. Our understanding of reaction (13) would benefit from further laboratory work, particularly at low temperatures.

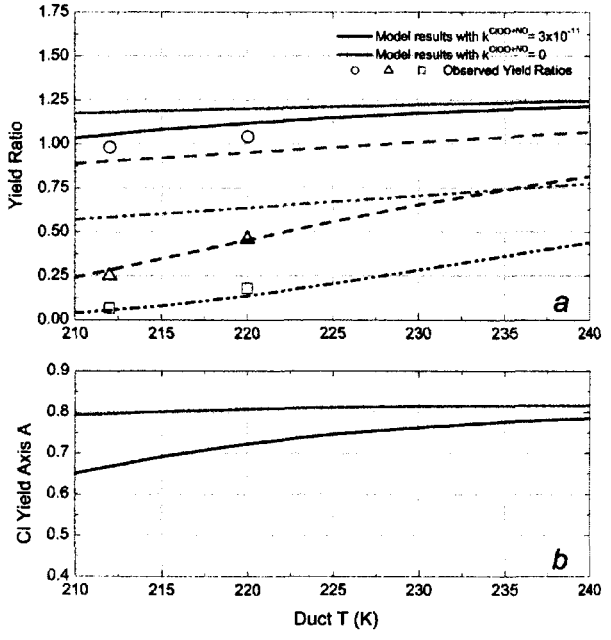

Figure 6-6. (a) The observed (symbols) and modeled (lines) yield ratios (see text for details) versus Duct T (K) for data from the 0305 flight. Observations are for data at T = 212 K (~ 42000 s UT) and T = 220 K (~ 52000 s UT). Three sets of lines for two different model runs are shown for $k^{ClOO+NO} = 3\times10^{-11}$ cm^3 molec^{-1} s^{-1} (black) and $k^{ClOO+NO} = 0$ (gray). Line types represent the model results, and symbols represent the observed ratios of Cl signals, for the following NO flow rates (sccm): 0.18/0.60 (circles and solid lines), 0.18/3.9 (triangles and dashed lines), and 0.18/7.9 (squares and dash-dot-dot lines). (b) The model calculated Cl yields at Axis A versus T. The effect on yield for the two different models is illustrated.

Evidence for the potential importance of (13) emerges from an examination of the observed Cl fluorescence signal as a function of NO concentration and temperature. The flight of 0305 is particularly revealing, since the ambient T varied from 192–200 K during a long segment of flight where the pressure did not vary significantly. The analysis is based on a comparison between the observed ratios of the Cl signal at the lowest NO flow relative to the three larger NO flows (hereafter referred to as the 'yield ratio') and model calculations assuming various scenarios of reaction mechanisms and rate constants. The conclusions are summarized in Figure 6-6a. The observed yield ratios shown as the symbols are the average values from two regions of the 0305 flight where the temperatures in the sample duct were 212 and 220 K, corresponding to ambient temperatures of 192 and 200 K, respectively due to ram heating. Since four NO flows are used there are three values of the yield ratio at each T. The only parameters that can cause changes in the observed yield ratios are (a) a change in the actual NO flows used, (b) a change in the flow velocity through the instrument affecting reaction times and NO mixing ratio, and (c) a change in the yield because of an extreme temperature-dependent reaction mechanism.

Possibilities (a) and (b) can be ruled out because the NO flow rates and the velocity measurements show no changes correlated with the observed changes in the yield ratios.

The most plausible explanation for the observed yield ratios is (c), an extreme temperature-dependent reaction. The black and gray lines of Figure 6-6a represent model calculations of the yield ratio for the conditions representative of the duct for this flight segment, P = 67 torr, velocity = 9 m/s, and O_3 = 1.6 ppmv, and where the rate constant for (14) is varied, $k^{ClOO+NO} = 3 \times 10^{-11}$ and 0 cm^3 $molec^{-1}$ s^{-1} (these units are used throughout), respectively. Clearly, the mechanism without the ClOO+NO reaction does not match the relative yield at any temperature very well, but more importantly, cannot impart a sufficient temperature dependence to the observed yield ratios for the over-titrated points, which here are the points at yield ratios < 0.5. The mechanism using $k^{ClOO+NO} = 3 \times 10^{-11}$ imparts a T dependence to the model that captures the essence of the observed Cl loss well. Values of the calculated fractional yield for the two different models are shown in Figure 6-6b. The calculation with $k^{ClOO+NO} = 3 \times 10^{-11}$ lowers the yield by ~15% at T = 215 K and ~10% at T = 220 K, with respect to the model using $k^{ClOO+NO} = 0$.

In the model discussed above, values for the rate constants for reactions (6) and (9)-(12) were taken from the JPL02 Evaluation [Sander *et al.*, 2002]. Additional runs were made to evaluate the partial derivative of the calculated yield with respect to changes in $k^{ClOO+NO}$. The yield was found to decrease by 14% for a doubling of $k^{ClOO+NO}$. When $k^{ClOO+NO}$ was halved, the yield increased by 7%. In a parallel effort we have begun work to measure the value of $k^{ClOO+NO}$ in the laboratory. Although we have not concluded that effort, preliminary results confirm that the removal of Cl due to NO is faster in the presence of O_2 compared to its removal in pure N_2 and that the rate of removal is more rapid as T is decreased. Preliminary results are consistent with the value 3×10^{-11} for $k^{ClOO+NO}$.

In summary, we have strong evidence, from *in situ* and laboratory data, that, concerning the conversion of ClO to Cl at low temperatures, subsequent chemistry of ClOO decreases the yield of chlorine atoms by titration with NO under the conditions of these measurements. Therefore, we have used the model above with $k^{ClOO+NO} = 3 \times 10^{-11}$ and values of temperature, pressure, velocity and [O_3] characteristic of flight conditions to calculate the yields for each ClO, ClOOCl and $ClONO_2$ measurement. Typical values of the fractional yield for ClO measured at the forward axis range from 0.65 to 0.75. Typical values of the yield used for the ClOOCl and $ClONO_2$ measurements from the aft axis range from 0.85 to 0.90 and are not affected by the inclusion of the ClOO + NO reaction, because at higher temperatures ClOO is essentially completely dissociated.

The heater control algorithms for the 'dither' mode used in duct 1 and the 'scanning' mode used in duct 2 are illustrated in Figure 6-7, which shows the average temperature (spatial average of 5 temperature sensors) at the aft thermistor array versus time. The dither mode steps between three different temperatures: T = 273 K, a null temperature where no dissociation takes place, T = 363 K for dissociation of ClOOCl exclusively, and T = 493 K for dissociation of $ClONO_2$, and ClOOCl if present. The three temperatures are stepped through sequentially in a 400 sec cycle, as shown in Figure 6-7a. At each temperature the NO addition algorithm runs through three cycles. The 'dither' mode is repeated three times followed by a heater off period of 60 s. The 'scanning' mode, which runs continuously in duct 2, ramps the temperature upward in 25 K increments from 0 to 503 K over a 700 s period, followed by a more rapid ramp downward in 300 s, as shown in Figure 6-7b.

The observed temperature dependence of the fluorescence signal resulting from thermal dissociation, shown in Figure 6-8, constitutes the primary diagnostic evidence demonstrating the ability to differentiate between ClOOCl and $ClONO_2$. The data from several different consecutive scans in air masses that are largely homogeneous with respect to chlorine loading and speciation over the time period of a complete up and down scan, 1000 s, are overlaid in Figure 6-8. For each scan, the observed Cl fluorescence signal is normalized by the peak observed signal for that scan. The data in Figure 6-8 are from two flights. The 0127 flight originated inside the vortex and penetrated the vortex wall in a southeasterly direction from Kiruna. From 0127, Figure 6-8a shows scans in air containing ClOOCl exclusively from inside the vortex and Figure 6-8b shows scans in air containing $ClONO_2$ exclusively from outside the vortex. The 0305 flight remained inside the vortex, and Figure 6-8c shows scans highly suggestive of air containing significant amounts of ClOOCl and $ClONO_2$. On 0127 inorganic chlorine in the vortex was evidently at or near complete activation, thus there is no $ClONO_2$ in the vortex (in the location of these observations). On 0305 partial chlorine recovery has taken place in the vortex. The data in Figure 6-8 are taken from Duct 2, Axis D and are used for diagnostic purposes only.

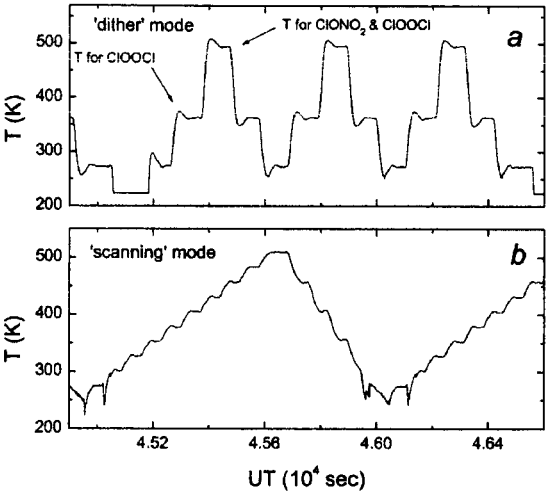

Figure 6-7. The 'dither' (a) and 'scanning' (b) heater control algorithms used in duct 1 and 2, respectively, illustrated as the observed T (K) measured at the aft temperature sensing assembly versus time (sec UT). These data are from the 0202 flight.

The results of Figure 6-8a suggest that ClOOCl is completely dissociated at temperatures of ~350 K, because no further increase in signal is observed as temperature is increased in the absence of $ClONO_2$. The character of the signal is clearly and dramatically different for $ClONO_2$, which requires heating to a temperature of ~ 493 K for complete dissociation, as was confirmed with observations from the POLARIS mission. The black line in all panels is a model that, due to its simplicity, must be considered semi-quantitative in nature. It indicates that there should be a region in which ClOOCl is fully dissociated while $ClONO_2$ is not dissociated, and the data largely agree. However, the data show that the temperature-driven dissociation curves are broadened toward the direction of lower temperature with respect to the model. It is suspected that this phenomenon arises because of the presence of locally hotter regions near the heater surface than indicated by the temperature measurement, which is spatially averaged and measured well downstream of the heater. Thus, for example, in the flight of 0305 (Figure 6-8c) we do not cleanly separate the two species in temperature space. A small empirical correction for the presence of $ClONO_2$ dissociation at T = 363 K is derived from observations in non-vortex air where there is no ClOOCl present.

While considerable refinement of details based on extensive laboratory studies has taken place, the general methodology to extract ClO concentrations from flight data is unchanged from previous descriptions [Brune *et al.*, 1989]. Summarizing the essentials only, the mixing ratio of ambient ClO is given by

$$ClO = \Delta S \times \left(\frac{dS/dM}{C}\right)^{Lab} \times \frac{1}{(dS/dM)^{Flight}} \times \frac{1}{Cl^{Yield}} \times T^{Corr} \times \text{Lyman } \alpha^{Corr} \times [M]^{-1} \quad (14)$$

where ΔS is the difference in the observed signal with and without NO present. The second term of Eq. (14) is the laboratory determined, density-dependent calibration factor, C (cts sec^{-1} / atom cm^{-3}), normalized against Rayleigh scattering, dS/dM, which serves as a measure of lamp flux. $(dS/dM)^{Flight}$ is the Rayleigh scattering signal determined from flight data based upon the background signal level given by the observed signal in the absence of NO. Cl^{Yield} is the fractional conversion of ClO to Cl by the reaction with NO as discussed above, typically = 0.7. T^{Corr} is a temperature correction for changes in the overlap integral between the Cl emission and absorption lines from the calibration which is determined at room temperature, typically = 1.03. Lyman α^{Corr} is a correction for hydrogen atom emission at 121.6 nm from the lamp that contributes to Rayleigh scatter but does not contribute to Cl sensitivity, typically = 1.10. $[M]^{-1}$ represents division by ambient density to convert the result to mixing ratio. ClOOCl concentrations are calculated similarly using the data from axis B, selected for temperatures centered on T = 363 K. $ClONO_2$ concentrations are calculated from data where T = 493 K, accounting for the presence of ClOOCl measured at the lower temperature.

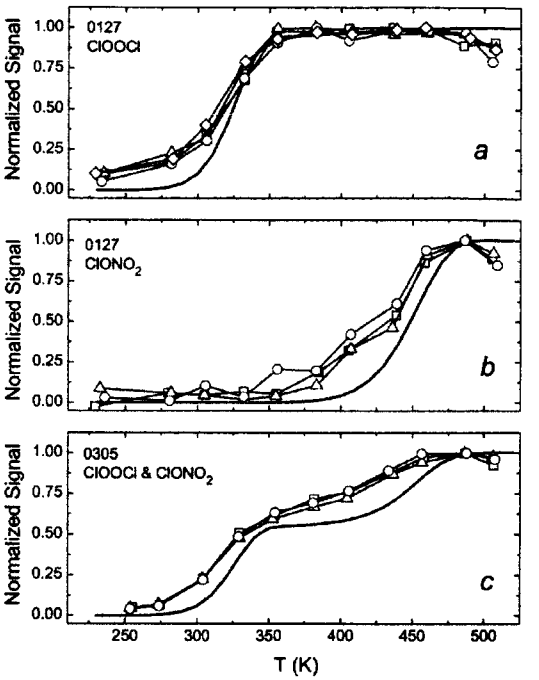

Figure 6-8. The temperature dependence of the observed signal at axis D, normalized to the maximum signal of each scan, versus T (K). (a) Data from the 0127 flight inside the vortex. (b) Data from the 0127 flight outside the vortex. (c) Data from 0305 inside the vortex. Different symbols represent results from individual scans. The solid line in each panel represents a model result.

A ClO measurement is reported every 35 s, the length of the NO addition cycle. ClOOCl and $ClONO_2$ measurements are reported less frequently as a consequence of the heater dither cycle. Nonetheless, every reported measurement of ClOOCl or $ClONO_2$ at the back axis represents an observation integrated over a 35 s time period, nearly concurrent (to within ~10 s) with a simultaneous ClO measurement at the front axis.

The estimated accuracy and detection limits (at 1σ confidence level) for the ClO measurements are ±17% and 3 pptv (parts per trillion by volume), respectively. The 1 sigma limits for the ClOOCl and $ClONO_2$ measurements are ±21% and 10 pptv, respectively. These uncertainty estimates are based upon the root-mean-square (RMS) sum for the estimated error for each of the terms in (14), as given in Table 1, columns 2 and 3.

We have assumed, as shown in Table 1 for the uncertainty contribution from ΔS, an additional uncertainty of 10% for the ClOOCl and $ClONO_2$, to acknowledge the possibility of additional unknown sources of error not related to the other entries in Table 1.

In this analysis, we use the ratio of $[ClOOCl]/[ClO]^2$ (= $[ClOOCl]/[ClO] \times 1/[ClO]$), extensively. In approximating the error of this ratio, we note that in the $[ClOOCl]/[ClO]$ factor there is some cancellation of error, whereas in the $1/[ClO]$ factor, all error enters in full. For example, the calibration factor, $((dS/dM)/C)^{Lab}$, is determined strictly in the laboratory and the identical expression is used for all axes. The systematic error in the Cl^{Yield}, T^{Corr}, and $[M]^{-1}$ terms is estimated to be similar for all axes and thus cancels. The remaining terms are lamp- or detection axis-specific and thus must enter in full. Columns 4 and 5 of Table 1 identify the common error terms (as dashes) and the resulting error for [ClO] and [ClOOCl] that is used to estimate the error in the ratio of $[ClOOCl]/[ClO]$. Thus, for the estimated accuracy in the ratio $[ClOOCl]/[ClO]^2$ we use the RMS sum of 17%, 10%, and 15%, (bottom row, columns 2, 4, and 5), which yields ±25% (1σ).

Table 1. Error Estimates[a]

	ClO	ClOOCl $ClONO_2$	ClO*[b]	ClOOCl* $ClONO_2$*
ΔS	2	12	2	12
$\left(\frac{dS/dM}{C}\right)^{Lab}$	12	12	-	-
$\frac{1}{(dS/dM)^{Flight}}$	8	8	8	8
Cl^{Yield}	6	6	-	-
T^{Corr}	2	2	-	-
Lyman α^{Corr}	5	5	5	5
$[M]^{-1}$	3	3	-	-
RMS sum[c]	17	21	10	15

[a]All errors are estimated as percentages at the 1σ level.
[b]The asterisk indicates common error terms that cancel in ratios are removed.
[c]The root-mean-square sum.

The thermal dissociation of ClOOCl may, in principle, proceed by multiple pathways to produce the following chlorine species: ClO, Cl, or Cl_2. In this analysis we have concluded, based upon the *in situ* observations and arguments discussed below, that ClOOCl thermally dissociates into two ClO fragments with unit yield. A possible Cl atom production channel can be ruled out by the *in situ* flight data. The direct production of Cl atoms as a result of heater operation in the absence of NO addition was never observed. An approximate upper limit on possible Cl atom production is 10 pptv, based upon the precision of the ClOOCl observations. A possible Cl_2 production channel is favorable thermodynamically and cannot be completely ruled out by the observational data. However, the mechanism that would be required is extremely unlikely, requiring the much weaker ClO–OCl bond to hold together long enough for the Cl atoms to come into close proximity in a four center intermediate state. Thus we have assumed the Cl_2 production channel to be unimportant, as has been similarly done in all of the previous laboratory (cross section and kinetic measurements) and *in situ* analyses involving ClOOCl that are referenced here. If Cl_2 and O_2 production were to occur, our reported ClOOCl concentrations would be biased low. We note that even in the unlikely event that up to 5% of ClOOCl thermally dissociated into the Cl_2 channel, the error in our ClOOCl measurement would only be 5%, which is small compared to our estimated error of ±21% (1σ) for ClOOCl.

We have previously carried out laboratory calibrations of $ClONO_2$ with this instrument, which indicated dissociation into ClO and NO_2 fragments with unit efficiency (±5%, 1σ) [Bonne, 1998]. Importantly, the $ClONO_2$ calibration demonstrates that (1) there are no outstanding issues concerning our understanding of instrumental sensitivity up to ~ 500 K and (2) there are no issues of unknown losses of chlorine species in the flight instrument as a result of passing through the heated region. We therefore similarly believe the ClOOCl yield to ClO is unlikely to be significantly different from unity.

The possibility that other chlorine oxide species may exist in the atmosphere cannot be ruled out by these measurements. However, given our present understanding of ClO_x photochemistry based upon laboratory measurements, it is doubtful that a significant part of the observed signal could be anything but ClOOCl. For example, it had been suggested that stratospheric Cl_2O_3 could form by reaction of ClO and OClO [Sander *et al.*, 1989]. However, laboratory measurements of the Cl_2O_3 formation rate and equilibrium constant result in estimates of the abundance of Cl_2O_3 that are several orders of magnitude less than the abundances of ClO and ClOOCl [Figure 8 of Burkholder *et al.*, 1993]. Formation of other higher oxides of chlorine probably occurs via reactions involving Cl_2O_3 [Sander *et al.*, 1989]. Thus the laboratory measurements of Burkholder *et al.* [1993] appear to rule out an important atmospheric role for this class of species. Nonetheless, if other unknown chlorine oxide molecules are contributing to the observed signal that we have attributed to ClOOCl, our reported concentrations of ClOOCl would be biased high.

Additional analyses of the SOLVE data set for (1) the inorganic chlorine budget and (2) the agreement of the $ClONO_2$ observations with simultaneous ClO and NO_2 observations [F. Keutsch, personal communication] provide collaborative evidence in support of the ClOOCl and $ClONO_2$ observations. These separate scientific topics are beyond the scope of the present paper.

Observations and Analysis

During the SOLVE/THESEO-2000 mission, ClOOCl measurements were acquired from eleven ER-2 flights taking place from Jan 14 to Mar 12, 2000, as summarized in Table 6-2. On the transit flight of 0114 from Westover, MA the ER-2 arrived in Kiruna, Sweden in darkness and, as indicated by the measurements of enhanced ClO at night, encountered the edge of the chemically activated vortex just prior to descent. All of the flights originating from and returning to Kiruna remained entirely within the vortex, except for the flights of 0127 and 0311, which were purposely flown through the vortex edge to sample extra-vortex air. The transit flight of 0316 to Westover, MA, took place outside of the vortex for its entirety. The acquisition of an ensemble of flights in air masses of dramatically different character was crucial for diagnosing instrument behavior.

Table 6-2. Flight Summary

Flight[a]	Latitude[b]	Longitude	SZA	Vortex[c]	ClO[d]	ClOOCl	$ClONO_2$
0114	42–72	72W–20	79–125	transit	80	170	700
0120	65–89	12–21	86–114	inside	750	850	< det limit[f]
0123	59–74	9–21	78–97	inside	1600	na[e]	< det limit
0127	52–68	20–37	74–97	extra	1300	900	900
0131	68–79	12–21	86–97	inside	800	900	< det limit
0202	64–78	11–63	83–104	inside	1100	1100	< det limit
0203	68–73	20–29	117–129	inside	120	1050	< det limit
0226	63–85	12–21	79–94	inside	1100	700	950
0305	67–81	10–65	73–95	inside	1100	480	1100
0307	68–83	20–75	78–89	inside	1200	490	1400
0311	59–75	4W–30	65–87	extra	1100	280	1300
0312	65–79	5–54	72–94	inside	900	340	1100
0316	42–68	70W–20	44–77	transit	100	< det limit	500

[a]0114 = 14 Jan 2000.

[b]Columns for latitude, longitude and solar zenith angle show the min and max values in degrees characterizing each flight. All latitudes are for the northern hemisphere. Longitudes are east if not labeled otherwise.

[c]The character of the flight with respect to the vortex position, extra indicates significant flight segments both inside and outside of the vortex wall. Transit flights originated or terminated at Westover, MA.

[d]ClO, ClOOCl and $ClONO_2$ columns show maximum observed concentrations in pptv.

[e]ClOOCl was not reported for this flight due to NO addition error at max values required for ClOOCl and $ClONO_2$ detection.

[f]Indicates no measurements submitted since signal was below the detection limit.

To provide some perspective on the overall data set, in Figures 6-9 and 6-10 we plot the observed ClOOCl and ClO mixing ratios from the flights of 0202 and 0311, with selected model results. These flights are representative of the mid- and late-winter observations provided by the SOLVE ER-2 deployments. The model calculations are carried out for different input values for absorption cross sections (used to derive J values) and rate constants. The standard case is the one that includes JPL02 recommendations for all input values, except for $k^{Prod} = k^{JPL00}$, since the various values of k^{Prod} have particular relevance in this analysis. For the sake of clarity, only three model results are shown in Figures 6-9 and 6-10, for different choices of the J value: J^{JPL02}, J^{Huder} and J^{NearIR}. An examination of Figures 6-9 and 6-10 yields preliminary conclusions that are more quantitatively developed in the analysis that follows.

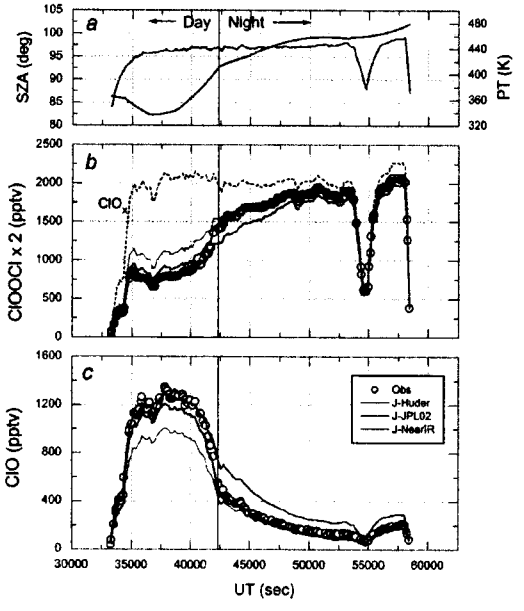

Figure 6-9. Observation-model comparison for the flight of 0202. (a) Solar zenith angle (deg) in blue and potential temperature (K) in red versus UT (sec). A vertical line marks the sunset transition at 92° SZA. (b) ClOOCl × 2 (symbols) and various model calculations: the standard case with J^{JPL02} (blue), J^{Huder} (green) and J^{NearIR} (red). The dashed line represents total observed ClO_x = ClO + ClOOCl × 2. (c) As in (b) but for ClO.

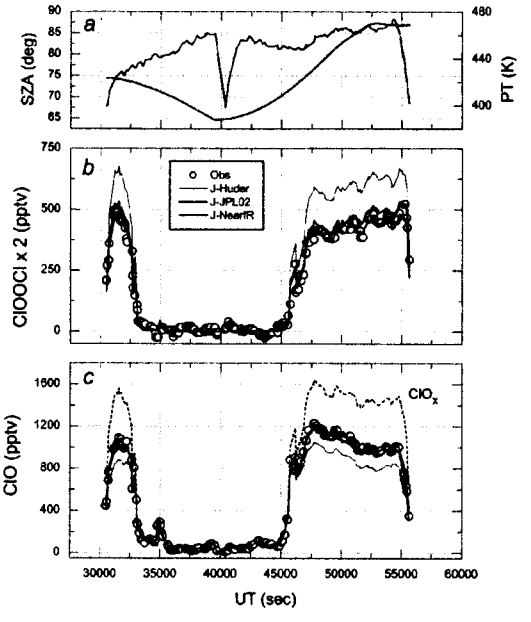

Figure 6-10. Observation-model comparison for the flight of 0311. Description similar to Figure 6-9.

The flight of 0202 provides an outstanding example of the diurnal behavior of ClO_x through a sunset transition in the activated vortex. For this flight, the ER-2 flew initially in an easterly direction to 60°W, northwesterly to 78°N, then southerly back to Kiruna. The solar zenith angle (SZA) and potential temperature are shown in Figure 6-9a. Observed ClO and ClO_x, given by the sum of ClO and ClOOCl × 2, are shown in Figure 6-9b. Observed ClOOCl is shown in Figure 6-9c. Focusing on the implications of the modeled J value, the speculative J^{NearIR} is not supported by the observations, as it clearly leads to excessive ClOOCl photolysis during the sunset transition. The J^{Huder} value underpredicts the amount of ClOOCl photolysis throughout the

sunlit portion of the flight. The J^{JPL02} value yields the best observation-model agreement. The observation versus model comparison for the nighttime portion of the flight is presented in Section 4.2.

The flight of 0311 (data shown in Figure 6-10) took place near the end of the SOLVE mission, when ClO_x/Cl_y levels demonstrably started a recovery to lower levels. For this flight the ER-2 flew initially in a southwesterly direction to 58°N , 5°E, then northwesterly back to Kiruna, followed by a short northerly survey to 75°N. The change from vortex to extra-vortex air is dramatically indicated by the pronounced drop in observed ClO_x abundances (Figure 6-10c) near UT 32500 s (~67°N). The ER-2 re-entered the vortex at about UT 46000 s. These sharp transitions are also present in observed mixing ratios of long-lived tracers of atmospheric motion, such as N_2O and CH_4 [J. Elkins, private communication, 2003]. As was seen for the measurement versus model comparisons for the flight of 0202, the JPL02 model simulates fairly well the observed variations of ClO and ClOOCl with SZA, whereas a model using J^{Huder} tends to underestimate observed ClO and overestimate measured ClOOCl. The simulation using J^{NearIR} is nearly identical to the J^{JPL02} model result, because by design the two photolysis rates are in near agreement for solar zenith angles less than 85°. As noted above, the two photolysis frequencies diverge at higher zenith angles, due to high optical depths in the UV (caused by Rayleigh scattering) that cause greater reductions in J^{JPL02} compared to J^{NearIR}.

Another important aspect of the model-measurement comparison for ClO and ClOOCl is that the agreement does not show any apparent sensitivity to the presence of polar stratospheric cloud (PSC) particles. The ER-2 flew through air containing large, nitric acid-bearing PSCs for long portions of the flight track on 0120, and for significant portions of flights on 0131 and 0203 [Fahey *et al.*, 2001]. Yet the quality of measurement/model comparison is unchanged in the presence of these PSCs, relative to neighboring air-masses with similar abundances of tracers but no PSC particles. This indicates that, for these observations, possible heterogeneous reactions of ClOOCl or ClO on particle surfaces have no effect on the partitioning of ClO_x between ClOOCl and ClO.

Daytime analysis

In this analysis the parameter of primary interest is the ratio of [ClOOCl] and $[ClO]^2$, denoted herein as α,

$$\alpha = \left(\frac{[ClOOCl]}{[ClO]^2} \right) \qquad (15)$$

where square brackets denote observed (obs) concentrations (molec cm^{-3}). When ClOOCl and ClO are close to instantaneous photochemical stationary state (PSS) (i.e., when the rates of production (3) and loss (4 and 5) of ClOOCl are nearly equal), this ratio tests our understanding of the key photochemical parameters that control both the partitioning of ClO and ClOOCl, as well as ozone loss:

$$\left(\frac{[ClOOCl]}{[ClO]^2} \right)_{PSS}^{Obs} = \frac{k^{Prod}}{J + k^{Loss}} \qquad (16)$$

As noted above, our analysis uses a fully time-dependent model, which provides for analysis of all available data. Thus, relation (16) is only heuristic. The time-dependent model used to calculate [ClO] and [ClOOCl] includes a full treatment of the kinetics, including minor terms such as thermal decomposition of ClOOCl during both day and night.

Using the time-dependent model, we compare the ratio of α defined by the observations and α defined by the model results, denoted herein as β,

$$\beta = \frac{\alpha^{Obs}}{\alpha^{Model}} = \left(\frac{[ClOOCl]}{[ClO]^2}\right)^{Obs} \Big/ \left(\frac{[ClOOCl]}{[ClO]^2}\right)^{Model} \qquad (17)$$

Since the loss rate of ClOOCl is dominated by photolysis during the day and by thermal dissociation during the night, the analysis can independently test the sensitivity of β to various choices for the ratios of J/k^{Prod} and k^{Loss}/k^{Prod} used in the model, respectively. Thus for the daytime analysis, β is primarily influenced by the ratio of J/k^{Prod} used in the model, and values of β will scale as follows,

$$\beta^{Daytime} \propto \left(\frac{[ClOOCl]}{[ClO]^2}\right)^{Obs} \times \left(\frac{J}{k^{Prod}}\right)^{Model} \qquad (18)$$

When β equals unity there is agreement between the observations and the model.

The daytime analysis is summarized by the plot of β versus SZA (Figure 6-11), calculated for various model runs, for all of the simultaneous observations of ClO and ClOOCl obtained during SOLVE. Values of β are regressed against SZA to examine the accuracy of the J value as a function of SZA. A comparison of the relative rates of ClOOCl loss by photolytic and thermal dissociation indicates that photolysis dominates (>90%) out to 92° SZA for all reasonable values of J and k^{Loss} at the temperatures characteristic of this study. Thus, the daytime analysis is carried out to 92° SZA. Results are shown for four possible values of both J and k^{Prod}. Figure 6-11a shows the underlying data and averaged values for the standard case, JPL02 recommendations adopted for all input except for $k^{Prod} = k^{JPL00}$. The data are averaged in eleven 2°-wide bins from 70 to 92° SZA. Figures 6-11b, c, d, and e show the average results for other cases considered, as identified by the labels. The estimated uncertainty of α^{Obs} (±25%, 1σ) is represented in the error in β as indicated by the error bars, shown for selected points only for clarity. The relative precision, given by the standard deviation of the mean, of the averages shown in Figure 6-11 are typically 1 to 2%, but in a few cases reach a maximum of 6%. Thus, in all cases, the uncertainty represented by the standard deviation of the mean values of β is negligible (if added in quadrature) compared to ±25%. For the purposes of this comparison we are not assigning any error to the model, which would normally include contributions from the error estimates in the rate constants and cross sections required in the model. The estimated error in the rate constants is usually of the

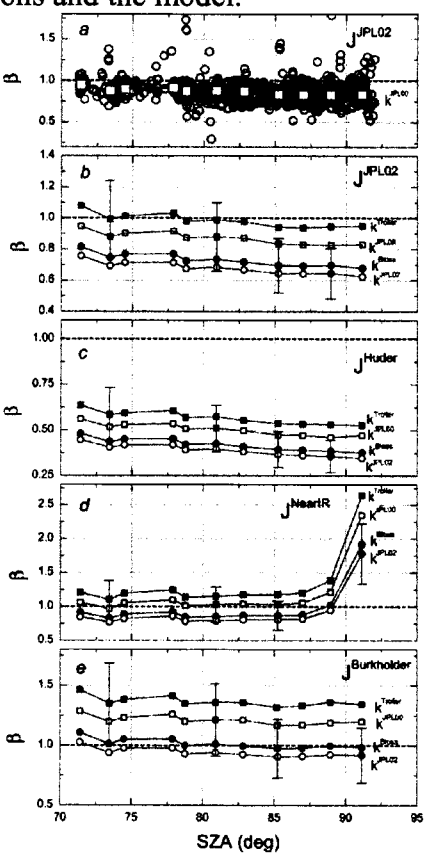

Figure 6-11. Daytime analysis of all flights, β (unitless) versus SZA (deg). Data selected for SZA<92° and M<3.0×10^{18} molec cm^{-3}. (a) Unaveraged and averaged data for the standard case, k^{JPL00} and J^{JPL02}. Averages are calculated for 2° width bins from 70 to 92° SZA. (b) Average values for J^{JPL02} and four different values for k^{Prod} as indicated. (c) As above but for J^{Huder}. (d) As above but for J^{NearIR}. (e) As above but for $J^{Burkholder}$. Error bars depict ±25% error attributable to the observations.

same order as that in α^{Obs}.

The choices for J considered here are J^{JPL02}, J^{Huder}, J^{NearIR}, and $J^{Burkholder}$. Values for k^{Prod} are taken from: the 2000 JPL Evaluation (k^{JPL00}); the recent laboratory work of Bloss *et al.* [2001] (k^{Bloss}); the earlier work of Trolier *et al.* [1990] ($k^{Trolier}$); and the most recent 2002 JPL Evaluation (k^{JPL02}). These four values span the range of variation of different measurements of k^{Prod}. The values for k^{Prod} of Sander *et al.* [1989] and Nickolaisen *et al.* [1994] lie close to the consensus value of k^{JPL00}. Bloss *et al.* [2001] report k^{Prod} to be ~30 to 20% larger than k^{JPL00} over the temperature range characteristic of this data set, $190 < T < 200$ K, respectively. The value given by k^{JPL02} is the largest over this T range, ~35 to 25% larger than k^{JPL00}, respectively. The $k^{Trolier}$ value is ~10 to 15% smaller than k^{JPL00} over this T range, respectively. Recent work based upon the observed rate of removal of ClO in the stratosphere observed from a balloon-borne *in situ* instrument is consistent with the larger k^{Bloss} rate constant [Vömel *et al.*, 2001].

The interpretation of the results of Figure 6-11 is somewhat complicated by the fact that we can test only the ratio of J over k^{Prod}, not individual values of either J or k^{Prod}. We have therefore plotted every permutation of the four choices of J and k^{Prod} in panels b, c, d and e of Figure 6-11.

Focusing on the J values first, the model results using J^{Huder} (Figure 6-11c) are markedly low (β ~0.6 to 0.4) for all four choices of k^{Prod}. In other words, model runs using photolysis rates for ClOOCl based on the Huder and DeMore [1995] cross sections tend to underestimate measured ClO and overestimate ClOOCl, as shown in Figures 6-9 and 6-10. Quantitative difficulties with J values for ClOOCl based on the cross sections of Huder and Demore [1995] have previously been shown, based upon an imbalance of the inorganic chlorine budget when measurements of ClO are available and the PSS approximation is used to estimate ClOOCl [Shindell and deZafra, 1995; Shindell and deZafra, 1996; Stachnik *et al.*, 1999].

The results for β using J^{NearIR}, Figure 6-11d, are much larger than unity in the 92° SZA bin, that which is most sensitive to this process. As noted earlier, model results for J^{NearIR} are similar by design to results using J^{JPL02} for the more sunlit portion of the day. This behavior is independent of choice of k^{Prod}. Additional photolysis of ClOOCl occurring in the near IR (λ>800 nm) region of the spectrum is unlikely. We conclude that both J^{Huder} and J^{NearIR} can be ruled out, at the 2 σ and 1σ confidence levels, respectively.

The SOLVE/THESEO-2000 observations are in excellent agreement with the combination of J^{JPL02} and the ClOOCl production rate constant of $k^{Trolier}$ (Figure 6-11b). However considering the estimated error of α^{Obs} (±25%), the observations cannot rule out the larger value of k^{JPL00} if ClOOCl photolyzes in a manner consistent quantitatively with J^{JPL02}. Choosing the progressively more rapid values for the ClOOCl production rate constant given by k^{Bloss} and k^{JPL02} further depresses β. Since the model–observation disagreement with the adoption of k^{Bloss} and k^{JPL02} with J^{JPL02} appears to be statistically significant at the 1 sigma level, we conclude that if k^{Bloss} or k^{JPL02} represents the true value of k^{Prod}, then the J value for ClOOCl must also be greater than J^{JPL02} in order to bring β back towards a value of unity.

The model results using $J^{Burkholder}$ (Figure 6-11e) yield remarkably good agreement between modeled and measured $[ClOOCl]/[ClO]^2$ for either k^{Bloss} or k^{JPL02}. The value of β found using the combination of $J^{Burkholder}$ and k^{JPL00} is ~25% greater than unity, equal to the estimated error of α^{Obs}. If the true photolysis rate of ClOOCl proceeds at a rate close to $J^{Burkholder}$, then our observations appear to be inconsistent with the rate for formation of ClOOCl given by $k^{Trolier}$.

J^{ClOOCl} decreases by nearly two orders of magnitude as SZA increases from 72 to 92° (Figure 6-2a). The overall shape of J^{ClOOCl} is captured remarkably well by all of the models that only allow for photolysis of ClOOCl in the UV, as shown by the nearly constant values of β with respect to SZA in Figure 6-11b, c, and e. The slight negative trend in β with increasing SZA for all cases using J^{JPL02} might indicate that the photolysis of ClOOCl in the real atmosphere is shifted slightly to the red of the spectral maximum of ClOOCl photolysis found in this model. Indeed, the photolysis of ClOOCl for $J^{Burkholder}$ is slightly red-shifted compared to J^{JPL02}, leading to essentially no trend in β (Figure 6-11e). The precise shape of β with respect to SZA is quite sensitive to how σ^{ClOOCl} is estimated longward of 410 nm. A slight negative trend would have resulted for $J^{Burkholder}$ had we set σ^{ClOOCl} equal to zero for $\lambda > 410$ nm, rather than use the log-linear extrapolation shown in Figure 6-1.

In summary, the analysis of the daytime partitioning of ClO and ClOOCl tests the ratio J/k^{Prod}. The observations are consistent with several combinations of J and k^{Prod}. If ClOOCl photolyzes at a rate similar to J^{JPL02}, then best consistency with α^{Obs} is found for the value of k^{Prod} reported by *Trolier et al.* [1990] or JPL00. Alternatively, if $J^{Burkholder}$ represents the true J value for ClOOCl, then best consistency is found for k^{Prod} of Bloss *et al.* [2001] or JPL02. The data are not consistent with J values for ClOOCl given by J^{Huder} or J^{NearIR}, for any choice of k^{Prod}.

The observations used in Figure 6-11 include all measurements inside the vortex where SZA<92° and [M]< 3.0×10^{18} molec cm^{-3}. Since the bulk of the data come from ER-2 cruise flight conditions, the M binning serves only to remove some outliers resulting from low signal-to-noise ratios. The conclusions do not change if the M binning is removed. This binning selects a total of 1005 simultaneous measurements of ClOOCl and ClO. The T ($189 < T < 202$ K) and [M] ($1.7\times10^{18} < [M] < 3\times10^{18}$) distributions of the selected atmospheric data are uncorrelated with SZA, thus there is no trend in the data related to the T and M dependence of k^{Prod}.

Avallone and Toohey [2001] derived a lower limit for J using ClO observations from AASE (Airborne Arctic Stratospheric Expedition) II and maximum possible abundances of ClOOCl assuming complete activation of Cl_y, i.e., $[ClO] + 2[ClOOCl] = [Cl_y]$. Using the recommendation for k^{Prod} of Sander *et al.* [1989], which is nearly identical to k^{JPL00}, they found that the variation in this empirical J value with SZA was consistent with that of modeled ClOOCl photolysis. However, their lower limit fell between the photolysis rates calculated from cross sections of Huder and DeMore [1995] and from JPL00. They concluded that their lower-limit J value was likely closer to those based on the Huder and DeMore [1995] cross sections than on the JPL00 recommended cross sections for their choice of k^{Prod}. If the same analysis were repeated today using the more recent k^{Bloss} determination, their lower limit would be pushed closer to JPL00 (or JPL02) by about 15-20%, effectively ruling out the Huder and Demore [1995] cross sections at the 1 sigma level of uncertainty (D. Toohey, personal communication).

While our ClOOCl photolysis rates agree with Avallone and Toohey [2001] within 2 sigma error, our derived J values are systematically higher than the lower limit they calculated. There are several possible explanations for this, including: (1) the AASE II measurements may never have been made in air that was 100% activated, i.e., ClO and ClO dimer never fully accounted for 100% of the inorganic chlorine budget in sunlight during AASE II, (2) the ClO observations from AASE II are systematically low, perhaps due to a loss of chlorine atoms by reactions of ClOO similar to that noted here, and (3) our new measurements of ClOOCl are systematically low. It remains unclear what effect the ClOO+NO reaction would have on their reported ClO values, but it is likely less than 5% under the temperatures and pressures that prevailed during the daylight observations during AASE II (L. Avallone, personal

communication). We speculate that the most likely explanation for the differences between our results and theirs is the assumption that ClO and ClOOCl represent 100% of the inorganic chlorine budget, something that we rarely observed during SOLVE/THESEO-2000. We are presently examining the inorganic chlorine budget for January-March 2000 with a more complete suite of measurements to address this issue, the results of which could have important implications for calculations of ozone loss rates.

Nighttime analysis

The nighttime analysis corresponds to an observation-model comparison for the equilibrium constant for dimer formation since

$$\beta^{\text{Nighttime}} \approx \left(\frac{[\text{ClOOCl}]}{[\text{ClO}]^2}\right)^{\text{Obs}} \times \left(\frac{k^{\text{Loss}}}{k^{\text{Prod}}}\right)^{\text{Model}} \qquad (19)$$

and $K^{Eq} = k^{Prod}/k^{Loss}$. In the time-dependent model the value chosen for K^{Eq} determines the value of k^{Loss}. The night results are not of primary importance with respect to catalytic loss of ozone since the thermal cycling of ClOOCl and ClO constitutes a null cycle that does not destroy ozone. However, comparing values of K^{Eq} inferred from these observations with other determinations of K^{Eq} provides further insight into the character of these observations and our understanding of ClO_x chemistry.

In addition to the flight of 0202 shown in Figure 6-10, the flights of 0120, 0131, and 0203 have simultaneous ClOOCl and ClO measurements in darkness. From these four flights the value of β, selected for SZA>95°, are plotted versus T in Figure 6-12. In Figure 6-12a we show β calculated for the combination of k^{Bloss} and K^{Cox} [Cox and Hayman, 1988]. Data are averaged in five bins of width 2 K from 190 to 200 K. The values of β are more scattered for the night observations compared to the day observations, since there is more noise associated with the relatively low values of ClO observed at night.

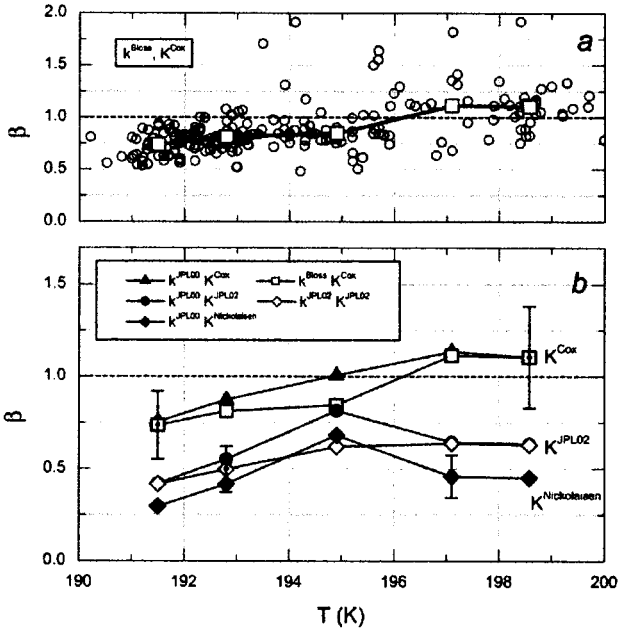

Figure 6-12. Nighttime analysis of all flights, β versus T. Data selected for SZA>95°. (a) Unaveraged and averaged data for the case of k^{Bloss} and K^{Cox}. Averages are calculated for 2 K width bins from 190 to 200 K. (b) Average values only for (1) K^{Cox} with k^{JPL00} and k^{Bloss} (2) K^{JPL02} with k^{JPL00} and k^{JPL02}, and (3) $K^{Nickolaisen}$ with k^{JPL00}. Error bars depict ±25% error attributable to the observations. The laboratory determinations of K^{Eq} are based on experiments conducted at warmer temperatures than the atmospheric measurements, and hence values are extrapolated with respect to temperature (see text).

In Figure 6-12b the averaged results for the observation–model comparison are shown for three values of the equilibrium constant and various values of k^{Prod}: K^{Cox} [Cox and Hayman, 1988] with k^{Bloss} and k^{JPL00}, K^{JPL02} [Sander *et al.*, 2002] with k^{JPL00} and k^{JPL02}, and $K^{Nickolaisen}$ [Nickolaisen *et al.*, 1994] with k^{JPL00}. The JPL02 recommendation for K^{Eq} is unchanged from the JPL00 recommendation. Over the temperature range characteristic of these observations, 190 < T < 200 K, K^{Cox} is ~50% less than K^{JPL02}, and $K^{Nickolaisen}$ is ~40% greater than K^{JPL02}. The minimum T

characterizing the $K^{Nickolaisen}$ determination was 260 K; thus, this comparison requires a rather long extrapolation to the temperatures of interest here. The minimum T for the determination of K^{Cox} was 233 K. As the value of K^{Eq} increases, the amount of ClO at night for a given ClO_x level will decrease.

The observations are in relatively good agreement with K^{Cox}, for either k^{Bloss} or k^{JPL00} for the ClOOCl production rate constant. The result using $k^{Trolier}$ is not shown because it yields results nearly identical to those from k^{JPL00}. The precision in the nighttime results is not sufficiently good to constrain the value of k^{Prod}. If all of the observations used in Figure 6-12 were in instantaneous PSS, then the model-observation comparison would in principle only be sensitive to K^{Eq}. However, because some observations that are not in PSS are included, in the time dependent analysis the model-observation comparison should and does show some sensitivity to the choice of k^{Prod}. The larger values of K^{JPL02} and $K^{Nickolaisen}$ result in progressively lower average values of β. Considering the error in α^{Obs} of ±25% (1σ), these results suggest that K^{JPL02} and $K^{Nickolaisen}$ are approximately too large by factors of 1.7 and 2.5, respectively.

The result using $K^{Avallone}$ [Avallone and Toohey, 2001] is not shown in Figure 6-12, since it is essentially identical to K^{Cox} over the temperature range of these observations ($190 < T < 200$ K). The value for $K^{Avallone}$ was derived from nighttime, *in situ* ClO data from the ER-2 during the AASE I mission of 1988/89. Since ClOOCl was not measured, the analysis assumed $ClO_x = Cl_y$. If this assumption is not valid, the derived value for $K^{Avallone}$ represents an upper limit to the actual value of the equilibrium constant. If the AASE ClO data set is biased low, (e.g., point 2 above) the inferred value of K^{Eq} from that data set would be even smaller. Together with this earlier study, our new observations present a strong case that the value of K^{Eq} relevant under stratospheric conditions is less than that of the current JPL recommendation by a significant margin. Additional laboratory studies of this process are clearly warranted.

Conclusions

The existence in the stratosphere of ClOOCl, a key species that propagates the catalytic destruction of polar ozone, has been demonstrated for the first time. The capability to measure [ClO] and [ClOOCl] simultaneously provides the ability to observe ClO_x directly, in day or nighttime conditions. The SOLVE/THESEO-2000 observations provide quantitative tests of the laboratory measurements of key parameters that control the rate of polar ozone depletion, k^{Prod} and J, i.e., the production rate constant and the photolysis rate of ClOOCl, for a wide range of solar zenith angles.

The observations of ClO and ClOOCl are in good agreement with the magnitude and solar zenith angle (SZA) dependence of J based on the JPL02 cross sections for ClOOCl [Sander *et al.*, 2002], J^{JPL02}, when coupled with a value for k^{Prod} taken from the JPL00 recommendation, or a smaller value for k^{Prod} (~15% smaller) based upon Trolier *et al.* [1990].

However, the most recent laboratory measurement of k^{Prod} by Bloss *et al.* [2001], k^{Bloss}, is considerably larger than the JPL00 recommendation and has led to a still larger value of k^{Prod} given by the JPL02 recommendation, k^{JPL02} [Sander *et al.*, 2002]. Our analysis suggests that the values given by k^{Bloss} and k^{JPL02} are only consistent with observed ClO and ClOOCl if the J value for ClOOCl is increased substantially relative to the J^{JPL02}. A J value derived from the larger absorption cross sections for ClOOCl reported by Burkholder *et al.* [1990], extrapolated to 450 nm using a log-linear relation, combined with either k^{Bloss} or k^{JPL02}, leads to good agreement with the observed partitioning of ClO and ClOOCl. Increasing both J and k relative to JPL00 recommendations will lead to substantial increases in the calculated rate of ozone destruction by

the ClO dimer cycle, because chlorine is cycled more quickly through the various steps of the cycle.

A speculative value for the photolysis rate of ClOOCl, which tests the possibility of additional photolysis longward of 800 nm, is effectively ruled out by the observations, for all values of k^{Prod}. Also, a value for J calculated using the ClOOCl cross sections of Huder and DeMore [1995], which are smaller compared to other laboratory data for wavelengths greater than ~310 nm, is inconsistent with the observed behavior of ClO and ClOOCl, again for all values of k^{Prod}.

The modeled value of J^{ClOOCl} declines by a factor of ~20 as SZA increases from 72 to 92°, yet values of β in Figure 6-11 are nearly flat for J^{JPL02} and essentially flat for $J^{Burkholder}$. The quantity β represents the accuracy of the model representation of the ratio J/k^{Prod} for daytime observations. The results in Figure 6-11 indicate that our radiative model captures the overall magnitude and spectral dependence of ClOOCl photolysis quite well, especially for the case of $J^{Burkholder}$.

From the nighttime analysis, the laboratory determination of K^{Eq} from Cox and Hayman [1988] agrees best with our simultaneous observations of ClO and ClOOCl, which span atmospheric temperatures of 190 to 200 K. This result is consistent with the conclusions of Avallone and Toohey [2001]. The larger values of K^{Eq} from the JPL02 recommendation [Sander *et al.*, 2002] and Nickolaisen *et al.* [1994] are not consistent with the observations by statistically significant factors of approximately 1.7 and 2.5, respectively. All of the laboratory determinations of K^{Eq} are based on experiments at considerably warmer temperatures than the atmospheric observations.

The rate of ozone depletion by the ClO-ClOOCl cycle is sensitive to the absolute magnitude of k^{Prod} and J, whereas the observations presented here constrain only the ratio of these parameters. Thus, any changes in excess of approximately ±25% (the estimated error in $[ClOOCl]/[ClO]^2$) to the ratio of J/k^{Prod} must occur in concert.

It is important to note that since the partitioning of ClOOCl and ClO is not sensitive to the quantum yield for photolysis into the chlorine atom channel (4a) relative to the total photolysis rate, these observations cannot provide information on this critical branching ratio. Verification of the yield of (4a) with atmospheric observations rests with inferences drawn from comparisons of observed ozone destruction rates with calculated ozone destruction rates constrained by radical observations.

References

Anderson, J. G, H. J. Grassl, R. E. Shetter, and J. J. Margitan, Stratospheric free chlorine measured by balloon-borne *in situ* resonance fluorescence, *J. Geophys. Res., 85*, 2869–87, 1980.

Anderson, J. G., W. H. Brune, and M. H. Proffitt, Ozone destruction by chlorine radicals within the Antarctic vortex: The spatial and temporal evolution of ClO-O_3 anticorrelation based on *in situ* ER-2 data, *J. Geophys. Res., 94*, 11,465–79, 1989.

Anderson, J. G., D. W. Toohey, and W. H. Brune, Free radicals within the Antarctic vortex: The role of CFCs in Antarctic ozone loss, *Science, 251*, 39-46, 1991.

Avallone, L, M., *In situ* measurements of ClO and implications for the chemistry of inorganic chlorine in the lower stratosphere, PhD Thesis, Harvard University, 1993.

Avallone, L. M. and D. W. Toohey, Tests of halogen photochemistry using *in situ* measurements of ClO and BrO in the lower polar stratosphere, *J. Geophys. Res., 106*, 10,411–21, 2001.

Baer, S., H. Hippler, R. Rahn, M. Siefke, N. Seizinger, and J Troe, Thermodynamic and kinetic properties of the reaction $Cl+O_2+M \leftrightarrow ClOO+M$ in the range 160-300 K and 1-1000 bar., *J. Chem. Phys., 95*, 6463–70, 1991.

Becker, G., R. Müller, D. S. McKenna, M. Rex, K. S. Carslaw, and H. Oelhaf, Ozone loss rates in the Arctic stratosphere in the winter 1994/1995: Model simulations underestimate results of the Match analysis, *J. Geophys. Res., 105*, 15,175–84, 2000.

Birk, M., R. R. Friedl, E. A. Cohen, H. M. Pickett, and S. P. Sander, The rotational spectrum and structure of chlorine peroxide, *J. Chem. Phys., 91*, 6588–97, 1989.

Bloss, W. J., S. L. Nickolaisen, R. J. Salawitch, R. R. Friedl, and S. P. Sander, Kinetics of the ClO self-reaction and 210 nm absorption cross section of the ClO dimer, *J. Phys. Chem. A, 105,* 11,226–39, 2001.

Bonne, G. P., *In situ* measurements of chlorine nitrate in the lower stratosphere, PhD Thesis, Harvard University, 1998.

Brune, W. H., J. G. Anderson, and K. R. Chan, *In situ* observations of ClO in the Antarctic: ER-2 aircraft results from 54S to 72S Latitude, *J. Geophys. Res., 94*, 16,649–63, 1989.

Burkholder, J. B., J. J. Orlando, and C. J. Howard, Ultraviolet absorption cross sections of Cl_2O_2 between 210 and 410 nm, *J. Phys. Chem., 94*, 687–95, 1990.

Burkholder, J. B., R. L. Mauldin III, R. J. Yokelson, S. Solomon, and A. R. Ravishankara, Kinetic, thermochemical, and spectroscopic study of Cl_2O_3, *J. Phys. Chem., 97*, 7597, 1993.

Cox, R. A. and G. D. Hayman, The stability and photochemistry of dimers of the ClO radical and implications for Antarctic ozone depletion, *Nature, 332*, 796-800, 1988.

Chipperfield, M. P. and R. L. Jones, Relative influence of atmospheric chemistry and transport on Arctic ozone trends, *Nature, 400*, 551–4, 1999.

DeMore, W. B. and E. Tschuikow-Roux, Ultraviolet spectrum and chemical reactivity of the ClO dimer, *J. Phys. Chem., 94*, 5856–60, 1990.

Fahey, D. W. *et al.*, The detection of large HNO_3-containing particles in the winter Arctic stratosphere, *Science, 291*, 1026–31, 2001.

Hanisco, T. F., J. B. Smith, R. M. Stimpfle, D. M. Wilmouth, and J. G. Anderson, *In situ* observations of HO_2 and OH obtained on the NASA ER-2 in the high-ClO conditions of the 1999/2000 Arctic polar vortex, *J. Geophys. Res., 107*, SOL 26, 2002.

Huder, K. J. and W. B. DeMore, Absorption cross sections of the ClO dimer, *J. Phys. Chem., 99*, 3905–8, 1995.

Kirk-Davidoff, D. B., E. J. Hintsa, J. G. Anderson, and D. W. Keith, The effect of climate change on ozone depletion through changes in stratospheric water vapour, *Nature, 402*, 399-401, 1999.

Logan, J. A., *et al.* Trends in the vertical distribution of ozone: A comparison of two analyses of ozonesonde data, *J. Geophys. Res., 104*, 26,375–99, 1999.

Mauldin, R. L., J. B. Burkholder, and A. R. Ravishankara, A photochemical, thermodynamic and kinetic study of ClOO. *J. Phys. Chem., 96*, 2582–8, 1992.

McElroy, C. T., A spectrometer for the measurement of direct and scattered solar irradiance from on-board the NASA ER-2 high-altitude aircraft, *Geophys. Res. Lett., 22*, 1365–8, 1995.

McElroy, M. B., R. J. Salawitch, S. C. Wofsy, and J. A. Logan, Reductions of Antarctic ozone due to synergistic interactions of chlorine and bromine, *Nature, 321*, 759–62, 1986.

McGrath, M. P., K. C. Clemitshaw, F. S. Rowland, and W. J. Hehre, Thermochemical stabilities and vibrational spectra of isomers of the chlorine oxide dimer, *Geophys. Res. Lett., 15*, 883–6, 1988.

McGrath, M. P., K. C. Clemitshaw, F. S. Rowland, and W. J. Hehre, Structures, relative stabilities, and vibrational spectra of isomers of Cl_2O_2: The role of the chlorine oxide dimer in Antarctic ozone depleting mechanisms, *J. Phys. Chem., 94*, 6126–32, 1990.

Molina, L. T. and M. J. Molina, Production of Cl_2O_2 from the self-reaction of the ClO radical, *J. Phys. Chem., 91*, 433–6, 1987.

Molina, M. J., A. J. Colussi, L. T. Molina, R. N. Schindler, and T. L. Tso, Quantum yield of chlorine-atom formation in the photodissociation of chlorine peroxide (ClOOCl) at 308 nm, *Chem. Phys. Lett., 173*, 310–15, 1990.

Moore, T. A., M. Okumura, J. W. Seale, and T. Minton, UV photolysis of ClOOCl, *J. Phys. Chem. A, 103*, 1691–5, 1999.

Newman, P. A., J. F. Gleason, R. D. McPeters, and R. S. Stolarski, Anomalously low ozone over the Arctic, *Geophys. Res. Lett., 24*, 2689–92, 1997.

Newman, P. A., D. W. Fahey, W. H. Brune, and M. J. Kurylo, Preface, *J. Geophys. Res., 104*, 26,481–95, 1999.

Newman, P. A., *et al.*, An overview of the SOLVE/THESEO 2000 campaign, *J. Geophys. Res., 107*, SOL 1, 2002.

Nicholas, J. E. and R. G. W. Norrish, Some reactions in the chlorine and oxygen system studies by flash photolysis, *Proc. Royal Soc. A., 307*, 391–7, 1968.

Nickolaisen, S. L., R. R. Friedl, and S. P. Sander, Kinetics and mechanism of the ClO + ClO reaction: Pressure and temperature dependencies of the bimolecular and termolecular channels and thermal decomposition of chlorine peroxide, *J. Phys. Chem., 98*, 155–69, 1994.

Nicovich, J. M, K. D. Kreutter, C. J. Shackelford, and P. H. Wine, Thermochemistry and kinetics of the $Cl+O_2$ association reaction, *Chem. Phys. Lett., 179*, 367–73, 1991.

Perkins, K. K., *et al.*, The NO_x-HNO_3 system in the lower stratosphere: Insights from *in situ* measurements and implications of the J_{HNO3}-[OH] relationship, *J. Phys. Chem. A, 105*, 1521–34, 2001.

Perkins, K. K., *In situ* observations of nitrogen dioxide using laser-induced fluorescence detection: Examining the NO_2-HNO_3 system in the lower stratosphere, PhD Thesis, Harvard University, 2000.

Permien, T., R. Vogt, and R. N. Schindler, Mechanisms of gas phase-liquid phase chemical transformations, In Air Pollution Report #17; Cox, R. A. Ed.: Environmental Research Program of the CEC.: Brussels, 1988.

Randall, C. E., *et al.*, Reconstruction of three-dimensional ozone fields using POAM III during SOLVE, *J. Geophys. Res., 107, (D20)*, 8299, doi:10.1029/2001JD000471, 2002.

Rex, M., R. J. Salawitch, M. L. Santee, J. W. Waters, K. Hoppel, and R. Bevilacqua, On the unexplained stratospheric ozone losses during cold Arctic Januaries, *Geophys. Res. Lett., 30*, 8-1, 2003.

Richard, E. C., K. C. Aikin, A. E. Andrews, B. C. Daube, C. Gerbig, S. C. Wofsy, P. A. Romashkin, D. F. Hurst, E. A. Ray, and F. L. Moore, Severe chemical ozone loss inside the Arctic polar vortex during winter 1999-2000 inferred from *in situ* airborne observations, *Geophys. Res. Lett., 28*, 2197–200, 2001.

Salawitch, R. J., *et al.*, Chemical loss of ozone in the Arctic polar vortex in the winter of 1991-1992, *Science*, 261, 1146–9, 1993.

Salawitch, R. J., *et al.*, The distribution of hydrogen, nitrogen, and chlorine radicals in the lower stratosphere: Implications for changes in O_3 due to emission of NO_y from supersonic aircraft, *Geophys. Res. Lett., 21*, 2547–50, 1994.

Salawitch, R. J., Ozone depletion: A greenhouse warming connection, *Nature, 392*, 551–2, 1998.

Sander, S. P., R. R. Friedl, and Y. L. Yung, Rate of formation of the ClO dimer in the polar stratosphere: Implications for ozone loss, *Science, 245*, 1989–98, 1989.

Sander, S. P., *et al.*, Chemical kinetics and photochemical data for use in stratospheric modeling, evaluation number 13, *JPL Publ. 00*-3, 2000.

Sander, S. P., *et al.*, Chemical kinetics and photochemical data for use in stratospheric modeling, evaluation number 14, *JPL Publ. 02*-25, 2002.

Scott, S. G., *et al.*, The meteorological measurement system on the NASA ER-2 aircraft, *J. Atmos. Oceanic Technol., 7*, 525–40, 1990.

Shindell, D. T. and R. L. deZafra, The chlorine budget of the lower polar stratosphere: Upper limits on ClO and implications of new Cl_2O_2 photolysis cross sections, *Geophys. Res. Lett., 22*, 3215–8, 1995.

Shindell, D. T. and R. L. deZafra, Chlorine monoxide in the Antarctic spring vortex 2. A comparison of measured and modeled diurnal cycling over McMurdo Station, 1993, *J. Geophys. Res., 101*, 1475–87, 1996.

Shindell, D. T., D. Rind, and P. Longergan, Increased polar stratospheric ozone losses and delayed eventual recovery owing to increasing greenhouse-gas concentrations, *Nature, 392*, 589–92, 1998.

Solomon, S. Stratospheric ozone depletion: A review of concepts and history, *Rev. Geophys., 37*, 275-316, 1999.

Stimpfle, R. M., *et al.*, The coupling of $ClONO_2$, ClO and NO_2 in the lower stratosphere from *in situ* observations using the NASA ER-2 aircraft, *J. Geophys. Res., 104*, 26,705–14, 1999.

Stachnik, R. A., R. Salawitch, A. Engel, and U. Schmidt, Measurements of chlorine partitioning in the winter Arctic stratosphere, *Geophys. Res. Lett., 26*, 3093–6, 1999.

Trolier, M., R. L. Mauldin, and A. R. Ravishankara, Rate coefficient for the termolecular channel of the self-reaction of ClO, *J. Phys. Chem., 94*, 4896–907, 1990.

Tuck, A. F., R. T. Watson, E. P. Condon, J. J. Margitan, and O. B. Toon, The planning and execution of ER-2 and DC-8 aircraft flights over Antarctica, August and September 1987, *J. Geophys. Res., 94*, 11,181–222, 1987.

Vömel, H., D. W. Toohey, T. Deshler, and C. Kroger. Sunset observations of ClO in the Arctic polar vortex and implications for ozone loss, *Geophys. Res. Lett., 28*, 4183–6, 2001.

Wennberg, P. W., R. J. Salawitch, D. J. Donaldson, T. F. Hanisco, E. J. Lanzendorf, K. K. Perkins, S. A. Lloyd, V. Vaida, R. S. Gao, E. J. Hintsa, R. C. Cohen, W. H. Swartz, T. L. Kusterer, and D. E. Anderson, Twilight observations suggest unknown sources of HO_x, *Geophys. Res. Lett., 26*, 1373–6, 1999.

Wilmouth, D. M., Laboratory studies and *in situ* stratospheric observations of inorganic chlorine and bromine species critical to catalytic ozone destruction, PhD Thesis, Harvard University, 2002.

Wongdontri-Stupor, W., R. Simonaitis, and J. Heicklen. The reaction of ClOO with NO, *Geophys. Res. Lett., 5*, 1005–8, 1978.

World Meteorological Organization (WMO); Scientific assessment of ozone depletion: 2002, *WMO Rep. 47*, Global Ozone Research And Monitoring Project, Geneva, Switzerland, 2003.

Publications resulting from this funding:

Moyer, E. J., D. B. Kirk-Davidoff, E. Weinstock, J. B. Smith, J. V. Pittman, and J. G. Anderson, "*In-situ* observations of the control of water vapor in the tropical upper troposphere and stratosphere," in preparation, 2005.

Sayres, D. S., J. V. Pittman, J. B. Smith, E. M. Weinstock, J. G. Anderson, G. Heymsfield, L. Li, A. Fridlind, and A. S. Ackerman, Methods for validation and intercomparison of remote sensing and *in situ* ice water measurements: Case studies from CRYSTAL-FACE and Model Results, *J. Geophys. Res.*, in preparation, 2005.

Smith, J. B., E. Weinstock, J. V. Pittman, D. Sayres, and J. G. Anderson, "Observations and implications of supersaturation in the presence of cirrus in the tropical and subtropical upper troposphere," in preparation, 2005.

Spackman, J. R., E. M. Weinstock, J. G. Anderson, C. R. Webster, and D. F. Hurst, "Deducing transport into the lowermost stratosphere from *in situ* measurements of water vapor, CH_4, and N_2O: Implications for mid-latitude ozone," in preparation, 2005.

Stimpfle, R. M., D. M. Wilmouth, R. J. Salawitch, and J. G. Anderson, The first measurements of ClOOCl in the stratosphere: The coupling of ClOOCl and ClO in the arctic polar vortex, *J. Geophys. Res.* **109**, D03301, doi:10.1029/2003JD003811, February 4, 2004.

Weinstock, E. M., E. J. Hintsa, D. B. Kirk-Davidoff, J G. Anderson, A. E. Andrews, R. L. Herman, C. R. Webster, M. Loewenstein, J. R. Podolske and T. P. Bui, "Constraints on the seasonal cycle of stratospheric water vapor using *in situ* measurements from the ER-2 and a CO photochemical clock," *J. Geophys. Res.* **106**(D19), 22,707–24, 2001.

Weinstock, E. M., J. B. Smith, D. Sayres, J. R. Spackman, J. V. Pittman, N. Allen, J. Demusz, M. Greenberg, M. Rivero, L. Solomon and J. G. Anderson, "Measurements of the total water content of cirrus clouds: Instrument details and calibration, " *J. Atmos. and Oceanic Techn.*, submitted 2005.

Weinstock, E. M., J. B. Smith, D. Sayres, J. V. Pittman, N. Allen and J. G. Anderson, "Measurements of the total water content of cirrus clouds: Instrument performance and validation," *J. Atmos. and Oceanic Techn.*, submitted 2005.

There are no inventions resulting from this funding.